

NAVAL POSTGRADUATE SCHOOL

Monterey, California



THESIS

**STUDIES OF SOUTH CHINA SEA CIRCULATION
AND THERMAL STRUCTURE USING A THREE
DIMENSIONAL NUMERICAL MODEL**

by

Nathan L. Edmons

September, 1996

Thesis Advisor:

Peter C. Chu

Thesis
E23956

Approved for public release; distribution is unlimited.

Replacement Copy.

~~DUPLICATE LIBRARY 7.6.~~

~~REPLACEMENT COPY~~

~~REPLACEMENT COPY~~

DUTLEY-HOY LIBRARY
NEW BRUNSWICK HIGH SCHOOL
MONTICELLY CA 95065-1411

REPORT DOCUMENTATION PAGE

Form Approved OMB No. 0704-0188

Public reporting burden for this collection of information is estimated to average 1 hour per response, including the time for reviewing instruction, searching existing data sources, gathering and maintaining the data needed, and completing and reviewing the collection of information. Send comments regarding this burden estimate or any other aspect of this collection of information, including suggestions for reducing this burden, to Washington Headquarters Services, Directorate for Information Operations and Reports, 1215 Jefferson Davis Highway, Suite 1204, Arlington, VA 22202-4302, and to the Office of Management and Budget, Paperwork Reduction Project (0704-0188) Washington DC 20503.

1. AGENCY USE ONLY (Leave blank)		2. REPORT DATE September 1996.		3. REPORT TYPE AND DATES COVERED Master's Thesis	
4. TITLE AND SUBTITLE TITLE OF THESIS. STUDIES OF SOUTH CHINA SEA CIRCULATION AND THERMAL STRUCTURE USING A THREE DIMENSIONAL NUMERICAL MODEL				5. FUNDING NUMBERS	
6. AUTHOR(S) Nathan L. Edmons					
7. PERFORMING ORGANIZATION NAME(S) AND ADDRESS(ES) Naval Postgraduate School Monterey CA 93943-5000				8. PERFORMING ORGANIZATION REPORT NUMBER	
9. SPONSORING/MONITORING AGENCY NAME(S) AND ADDRESS(ES)				10. SPONSORING/MONITORING AGENCY REPORT NUMBER	
11. SUPPLEMENTARY NOTES The views expressed in this thesis are those of the author and do not reflect the official policy or position of the Department of Defense or the U.S. Government.					
12a. DISTRIBUTION/AVAILABILITY STATEMENT Approved for public release; distribution is unlimited.				12b. DISTRIBUTION CODE	
<p>13. ABSTRACT (maximum 200 words)</p> <p>The seasonal ocean circulation and thermal structure in the South China Sea (SCS) were studied numerically using the Princeton Ocean Model (POM) with 20 km horizontal resolution and 23 sigma levels conforming to a realistic bottom topography. A sixteen month control run was performed using climatological monthly mean wind stresses and restoring type salt and heat fluxes as surface forcing terms and observational oceanic inflow/outflow at the open boundaries. The seasonally averaged effects of isolated forcing terms are presented and analyzed from the following experiments: 1) non-linear effects removed, 2) wind effects removed, 3) open boundary inflow/outflow set to zero, and 4) open boundary inflow/outflow doubled. This procedure allowed analysis of spatial and temporal contributions of the isolated parameter to the general hydrology of the SCS and some of its specific features. A coastal jet is identified and analyzed, as are a mesoscale topographic gyre and several counter currents. Non-linearity is shown to be important to the energy and volume transport of baroclinic eddy features, but otherwise insignificant. Boundary transport from open lateral boundaries is determined to be of considerable importance to summer circulation and thermal structure, with little effect found for the winter monsoon hydrology. In general, monsoonal circulation patterns and upwelling phenomena are determined and forced by the wind, while boundary transport effects play a secondary role in determining the magnitude of the circulation velocities.</p>					
14. SUBJECT TERMS South China Sea, numerical simulation, sensitivity studies, circulation, thermal structure.				15. NUMBER OF PAGES 103	
				16. PRICE CODE	
17. SECURITY CLASSIFICATION OF REPORT Unclassified	18. SECURITY CLASSIFICATION OF THIS PAGE Unclassified	19. SECURITY CLASSIFICATION OF ABSTRACT Unclassified	20. LIMITATION OF ABSTRACT UL		

NSN 7540-01-280-5500

Standard Form 298 (Rev. 2-89)
Prescribed by ANSI Std. Z39-18 298-102

Approved for public release; distribution is unlimited.

**STUDIES OF SOUTH CHINA SEA CIRCULATION AND THERMAL
STRUCTURE USING A THREE DIMENSIONAL NUMERICAL MODEL**

Nathan L. Edmons

Lieutenant, United States Navy

B.S., University of Washington, Seattle, Washington, 1989


**Submitted in partial fulfillment
of the requirements for the degree of**

MASTER OF SCIENCE IN PHYSICAL OCEANOGRAPHY

from the

NAVAL POSTGRADUATE SCHOOL

September 1996



ABSTRACT

42
DUDNEY HIGGINS LIBRARY SCHOOL
NAVIGATIONAL SCHOOL
MONTEREY CA 93943-5101

The seasonal ocean circulation and thermal structure in the South China Sea (SCS) were studied numerically using the Princeton Ocean Model (POM) with 20 km horizontal resolution and 23 sigma levels conforming to a realistic bottom topography. A sixteen month control run was performed using climatological monthly mean wind stresses and restoring type salt and heat fluxes as surface forcing terms and observational oceanic inflow/outflow at the open boundaries. The seasonally averaged effects of isolated forcing terms are presented and analyzed from the following experiments: 1) non-linear effects removed, 2) wind effects removed, 3) open boundary inflow/outflow set to zero, and 4) open boundary inflow/outflow doubled. This procedure allowed analysis of the contribution of the isolated parameter to the general hydrology of the SCS and some of its specific features. A coastal jet is identified and analyzed, as are a mesoscale topographic gyre and several counter currents. Non-linearity is shown to be important to the energy and volume transport of baroclinic eddy features, but otherwise insignificant. Boundary transport from lateral boundaries is determined to be of considerable importance to summer circulation and thermal structure, with little effect found for the winter monsoon hydrology. In general, monsoonal circulation patterns and upwelling phenomena are determined and forced by the

wind, while boundary transport effects play a secondary role in determining the magnitude of the circulation velocities.

TABLE OF CONTENTS

I. INTRODUCTION	1
A. DESCRIPTION OF THE SOUTH CHINA SEA.....	1
B. PREVIOUS NUMERICAL SIMULATION STUDIES	7
C. OBJECTIVES.....	8
II. PRINCETON OCEAN MODEL	11
A. MODEL FEATURES.....	11
1. Sigma Coordinates	12
2. Finite Differencing.....	14
3. Mode Splitting	14
4. Level Two Turbulence Closure.....	15
B. MODEL GOVERNING EQUATIONS.....	15
1. The Continuity Equation.....	15
2. The Momentum Equations.....	16
3. The Temperature and Salinity Conservation Equations	16
4. Subgrid Scale Horizontal Mixing Processes.....	16
C. INITIAL CONDITIONS AND BOUNDARY CONDITIONS.....	17
1. Initial Conditions and Initialization	17
2. Bottom Boundaries	19
D. FORCING.....	19
1. Atmospheric Forcing	19
2. Lateral Boundaries	20
III. EXPERIMENTS	23
IV. RESULTS	25
A. CONTROL RUN	25
1. Summer Monsoon.....	25
2. Winter Monsoon	36
B. SENSITIVITY STUDIES	42
1. Effects of non-linearity (Run 2).....	42
2. Effects of wind (Run 3).....	54
3. Effects of lateral boundary transport (Runs 4 and 5).....	65
V. CONCLUSIONS.....	81
LIST OF REFERENCES.....	85
INITIAL DISTRIBUTION LIST.....	87

1	THE HISTORY OF THE
2	REIGN OF
3	CHARLES THE FIRST
4	BY
5	JOHN BURNET
6	OF THE UNIVERSITY OF OXFORD
7	IN TWO VOLUMES
8	THE SECOND VOLUME
9	CONTAINING
10	THE HISTORY OF THE
11	REIGN OF
12	CHARLES THE FIRST
13	BY
14	JOHN BURNET
15	OF THE UNIVERSITY OF OXFORD
16	IN TWO VOLUMES
17	THE SECOND VOLUME
18	CONTAINING
19	THE HISTORY OF THE
20	REIGN OF
21	CHARLES THE FIRST
22	BY
23	JOHN BURNET
24	OF THE UNIVERSITY OF OXFORD
25	IN TWO VOLUMES
26	THE SECOND VOLUME
27	CONTAINING
28	THE HISTORY OF THE
29	REIGN OF
30	CHARLES THE FIRST
31	BY
32	JOHN BURNET
33	OF THE UNIVERSITY OF OXFORD
34	IN TWO VOLUMES
35	THE SECOND VOLUME
36	CONTAINING
37	THE HISTORY OF THE
38	REIGN OF
39	CHARLES THE FIRST
40	BY
41	JOHN BURNET
42	OF THE UNIVERSITY OF OXFORD
43	IN TWO VOLUMES
44	THE SECOND VOLUME
45	CONTAINING
46	THE HISTORY OF THE
47	REIGN OF
48	CHARLES THE FIRST
49	BY
50	JOHN BURNET
51	OF THE UNIVERSITY OF OXFORD
52	IN TWO VOLUMES
53	THE SECOND VOLUME
54	CONTAINING
55	THE HISTORY OF THE
56	REIGN OF
57	CHARLES THE FIRST
58	BY
59	JOHN BURNET
60	OF THE UNIVERSITY OF OXFORD
61	IN TWO VOLUMES
62	THE SECOND VOLUME
63	CONTAINING
64	THE HISTORY OF THE
65	REIGN OF
66	CHARLES THE FIRST
67	BY
68	JOHN BURNET
69	OF THE UNIVERSITY OF OXFORD
70	IN TWO VOLUMES
71	THE SECOND VOLUME
72	CONTAINING
73	THE HISTORY OF THE
74	REIGN OF
75	CHARLES THE FIRST
76	BY
77	JOHN BURNET
78	OF THE UNIVERSITY OF OXFORD
79	IN TWO VOLUMES
80	THE SECOND VOLUME
81	CONTAINING
82	THE HISTORY OF THE
83	REIGN OF
84	CHARLES THE FIRST
85	BY
86	JOHN BURNET
87	OF THE UNIVERSITY OF OXFORD
88	IN TWO VOLUMES
89	THE SECOND VOLUME
90	CONTAINING
91	THE HISTORY OF THE
92	REIGN OF
93	CHARLES THE FIRST
94	BY
95	JOHN BURNET
96	OF THE UNIVERSITY OF OXFORD
97	IN TWO VOLUMES
98	THE SECOND VOLUME
99	CONTAINING
100	THE HISTORY OF THE

LIST OF FIGURES

Figure 1 The South China Sea and surrounding areas.....	2
Figure 2 Bathymetry contours (m) of the South China Sea.....	3
Figure 3 Climatological wind stress (dyne/cm^2) for (a) June (b) December (after Hellerman and Rosenstein, 1983).....	5
Figure 4 Observational surface circulation (a) April, (b) June, (c) December (after Wyrtki, 1961).....	6
Figure 5 The model horizontal grid.....	13
Figure 6 Temporal variation of the total kinetic energy.....	18
Figure 7 Near surface circulation for control run during summer (a) May 15, (b) July 15, (c) September 15.....	26
Figure 8 Sea surface elevation (m) of the control run averaged over (a) summer monsoon, (b) winter monsoon.....	27
Figure 9 Temperature ($^{\circ}\text{C}$) distribution for control run at 114°E longitudinal cross section averaged over (a) summer monsoon, (b) winter monsoon.....	29
Figure 10 Sea surface temperatures ($^{\circ}\text{C}$) of the control run averaged over (a) summer monsoon, (b) winter monsoon.....	30
Figure 11 Satellite imagery of South China Sea sea surface temperatures for (a) summer, (b) winter.....	31
Figure 12 V component of velocity (m/s) of control run at 6°N latitudinal cross section averaged over (a) summer monsoon, (b) winter monsoon.....	32
Figure 13 V component of velocity (m/s) of control run at 13°N latitudinal cross section averaged over (a) summer monsoon, (b) winter monsoon.....	33
Figure 14 Temperature ($^{\circ}\text{C}$) profile of control run at 13°N latitudinal cross section averaged over (a) summer monsoon, (b) winter monsoon.....	34
Figure 15 U component of velocity (m/s) of control run at 114°E longitudinal cross section for (a) July 15, (b) September 15.....	35

Figure 16 Volume transport (S_v) of control run averaged over (a) winter monsoon, (b) summer monsoon.....	37
Figure 17 Near surface circulation for control run during winter (a) October 15, (b) December 15, (c) March 15.....	38
Figure 18 U component of velocity (m/s) of control run at 110° E longitudinal cross section averaged over winter monsoon.....	40
Figure 19 (a) V component of velocity (m/s) for control run and (b) temperature (°C) profile of control run for 15 March at 15° N latitudinal cross section.....	41
Figure 20 Near surface circulation for linear run during summer (a) May 15, (b) July 15, (c) September 15.....	43
Figure 21 Near surface circulation for linear run during winter (a) October 15, (b) December 15, (c) March 15.....	44
Figure 22 A comparison of kinetic energy ($\text{kg m}^2/\text{s}^2$) during the winter monsoon for (a) control run, no wind run, and linear run and (b) control run, closed boundaries run, and double lateral transport run.....	45
Figure 23 Sea surface temperature (°C) differences between control run and linear run over (a) summer monsoon, (b) winter monsoon.....	46
Figure 24 Volume transport difference (S_v) between control run and linear run averaged over summer monsoon.....	47
Figure 25 V component of velocity difference (m/s) between control run and linear run at 6° N latitudinal cross section averaged over summer monsoon.....	49
Figure 26 V component of velocity difference (m/s) between control run and linear run at 13° N latitudinal cross section averaged over summer monsoon.....	50
Figure 27 V component of velocity difference (m/s) between control run and linear run at 13° N latitudinal cross section averaged over winter monsoon.....	51
Figure 28 Volume transport difference (S_v) between control run and linear run averaged over winter monsoon.....	52
Figure 29 V component of velocity difference (m/s) between control run and linear run at 6° N latitudinal cross section averaged over winter monsoon.....	53

Figure 30 Near surface circulation for no wind run during summer (a) May 15, (b) July 15, (c) September 15.....	55
Figure 31 Near surface circulation for no wind run during winter (a) October 15, (b) December 15, (c) March 15.....	56
Figure 32 Sea surface height difference (m) between control run and no wind run averaged over (a) summer monsoon, (b) winter monsoon.....	57
Figure 33 Sea surface temperatures difference (°C) between control run and no wind run averaged over (a) summer monsoon, (b) winter monsoon.....	58
Figure 34 Sea surface salinity difference (ppt) between control run and no wind run averaged over (a) summer monsoon, (b) winter monsoon.....	59
Figure 35 V component of velocity (m/s) for no wind run 15 July at 5° N latitudinal cross section.....	60
Figure 36 V component of velocity difference (m/s) between control run and no wind run averaged over summer monsoon at (a) 6° N latitudinal cross section, (b) 13° N latitudinal cross section.....	62
Figure 37 Volume transport difference (Sv) between control run and no wind run averaged over (a) summer monsoon, (b) winter monsoon.....	63
Figure 38 V component of velocity difference (m/s) between control run and no wind run averaged over winter monsoon at (a) 6° N latitudinal cross section, (b) 13° N latitudinal cross section.....	64
Figure 39 Near surface circulation for closed boundaries run during summer (a) May 15, (b) July 15, (c) September 15.....	66
Figure 40 Near surface circulation for closed boundaries run during winter (a) October 15, (b) December 15, (c) March 15.....	67
Figure 41 Near surface circulation for double lateral transport run during summer (a) May 15, (b) July 15, (c) September 15.....	68
Figure 42 Near surface circulation for double lateral transport run during winter (a) October 15, (b) December 15, (c) March 15.....	69

Figure 43 Sea surface height difference (m) between control run and closed boundaries run averaged over (a) summer monsoon, (b) winter monsoon.....	70
Figure 44 Sea surface temperatures difference ($^{\circ}\text{C}$) between control run and closed boundaries run averaged over summer monsoon.....	71
Figure 45 V component of velocity difference (m/s) between control run and closed boundaries run averaged over summer monsoon at 6° N latitudinal cross section.....	73
Figure 46 V component of velocity difference (m/s) between control run and closed boundaries run averaged over summer monsoon at 13° N latitudinal cross section.....	74
Figure 47 V component of velocity difference (m/s) between control run and closed boundaries run averaged over winter monsoon at (a) 6° N latitudinal cross section, (b) 13° N latitudinal cross section.....	75
Figure 48 V component of velocity difference (m/s) between control run and double lateral transport run averaged over summer monsoon at (a) 6° N latitudinal cross section, (b) 13° N latitudinal cross section.....	77
Figure 49 Volume transport difference (Sv) between control run and double lateral transport run averaged over summer monsoon.....	78
Figure 50 V component of velocity difference (m/s) between control run and double lateral transport run averaged over winter monsoon at (a) 6° N latitudinal cross section, (b) 13° N latitudinal cross section.....	79

ACKNOWLEDGEMENTS

The author would like to acknowledge the unfailing support of Laura Ehret, Chenwu Fan and others in the Naval Ocean Analysis and Prediction Laboratory. Without their tireless efforts and assistance with computer programming this thesis would not have been produced. Additionally much of the credit for this work is due to Professor Peter Chu, the benefit of his grasp of the concepts involved is exceeded only by his patience in explaining them to the author. His positive attitude and moral support were essential elements to making this a rich and rewarding experience.

I. INTRODUCTION

The South China Sea (SCS), and the nations on its border, constitutes a region of strategic political and military importance to the United States and its allies. As a semi-enclosed ocean, it is subject to high spatial and temporal variability from external forcing factors. The Naval Oceanographic Office (NAVOCEANO) has been tasked to develop an ocean forecasting capability for this region. This thesis uses the three dimensional model currently being assessed for the SCS to evaluate the relative importance of various forcing terms to circulation and thermal structure.

A. DESCRIPTION OF THE SOUTH CHINA SEA

The SCS extends across the tropical and sub-tropical zones and is located between the Asian landmass to the west, the Phillipine Islands and Borneo to the east and China and Taiwan to the north (Figure 1), a total of $3.5 \times 10^6 \text{ km}^2$ surface area. It includes the Gulf of Thailand and is connected to the East China Sea (through the Formosa Strait), the Pacific Ocean (through the Luzon Strait), the Sulu Sea (through the Balabac Strait), the Java Sea (through the Gasper and Karimata Straits) and to the Indian Ocean (through the Strait of Malacca). All of these straits are shallow except the Luzon Strait whose maximum depth is 1800 m, and consequently the SCS is considered a semi-enclosed water body (Huang et al., 1994). The complex topography includes the broad shallows of the Sunda Shelf in the south; the continental shelf of the Asian landmass in the west, extending from the Gulf of Tonkin to the Formosa Strait; a deep, elliptical shaped basin in the center, and numerous reef islands and underwater plateaus scattered throughout (Figure 2). The shelf that extends from the Gulf of Tonkin to the Formosa Strait is consistently about 70 m deep, and averages 150 km in width from the shoreline; the central deep basin is 1900 km along its major axis (northeast-southwest) and approximately 1100 km along its minor axis, and extends to over 4000 m deep. The Sunda Shelf is the submerged connection between southeast Asia, Malaysia, Sumatra,

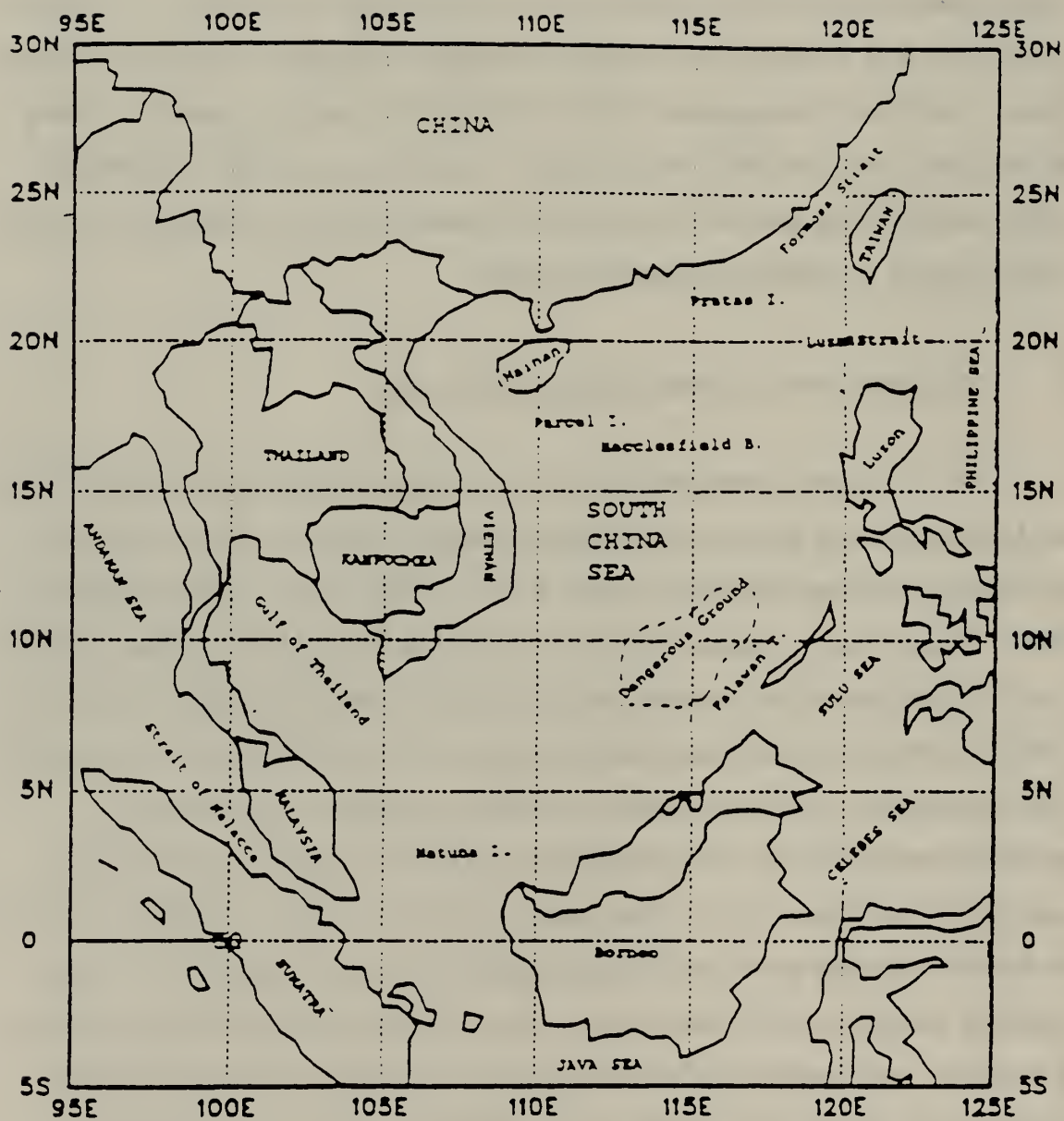


Figure 1. The South China Sea and surrounding areas.

South China Seas Bathymetry Contours (m)

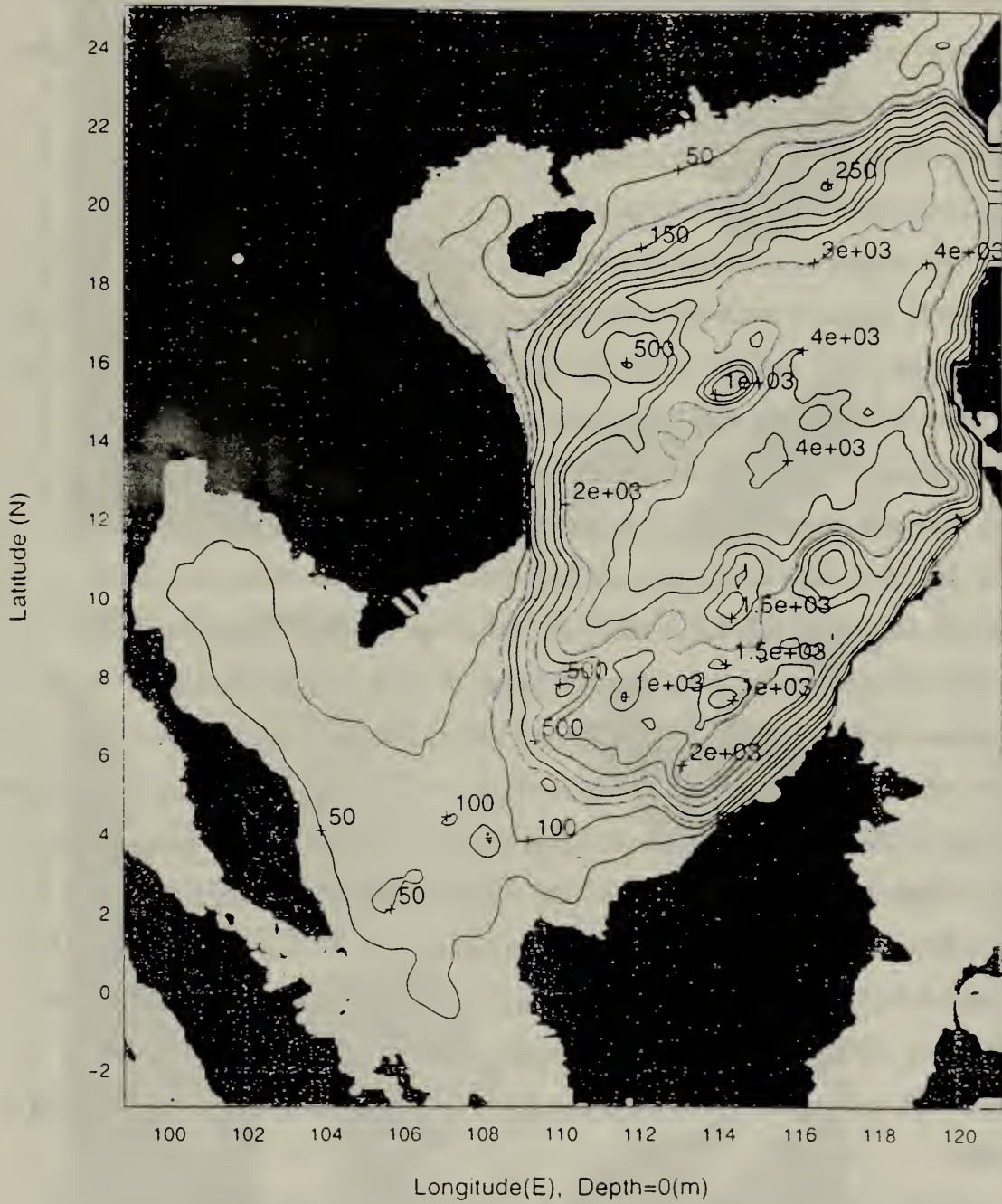


Figure 2. Bathymetry contours (m) of the South China Sea.

Java and Borneo and is 100 m deep in the middle; the Gulf of Thailand is about 70 m deep in its central part.

The SCS is subjected to a seasonal monsoon system (Wyrтки, 1961). From April to August, the weaker southwesterly summer monsoon winds lead to a wind stress of over 1 dyne/cm^2 (Figure 3a) which drives an anticyclonic circulation in the SCS (Figure 4b). From November to March, the stronger northeasterly winter monsoon winds corresponding to a maximum wind stress of nearly 3 dyne/cm^2 (Figure 3b) cause a cyclonic circulation in the SCS (Figure 4c).

The observed circulation patterns of the intermediate to upper layers of the SCS are primarily forced by the local monsoon systems (Wyrтки, 1961). Transitional periods are marked by highly variable winds and surface currents. In early spring, two cyclonic gyres form on the western side of the basin, one between Vietnam and Hainan and another between Vietnam and Malaysia (Figure 4a). During the summer monsoon period, a western intensification of current flow develops along the coast of Vietnam (Figure 4b). A counter current also develops at 11° N that flows from the western intensified current due east across the basin. When the winter monsoon begins, the circulation becomes cyclonic and the cross basin current is re-established at 10° N ; in both summer and winter this current leads to a recirculation of water mass due to the shallow sill depths between the SCS and the Sulu Sea. Another contributing factor to the hydrology of the region is the presence of the Kuroshio Current near the Bashi Channel, in the southern half of the Luzon Strait. The current enters the southern side of the channel then executes a tight, anticyclonic turn and exits the SCS south of Taiwan. An estimated 8-10 Sv ($1 \text{ Sv} = 10^6 \text{ m}^3/\text{s}$) of the intrusion passes through the Bashi Channel (Huang, et al., 1994). This flow exerts a strong influence on the properties of the northern SCS waters and is believed to contribute to currents in the Formosa Strait (Hu et al., 1992).

Eddy behavior in the SCS has two distinct features. First, the number of cold eddies is far greater than the number of warm eddies and second, the eddies are significantly affected by the bottom topography and are most likely to occur near areas

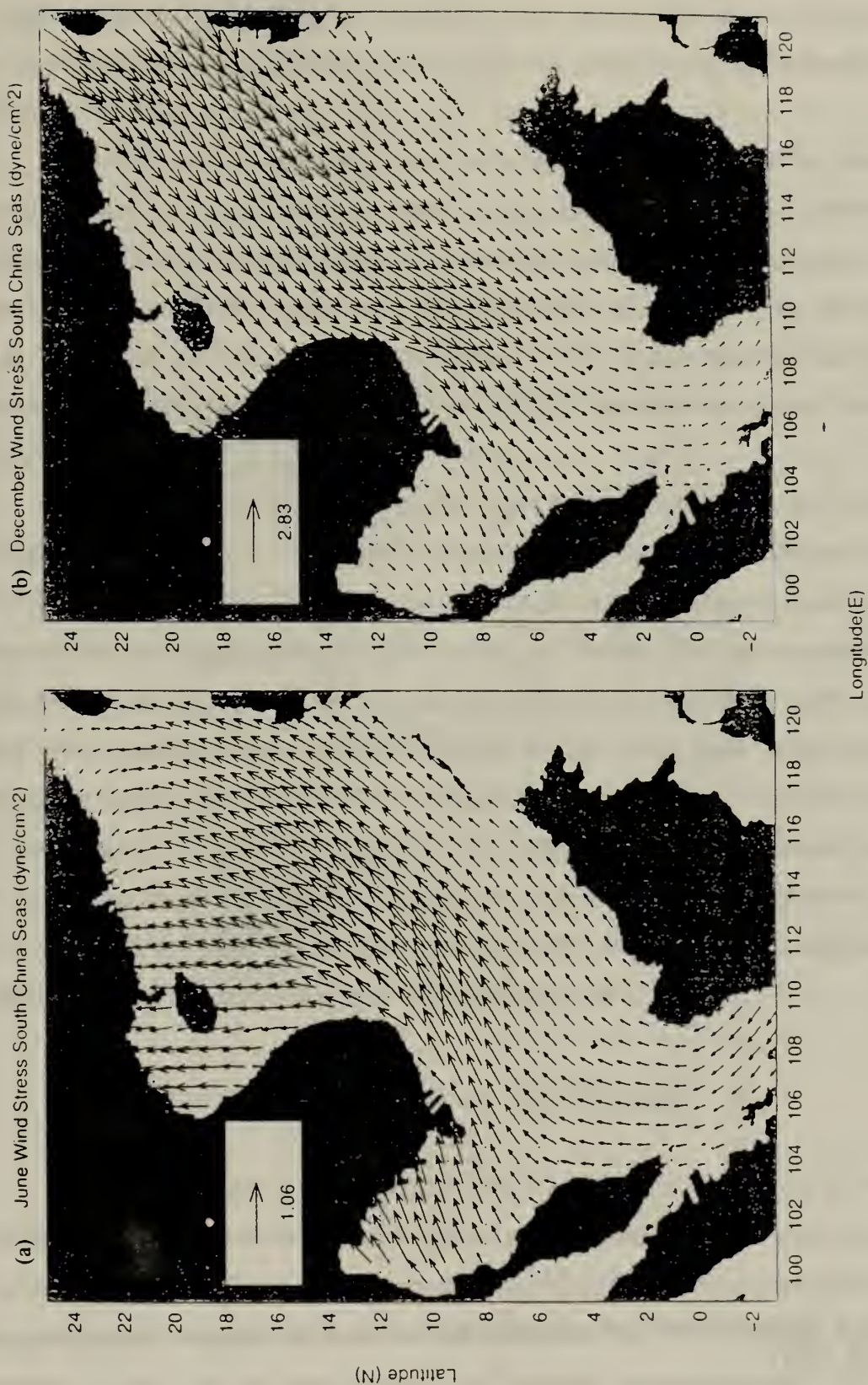


Figure 3. Climatological wind stress (dyne/cm²) for (a) June (b) December (after Hellerman and Rosenstein, 1983).

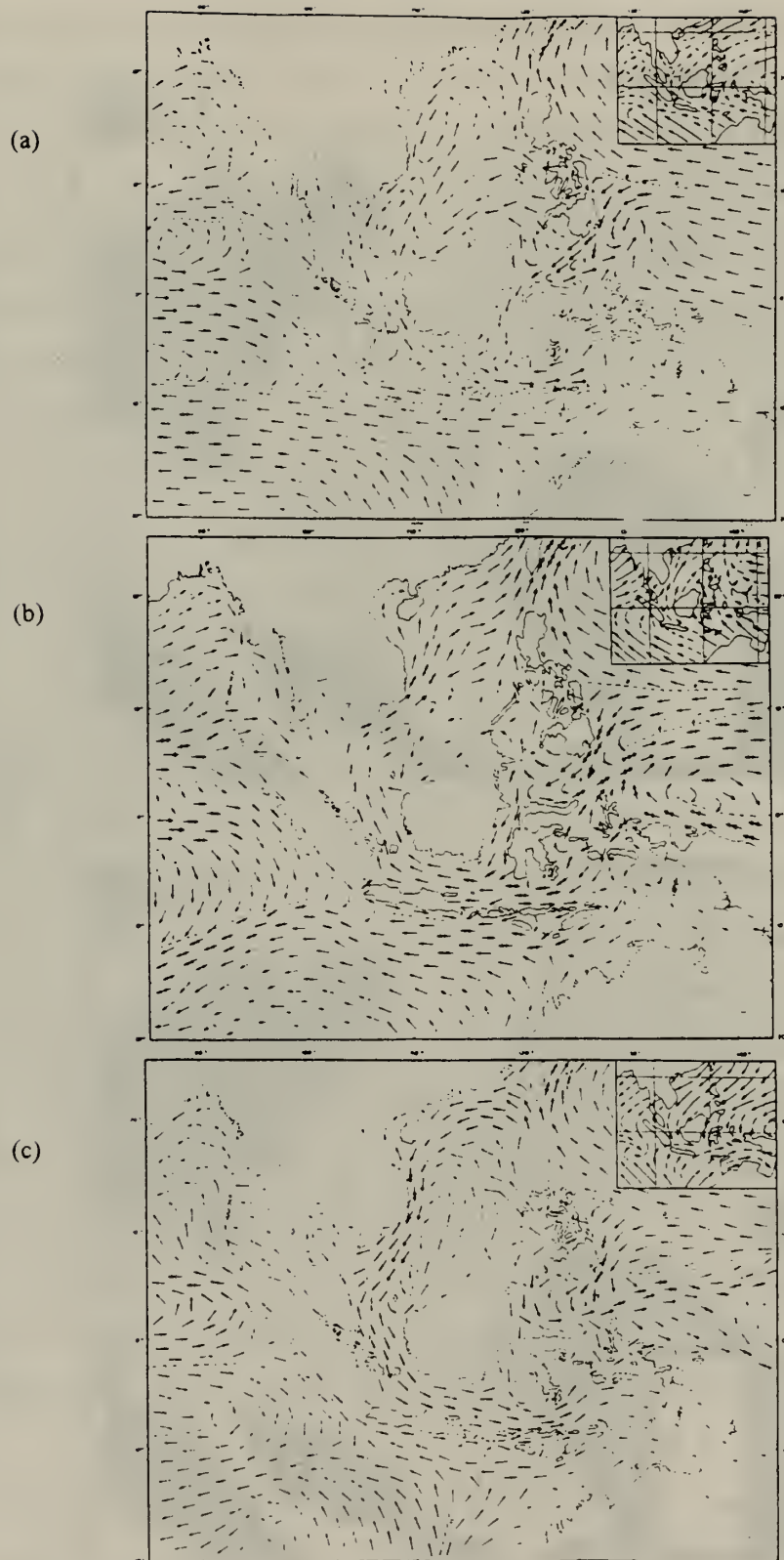


Figure 4. Observational surface circulation (a) April, (b) June, (c) December (after Wyrtki, 1961).

where the localized current velocity is high (Huang, 1994). Small scale eddies with seasonal dependence have been found off coastal Vietnam in summer, near Natuna Island and in reef areas. Large scale eddies have been found primarily during the summer monsoon. (Huang et al., 1994)

Upwelling and downwelling occur extensively along both sides of the basin, specifically off the coast of central Vietnam and the coastal area of eastern Hainan. The summer monsoon is believed to cause an Ekman-type drift current and corresponding seaward transport of water mass, leading to upwelling (Huang et al., 1994). Others (Chen et al., 1982) have pointed out that upwelling has occurred in these areas during winter monsoon conditions, casting doubt on previous ideas concerning the origin of these features.

The SCS is described by two separate water masses. In the north, the waters are cold and saline. The annual variability of salinity is small, due to the inflow and diffusion of high salinity water from the Pacific Ocean through the Bashi Channel. In the south the tropical conditions cause the waters to be warmer and fresher. The high temperature, low salinity water in the south and low temperature, high salinity water in the north causes a steep vertical gradient, usually strongest between 100 and 300 m deep. In the central region, the water is alternately subjected to high and low salinity inflows as the monsoons change; therefore the annual variability is much higher and horizontal gradients are created during the early portion of each monsoon season. Mixed layer depths vary from 30 to 40 m during the summer monsoon, and 70 to 90 m during the winter monsoon with variation being due to both wind and current. (Wyrski, 1961)

B. PREVIOUS NUMERICAL SIMULATION STUDIES

Three dimensional ocean models have been used several times in the past to simulate the circulation in the SCS. Integrating a semi-implicit 12 layer shallow water model from the mean winter and summer conditions for 15 days, Pohlmann (1987) simulated the reversal of the upper layer circulation between the summer and winter monsoon seasons. The horizontal resolution of his model was approximately 50 km. His

results showed westward to southwestward currents during the winter monsoon season and northeastward currents during the summer monsoon season. Due to the low resolution and short integration period, the model didn't adequately represent the thermodynamics and turbulence, and it failed to reproduce the mesoscale eddies and upwelling phenomena known to exist in the SCS.

More recent attempts include work by Wang et al. (1994) who employed four separate models to simulate circulation in the SCS: a multi-layer model, a σ level (contour following) model, a diagnostic model (with reference plane set at 1200 m depth), and a model utilizing the β -spiral method. Although horizontal grid spacing was coarse (generally around 1°), their results agreed well with field observations. The model data clearly showed the intrusion of the Kuroshio through the Bashi Channel as well as some of the larger eddies in the surface layers. No analysis of thermohaline structure was presented, and no sensitivity studies were made of the physical mechanisms producing these features.

Initial uses of the Princeton Ocean Model (POM) for the SCS include Li (1994) and Chu et al. (1994, 1996) who successfully simulated the seasonal variation of the SCS circulation and the thermohaline structure under climatological forcing. Using observational data (Wyrtki, 1961) as a standard, the seasonal circulation and temperature patterns were shown to be better represented by the POM than Pohlmann's shallow water model (Li, 1994). Specifically, the POM data accurately captured the monsoonal variation in surface currents and upwelling events. It is not clear what mechanisms caused the mesoscale variability, and no sensitivity studies were performed by Li (1994) or Chu et al. (1994, 1996).

C. OBJECTIVES

The objective of this study is to quantify the effect of external forcing on SCS circulation and thermohaline features. Utilizing the Princeton Ocean Model (POM), we will examine the circulation and thermal structure of the SCS during summer and winter by analyzing specific features of modeled circulation and thermal structure. The control

run is meant to simulate ‘reality’ against which each experiment is compared. In the experiments, various external and internal factors will be modified and the resulting circulation patterns and magnitudes will be compared to the control run results. Specifically we will estimate the contribution (in terms of volume transport, sea surface elevation and circulation patterns) of non-linear advection, wind forcing and lateral boundary transport to the ocean features identified in the original results. From this we can estimate the relative importance of these factors to the SCS oceanography.

II. PRINCETON OCEAN MODEL

A. MODEL FEATURES

Coastal oceans and semi-enclosed seas are marked by extremely high spatial and temporal variabilities that challenge the existing prediction capabilities of numerical simulations. The POM is a time dependent, primitive equation circulation model in a three dimensional grid that includes realistic topography and a free surface. Developed at Princeton University (Blumberg and Mellor, 1987), the model was specifically designed to accomodate mesoscale phenomena, including the often non-linear processes (such as upwelling and eddy dynamics) commonly found in estuarine and coastal oceanography. Notable applications include simulation of the circulation in the Gulf of Mexico (Blumberg and Mellor, 1985), the Gulf Stream (Mellor and Ezer, 1991 and Ezer and Mellor, 1992), and the Kuroshio (Oey and Chen, 1991).

Wang et al. (1994) used the POM to study and quantify the dominant forcing present in the summer circulation of Hudson Bay. Using a sufficiently small grid size, they were able to determine the origin of observed mesoscale features and estimate the relative importance of wind and lateral transport on the hydrology of the summer circulation in the bay. Following the methodology used by Ezer and Mellor (1992) for the Gulf Stream, Wang et al. compared the output of several experiments, in each of which some contributing factor was isolated or modified, to the output of a control run, in which all factors were set to realistic values. Given that the primitive equations are deterministic, and assuming that non-linear interaction is minimal, they were able to quantify estimates of the effects of each isolated factor.

In this thesis, we use a 20 km horizontal grid resolution with 23 sigma levels in the vertical. The 20 km grid resolution is of the same magnitude as the estimated internal Rossby radius of deformation (estimated to be 16-20 km for typical layer depths) and so most rotational effects are adequately resolved. The model data were sampled on a 5 day interval (for 16 months) which will not reveal some short term and high frequency features. Tidal forcing was not included in this application of the model, since high

frequency variability of the circulation is not considered. River outflow is also not included. Monthly wind forcing is applied at every iteration and comes from a climatological data set (Hellerman and Rosenstein, 1983). Heat and salinity fluxes ($Q_{H,S}$) use the Haney-type restoring form (Haney, 1971). The seasonal variation in sea surface height, temperature, salinity, circulation and transport are well represented by the model data. From a series of numerical experiments, the qualitative and quantitative effects of non-linearity, wind forcing and lateral boundary transport on the SCS are analyzed, yielding considerable insight into the external factors affecting the regions oceanography.

The SCS application of the POM was established jointly at the University of Miami and the Naval Postgraduate School. Using a rectilinear grid with horizontal spacing of 0.179° by 0.175° (approximately 20 km resolution) and 23 vertical sigma coordinate levels, the model contains $125 \times 162 \times 23$ horizontally fixed grid points (Figure 5). The model domain is from 3.06° S to 25.07° N, and 98.84° E to 121.16° E, which encompasses the SCS and the Gulf of Thailand, and uses realistic bathymetry data from the Naval Oceanographic Office DBDB5 database (5 minute by 5 minute resolution).

1. Sigma Coordinates

Bathymetric irregularities create problems when incorporated in the standard, three dimensional orthogonal coordinate system. Model results near irregular bathymetric features tend to have large numbers of singularities which unrealistically affect adjacent grid values. To compensate for this, the POM uses a contour following coordinate system based on a scaling of the water depth at each horizontal grid location. The resulting sigma levels range from $\sigma = 0$ at the surface ($z = \eta$) to $\sigma = -1$ at the bottom ($z = -H$), with an arbitrary number of levels in between. In this application there are 23 sigma levels. The conversion between σ and z is:

$$\sigma = (z - \eta) / (H + \eta) \quad (1)$$

where H is the mean water depth and η is the time varying free surface height at grid

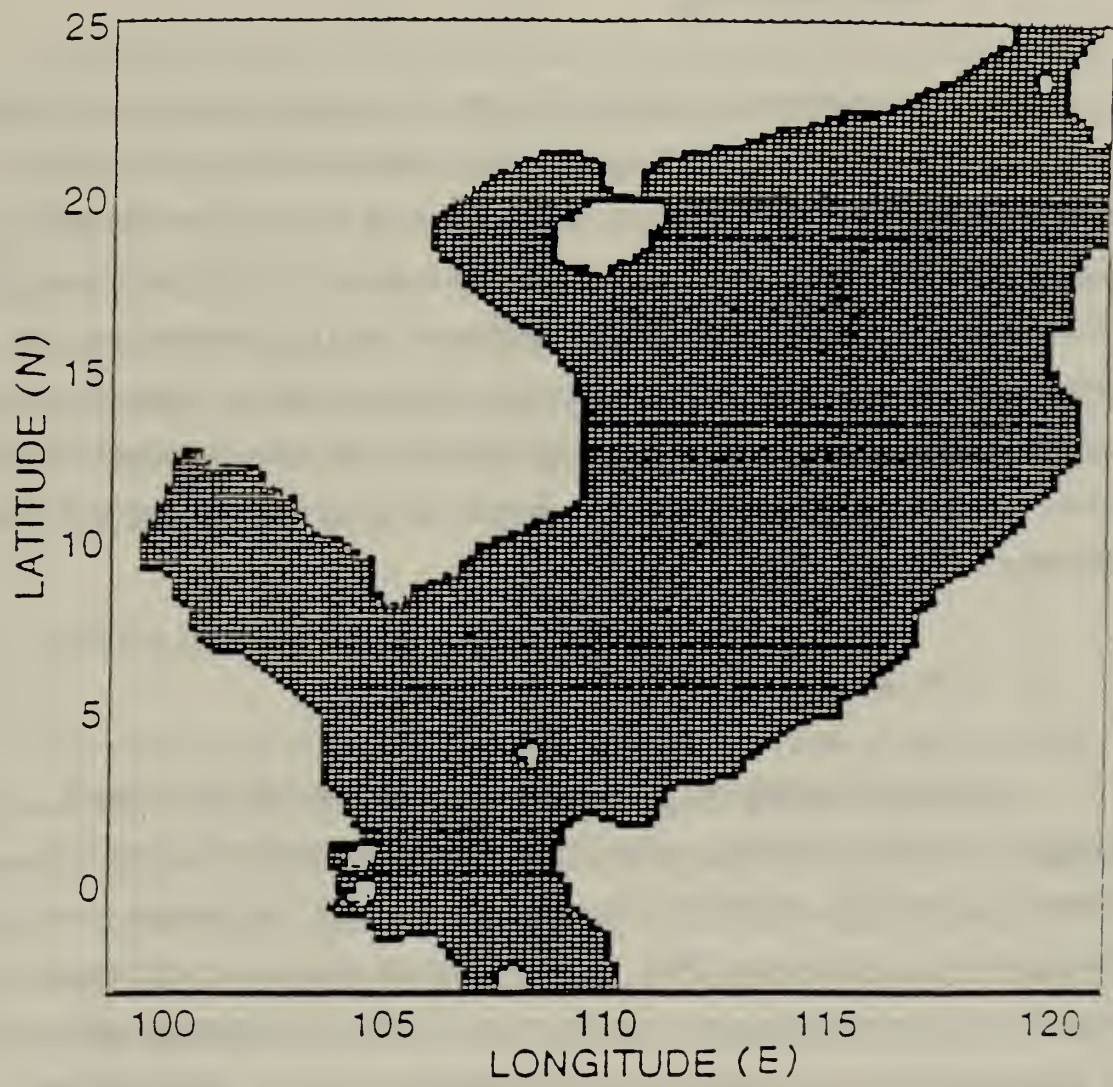


Figure 5. The model horizontal grid.

point (x,y). Use of the sigma levels as the vertical coordinates is not a perfect solution but allows improved resolution of boundary layers and is probably a necessary attribute in dealing with significant bathymetric variability (Mellor, 1992).

2. Finite Differencing

The governing equations are finite differenced in a leapfrog manner (centered in space and time) to produce the model output which includes the three components of velocity (u,v,w), temperature and salinity at each grid point as well as depth averaged velocity, sea surface height η and two quantities which characterize the turbulence. The horizontal finite differencing is explicit on an Arakawa C-grid and includes advection, horizontal diffusion, pressure gradient and Coriolis effect subroutines. Vertically, the finite differencing is implicit to eliminate time constraints that would be imposed by the sigma level vertical coordinates due to their dependence on the time varying free surface. (Blumberg and Mellor, 1985)

3. Mode Splitting

Computational limitations require that the external mode (two dimensional, barotropic, vertically integrated equations) be separated from the internal mode (three dimensional, baroclinic, vertical structure equations) by a technique known as mode splitting (Blumberg and Mellor, 1987). The external mode equations are obtained by integrating the internal mode primitive equations over depth. The barotropic solutions are then obtained prior to calculation of the internal mode equations. Mode splitting is applied with a barotropic time step of 25 seconds, based on the Courant-Friederichs-Levy (CFL) computational stability condition and the external wave speed; and a baroclinic time step of 900 seconds, based on the CFL condition and the internal wave speed. Separating the governing equations into internal and external mode algorithms permits calculation of the free surface elevation and velocity transport with no sacrifice in computational time from the calculation of the internal mode equations. Mode splitting

and the explicit/implicit numerical scheme are the two essential features that allow the model to predict the highly variable dynamics of coastal oceans and semi-enclosed seas.

4. Level Two Turbulence Closure

The equations used by the model are based on the Reynolds momentum and flux equations, where Reynolds stresses and flux terms (turbulence) require parameterization. Use is made of the Mellor-Yamada turbulence closure submodel (Mellor and Yamada, 1982) to provide the vertical eddy diffusivities for momentum, heat and salt ($K_{H,M}$) necessary to parameterize the vertical mixing processes. These coefficients are calculated as a function of the turbulent kinetic energy and the turbulence length scale (a characteristic length of turbulent motion at any point in space or time), thus linking diffusivity coefficients with estimates of turbulence. Use of these coefficients allows the model to simulate realistic Ekman surface layers and mixed layer dynamics.

B. MODEL GOVERNING EQUATIONS

The equations used to determine circulation and thermal structure are non-linear and incorporate a variable Coriolis parameter. Two approximations are used: the hydrostatic balance, which is that the weight of the fluid identically balances the pressure; and the Boussinesq approximation, that differences in density are neglected unless multiplied by gravity (to include buoyancy effects). Additionally, a latitudinal variation in the Coriolis parameter is accounted for by use of the β -plane approximation.

The governing, internal mode Reynolds momentum and conservation equations are presented here in z coordinates to better illustrate the interaction of variables.

1. The Continuity Equation

$$(\partial U/\partial x) + (\partial V/\partial y) + (\partial W/\partial z) = 0 \quad (2)$$

The conservation of mass equation with U the mean velocity in the x direction, V the mean velocity in the y direction and W the mean velocity in the z direction.

2. The Momentum Equations

$$(\partial U / \partial t) + \nabla \bullet U - fV = -(1/\rho_0)(\partial P / \partial x) + \partial / \partial z (K_M \partial U / \partial z) + F_X \quad (3)$$

$$(\partial V / \partial t) + \nabla \bullet V + fU = -(1/\rho_0)(\partial P / \partial y) + \partial / \partial z (K_M \partial V / \partial z) + F_Y \quad (4)$$

$$\rho g = -\partial P / \partial z \quad (5)$$

These are the momentum equations in x , y , and z directions respectively with ρ_0 the reference density, ρ the *in situ* density, g the gravitational acceleration, P the pressure, K_M the vertical eddy diffusivity of turbulent mixing of momentum, and f the Coriolis parameter. $F_{X,Y}$ represent a sum of processes occurring below the resolution of the model grid size.

3. The Temperature and Salinity Conservation Equations

$$(\partial \theta / \partial t) + \mathbf{V} \bullet \nabla \theta = \partial / \partial z (K_H \partial \theta / \partial z) + F_\theta \quad (6)$$

$$(\partial S / \partial t) + \mathbf{V} \bullet \nabla S = \partial / \partial z (K_H \partial S / \partial z) + F_S \quad (7)$$

Where θ is the potential temperature (or *in situ* temperature for shallow water conditions) and S is the salinity. $\mathbf{V} \bullet \nabla$ is the velocity vector multiplied with the divergence, K_H denotes the vertical eddy diffusivity for turbulent mixing of heat and salt, and $F_{\theta,S}$ represent a sum of processes occurring below the resolution of the model grid size.

4. Subgrid Scale Horizontal Mixing Processes

Processes that occur below the resolution of the model grid size are parameterized in terms of horizontal mixing processes:

$$F_X = \partial / \partial x (2A_M \partial U / \partial x) + \partial / \partial y (A_M (\partial U / \partial y + \partial V / \partial x)) \quad (8)$$

$$F_Y = \partial / \partial y (2A_M \partial V / \partial y) + \partial / \partial x (A_M (\partial U / \partial y + \partial V / \partial x)) \quad (9)$$

$$F_{\theta,S} = \partial/\partial x(A_H \partial/\partial x(\theta,S)) + \partial/\partial y(A_H (\partial/\partial y(\theta,S))) + R_{\theta,S} \quad (10)$$

where A_M and A_H are horizontal diffusivities required to damp small scale computational noise. The horizontal diffusivities are taken from the Smagorinsky formula (Smagorinsky,1963):

$$A_M = C\Delta x\Delta y(1/2) |\nabla \mathbf{V} + (\nabla \mathbf{V})^T| \quad (11)$$

with C the horizontal constant (chosen to be 0.2 for this application), \mathbf{V} the velocity vector at grid location (x,y) , and the superscript T denoting the transpose applied to the gradient of \mathbf{V} .

C. INITIAL CONDITIONS AND BOUNDARY CONDITIONS

1. Initial Conditions and Initialization

The model was integrated with all three components of velocity initially set equal to zero, and temperature and salinity specified by interpolating the climatology data (Levitus,1984) to each model grid point. The model year consists of 360 days (30 days per month), day 361 corresponds to 1 January. It was found that 90 days were sufficient for the model to reach quasi-steady state under the imposed condition (Figure 6). In order to capture the winter monsoon to summer monsoon transition, the model was started in the fall, day 300, and run to day 390 to establish the quasi-steady state. After day 390, the model was run another 450 days for each experiment.

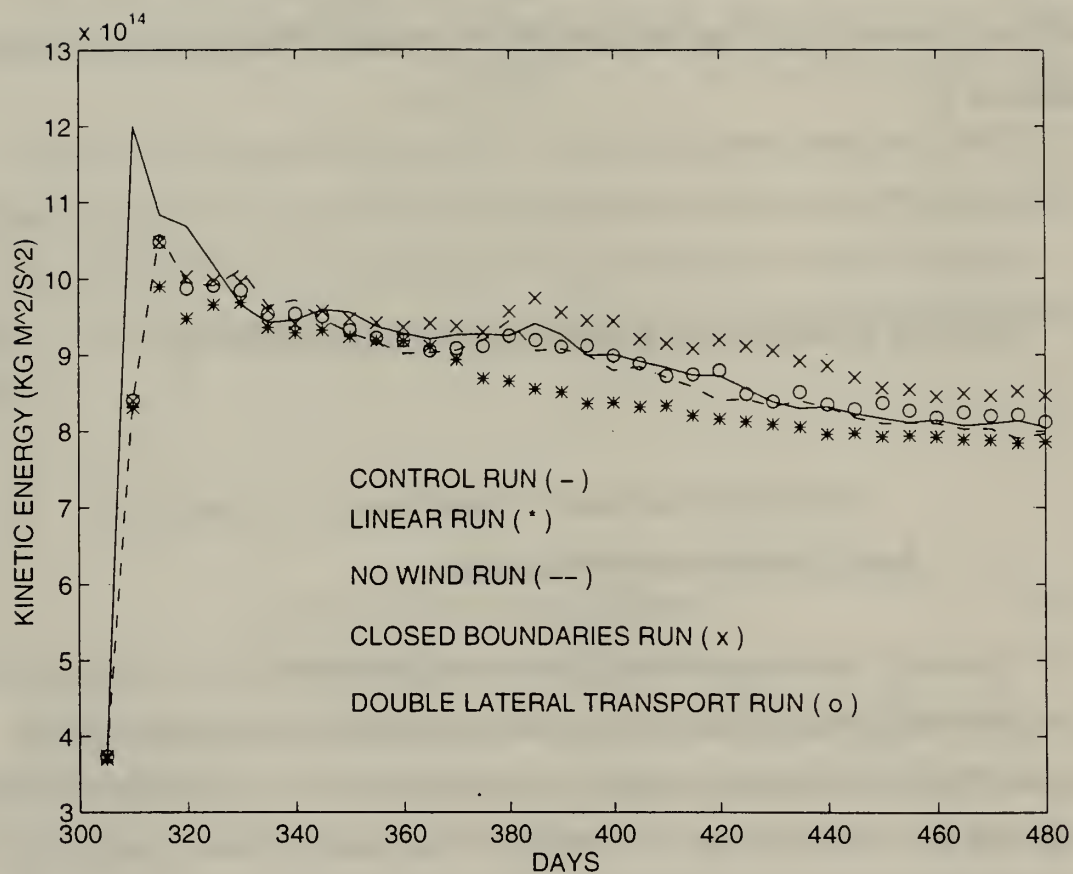


Figure 6. Temporal variation of the total kinetic energy. After day 750, the model is considered adjusted.

2. Bottom Boundaries

The bottom boundary conditions are calculated by:

$$\rho_0 K_M \{ \partial U / \partial z, \partial V / \partial z \} = (\tau_{bx}, \tau_{by}) \quad (12)$$

where (τ_{bx}, τ_{by}) is the bottom frictional stress vector, determined by matching the velocity at the nearest grid point with the logarithmic law of the wall:

$$\tau_b = \rho_0 C_D |V_b| V_b \quad (13)$$

where V_b is the velocity vector at the boundary and the drag coefficient C_D is specified as 0.0025 (Blumberg and Mellor, 1985).

D. FORCING

1. Atmospheric Forcing

The atmospheric forcing for the SCS application of the POM includes mechanical and thermal forcing. The mechanical forcing is depicted by

$$\rho_0 K_M \{ \partial U / \partial z, \partial V / \partial z \} = (\tau_{0x}, \tau_{0y}) \quad (14)$$

where (τ_{0x}, τ_{0y}) are the two components of the wind stress vectors, which were taken from the monthly mean climatological wind stress data of Hellerman and Rosenstein, 1983.

The middle of the month values were extrapolated to each day. The wind stress has a typical magnitude of 1-2 dynes/cm² (see Figure 3). Between the monsoon seasons the wind varies with latitude and time, leading to a complicated distribution of wind stress.

Surface thermal forcing is depicted by

$$K_H \partial \theta / \partial z = \alpha_1 (Q_H / \rho C_p) + \alpha_2 C (\theta_{OBS} - \theta) \quad (15)$$

$$K_S \partial S / \partial z = \alpha_1 Q_S + \alpha_2 C (S_{OBS} - S) \quad (16)$$

where θ_{OBS} and S_{OBS} are the observed potential temperature and salinity, C_p is the specific heat, and Q_H and Q_S are surface heat and salinity fluxes, respectively. The time constant C is the reciprocal of the restoring time period for a unit volume of water. The

parameters (α_1, α_2) are (0,1)-type switches: $\alpha_1 = 1, \alpha_2 = 0$, would specify only flux forcing is applied; $\alpha_1 = 0, \alpha_2 = 1$, would specify that only restoring type forcing is applied.

In this study, the surface thermal forcing is determined solely by restoring forcing, $\alpha_1 = 0$ and $\alpha_2 = 1$ in (15)-(16). The relaxation constant C is taken to be 0.7 m/d, which is equivalent to a relaxation time of 43 days for an upper layer 30 m thick (Chu et al., 1996). Therefore, in the SCS application of the POM, the heat and salinity surface boundary conditions do not include real time flux terms (Q_H, Q_S) and the equations act solely to relax the surface temperature and salinity to the values interpolated from the climatological data (Levitus, 1984). The net effect is to prevent any deviation from climatology and ensure that the SCS acts as a heat source.

2. Lateral Boundaries

Closed lateral boundaries, the extent of the modeled ocean bordered by land, were incorporated using a free slip condition for velocity and a zero gradient condition for temperature and salinity. No advective or diffusive heat, salt or velocity fluxes occur through these boundaries.

Open lateral boundaries are problematic. The volume transports through the open boundaries at the Balabac Channel, Mindoro Strait, and Strait of Malacca are assumed zero in this thesis; only the Luzon Strait, Formosa Strait, and Gasper/Karimata Strait were open. The hydrographic data of the Naga Report (Wyrki, 1961) was utilized to specify monthly boundary transport values. Barotropic velocities (V_n) at the open boundaries are obtained by:

$$V_n = (\text{Transport}) / \int_l H \, dl \quad (17)$$

where the seasonal transport is given in Table 1, l is the boundary width, n is normal direction to the boundary and H is the water depth. Baroclinic velocities at the boundaries are then obtained by (Chu et al., 1996):

$$V_{nBC} = V_n (e^\sigma / (1 - e^{-1})) \quad (18)$$

Table 1: The bi-monthly variation of volume transport (Sv) at the open boundaries. The values were taken from Wyrтки (1961).

Month	Feb.	Apr.	Jun.	Aug.	Oct.	Dec.
Gasper & Karimata Straits (Eastward Positive)	4.4	0.0	-4.0	-3.0	1.0	4.3
Luzon Strait (Eastward Positive)	-3.5	0.0	3.0	2.5	-0.6	-3.4
Formosa Strait (Northward Positive)	-0.9	0.0	1.0	0.5	-0.4	-0.9

Temperature and salinity are likewise prescribed from data when the transport is specified to be flowing into the model domain. When the transport is flowing out of the model, the advection gradient equation:

$$\partial/\partial t (\theta, S) + U_n \partial/\partial n (\theta, S) = 0 \quad (19)$$

is solved for both barotropic and baroclinic modes where the subscript n is the coordinate normal to the boundary.

III. EXPERIMENTS

Our approach was to carry out four numerical experiments and compare them to a control run. All runs were completed for the same 16 month period encompassing both summer and winter monsoons, and, except as specified below, utilized the same initial conditions and boundary conditions. For the purposes of analysis, summer is considered to be from May to August and winter is considered to be from November to March, corresponding to the maximums in climatological wind forcing. Each experiment is a sensitivity study in which we independently examine the effects of (1) non-linear advection, (2) wind stress, (3) zeroing lateral transport at the open boundaries and (4) doubling the amount of lateral transport at the open boundaries. The difference between the experiment result and control run result at each grid point and time instance will be due to the factor isolated in that experiment. Integrating the linear difference over the monsoon season provides a quantitative measure of the isolated or modified parameter for that season. Both general features and specific characteristics of the SCS circulation will be identified from the control run and analyzed for the effect of forcing factors.

An essential assumption for later analysis is that the flow is nearly linear in the SCS. If this is valid, then the contribution of the forcing field eliminated or modified can be determined by simple differencing. The second run was designed to test this assumption. The primitive equations used by the model to determine the prognostic variables were modified so that the non-linear advective terms were set equal to zero. The model was run in this condition until quasi-steady state was achieved, then run prognostically to collect data.

To simulate the seasonal circulation in the SCS without winds, the control run was repeated from day 300 with wind stress forcing set to zero over the model's spatial domain. After reaching quasi-steady state, the model was run prognostically in this condition and data was collected for comparison to the control run. The difference between this data and that from the control run is thus exclusively due to the effect of daily wind forcing. The fourth and fifth runs tested the effect of lateral boundary transport on the SCS, first by closing all open boundaries (Run 4) and then by doubling

the historical transport values (Run 5). The same procedure was followed as in previous runs, with some additional attention given to conserving mass.

IV. RESULTS

First we examine the thermal structure, sea surface elevation and circulation patterns that constitute the SCS oceanography. Various oceanographic features will be identified from the control run for subsequent analysis of volume transport. Then, for each sensitivity study, these features and the general circulation patterns will be analyzed for qualitative differences in structure from the control run results. From this information we will compare kinetic energies and estimate the quantitative linear differences in sea surface elevation, velocities and volume transport. This will allow us to draw conclusions regarding the contribution of the studied parameters to individual oceanographic features. An important assumption is made that the differences are linear, i.e., higher order terms and interactions are negligible and can be ignored.

A. CONTROL RUN

1. Summer Monsoon

During summer months (May to August) winds flow from the southwest and the surface circulation is generally anticyclonic, with inflow from the southern boundary and outflow through the northern boundaries (Figure 7). Velocities reach 1 m/s at the peak of the monsoon (Figure 7b) with a clearly visible western intensification of current and substantial small scale eddy activity over the deep basin. The average sea surface elevation for the summer varies from 10 to 20 cm in the southernmost portion of the SCS (Figure 8a), and is fairly uniform elsewhere.

In general the temperature and salinity profiles reflect the existence of two distinct water masses in the SCS throughout the year, consistent with the Naga Report analysis (Wyrki, 1961). In the north the surface layers are influenced by the inflow of North Pacific water and thus are uniformly cold and saline with relatively shallow layer depths. In the south the tropical climate and inflow of water from the shallow Java Sea cause the

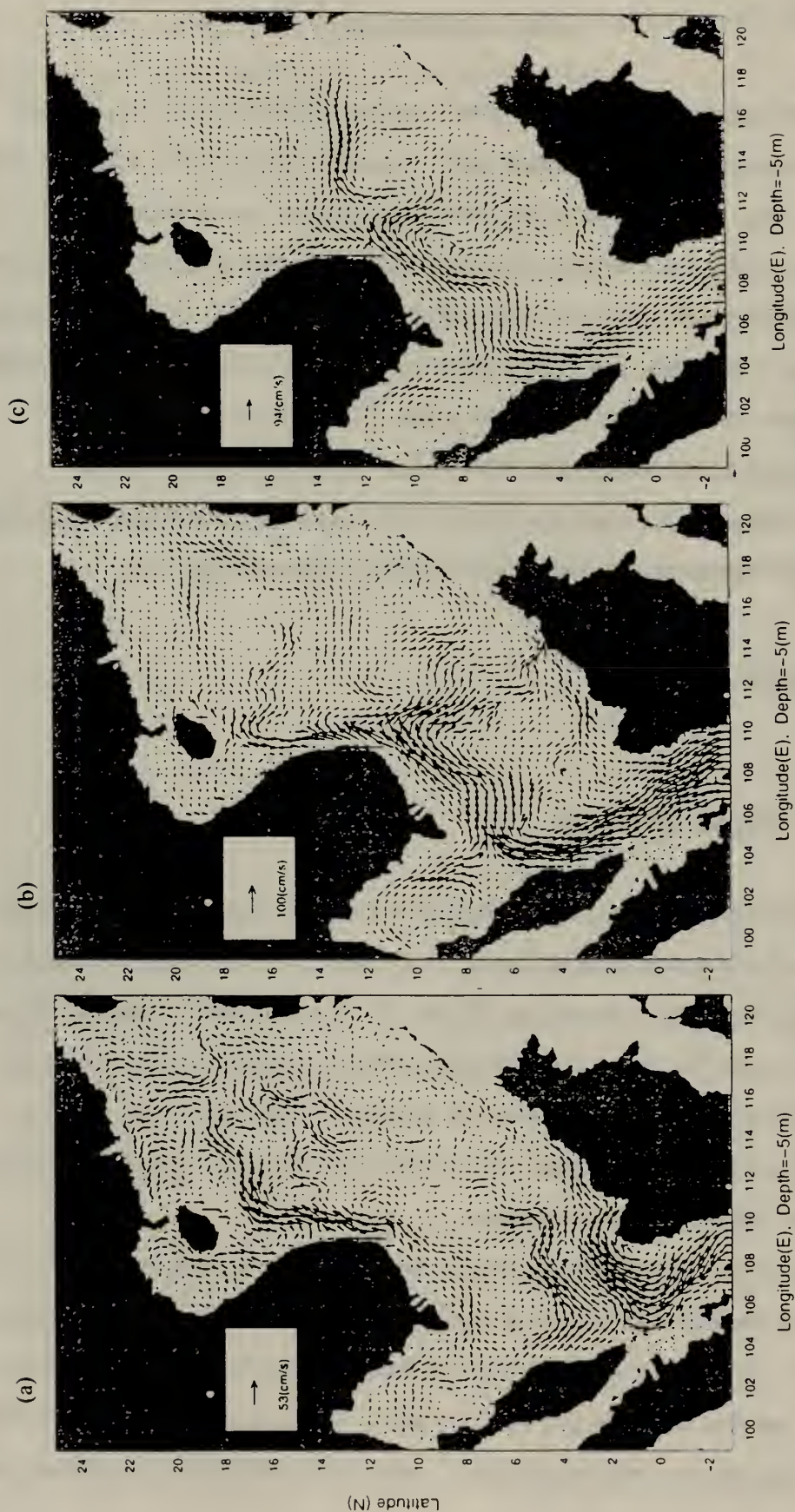
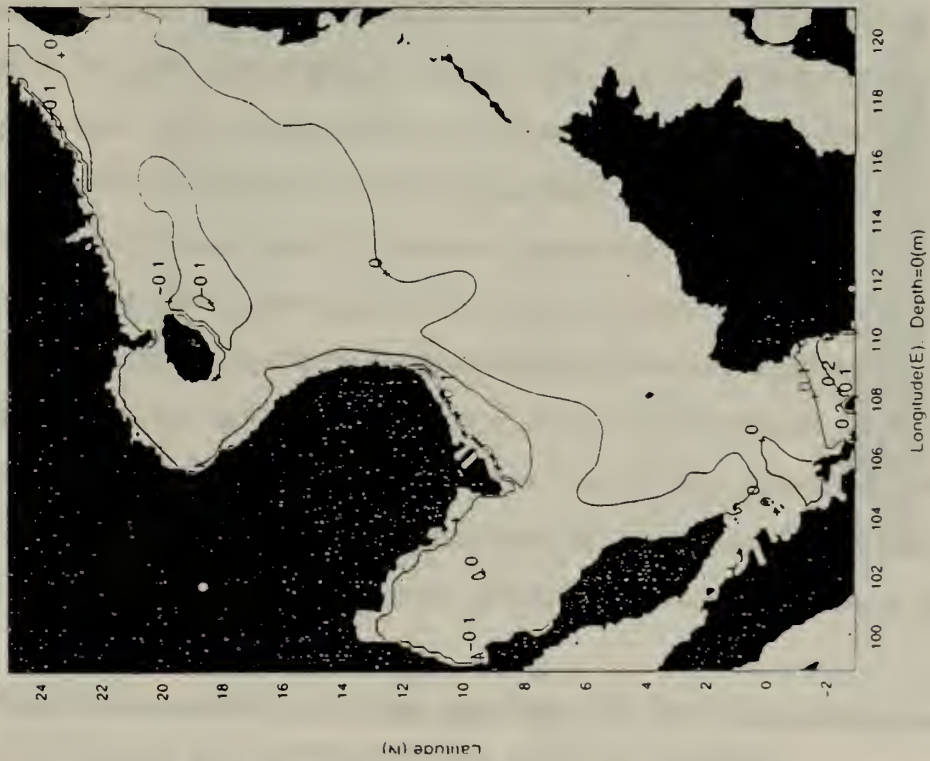


Figure 7. Near surface circulation for control run during summer (a) May 15, (b) July 15, (c) September 15.

(a) SUMMER MONSOON SSH RUN1 (m)



(b) WINTER MONSOON SSH RUN1 (m)

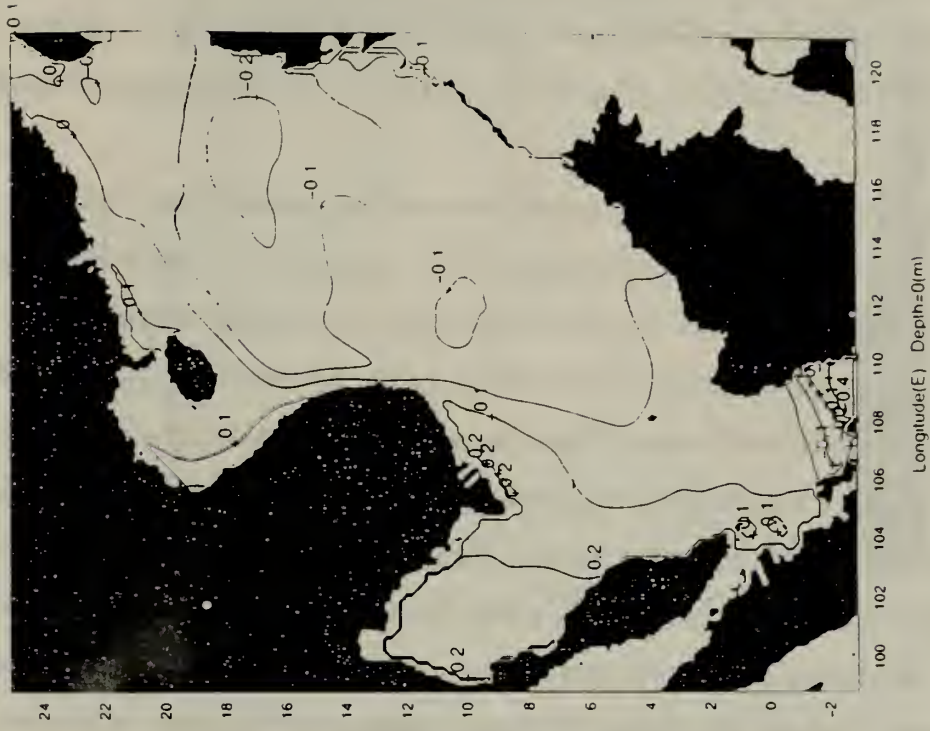


Figure 8. Sea surface elevation (m) of the control run averaged over (a) summer monsoon, (b) winter monsoon.

water masses to be fresh and warm and slightly deeper (Figure 9a). The SCS summer thermocline averages between 30 and 50 m and the halocline exists from 100 to 150 m. Model sea surface temperature (SST) varies with latitude and nearby oceanographic features (Figure 10a), but matches satellite observed sea surface temperatures (Figure 11a).

As described by Li (1994), the model simulates the climatological historical observations of the surface circulation (Figure 4). At the start of the summer monsoon (mid-May) the near surface flow from the Gaspar and Karimata Straits turns sharply to the east and follows the shoreline of Borneo (Figure 7a). By the middle of the summer monsoon, there is an intensification of flow along the coast of Malaysia and the current at all depths in this area has turned northwestward (without entering the Gulf of Thailand). Figure 12a shows that this current exists from the surface to 50 m with a core velocity that averages 45 cm/s. A northward shelf current is also visible with average velocities of 15 cm/s. As the current flows northward it follows the 150 m isobath to the coast of Vietnam where it becomes the summer Vietnam Coastal Jet (VCJ). The VCJ continues north along the isobaths almost to the coast of Hainan before turning east towards the Luzon Strait. This current reaches a maximum velocity of 80 cm/s at the peak of the monsoon season and averages 40 cm/s during the summer (Figure 13a), additionally a equatorward counter current occurs along the shelf break in mid-summer with velocities less than 10 cm/s (not shown). The average core velocity corresponds to a volume transport of 5.5 Sv (Table 2). An examination of the temperature profile across the jet indicates that upwelling occurs inshore of the current (Figure 14a) consistent with Ekman theory. The colder, denser water nearshore, combined with the high velocity current relative to offshore current speeds, results in baroclinic instability. The southwestward turn that occurs at 10° N and bisects the basin along its minor axis (Figure 7b), demonstrates a coastal jet meander behavior as a result of the baroclinic instability in this region.

A second cross-basin current occurs at the surface at 16° N in the middle of summer (Figure 15a), with current speeds in excess of 20 cm/s at the surface and 10-15 cm/s down to 600 m depth. This current begins the summer as a meandering extension of

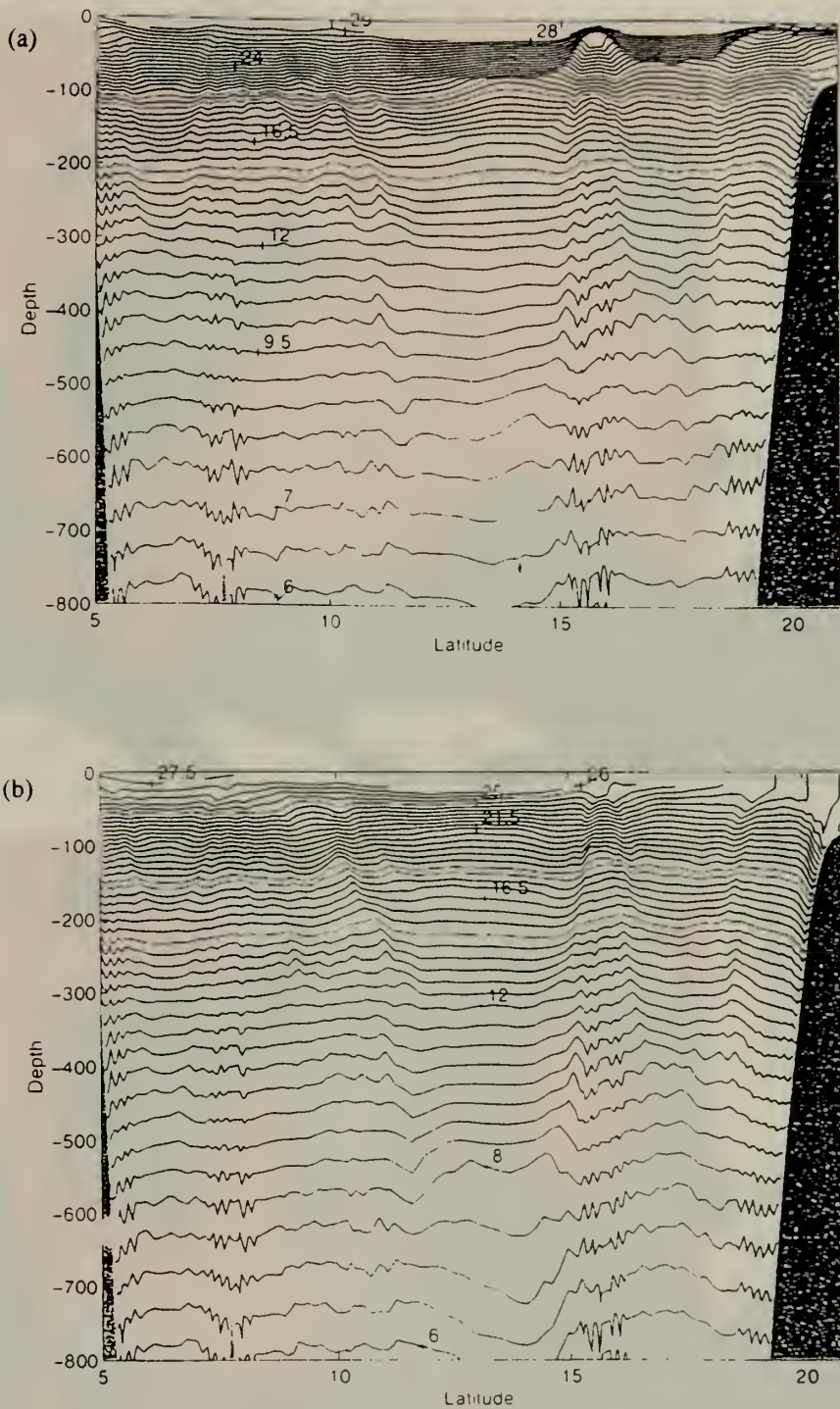
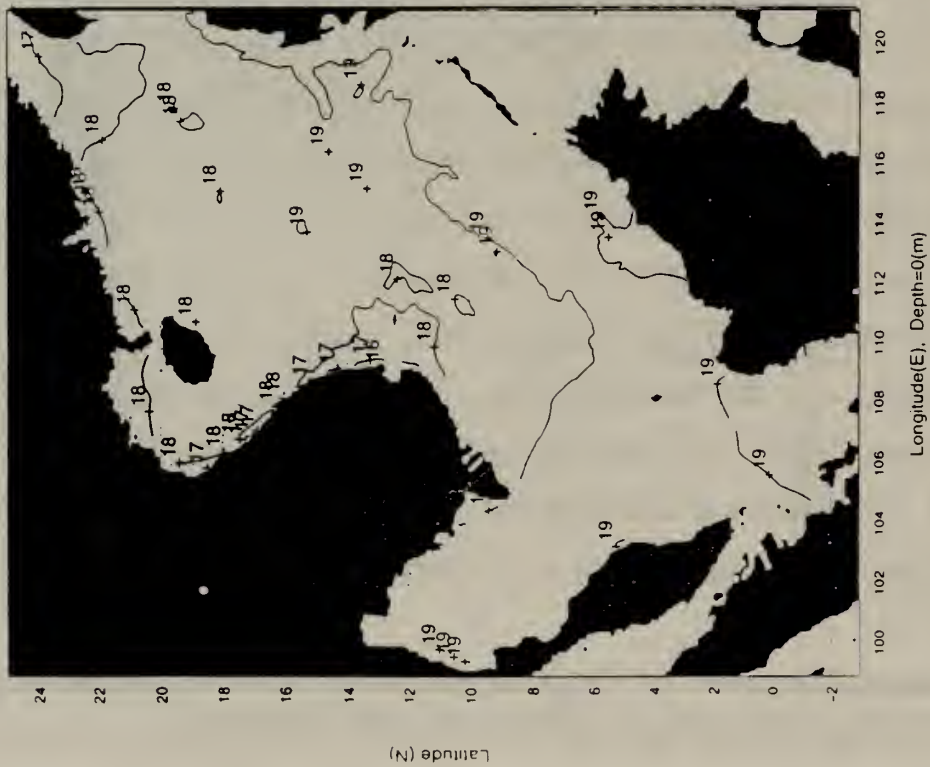


Figure 9. Temperature (°C) for control run at 114° E longitudinal cross section averaged over (a) summer monsoon, (b) winter monsoon.

(a) SUMMER MONSOON Run1 temp



(b) WINTER MONSOON Run1 temp

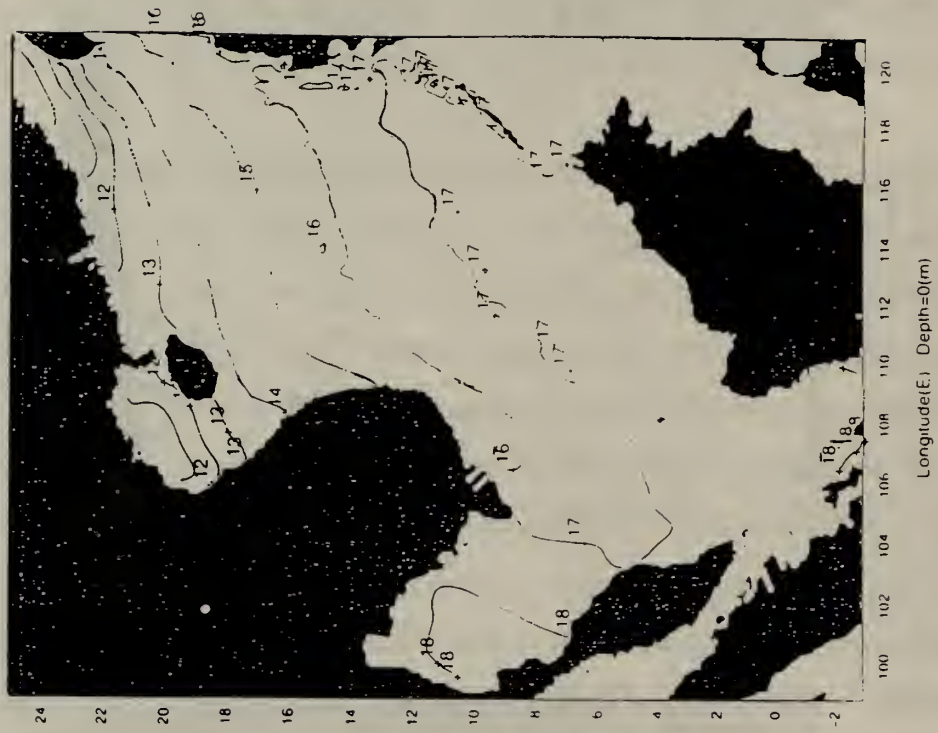
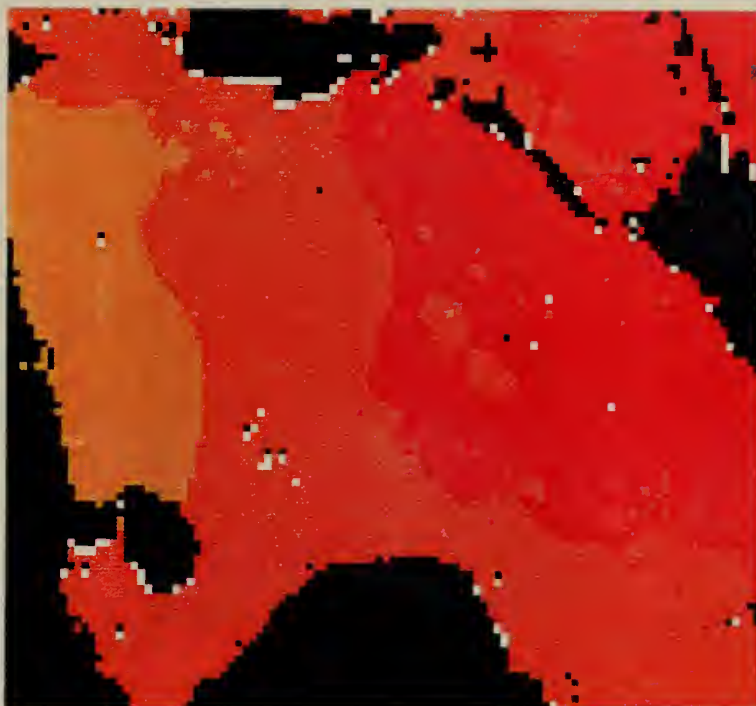


Figure 10. Sea surface temperatures ($^{\circ}\text{C}$) of the control run averaged over
(a) summer monsoon, (b) winter monsoon.



(a)



(b)

Figure 11. Satellite imagery of South China Sea sea surface temperatures for (a) 17 May 1995, (b) 7 January 1995. The warmer water is darker.

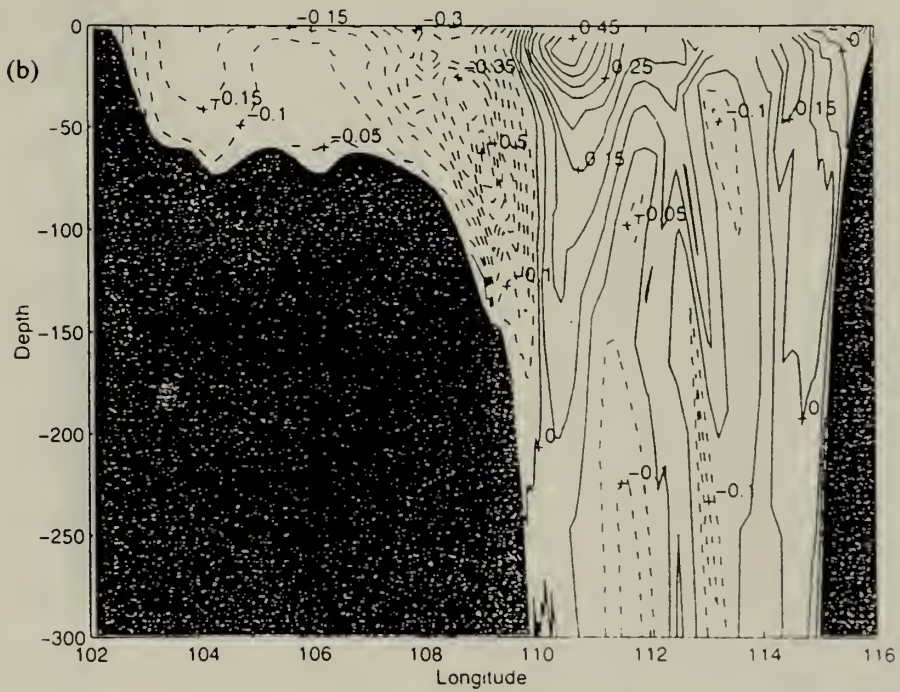
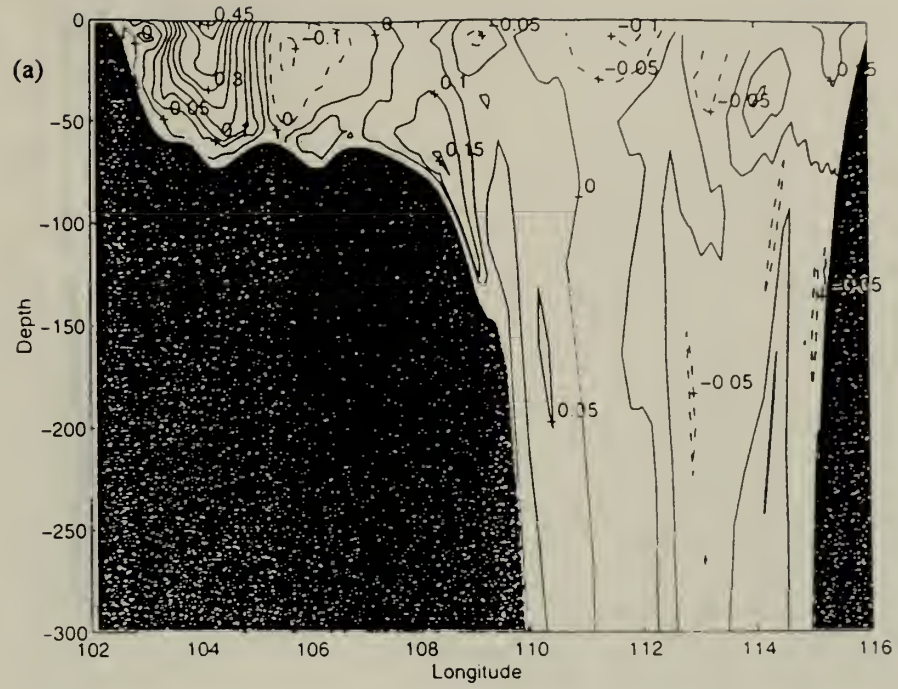


Figure 12. V component of velocity (m/s) of control run at 6° N latitudinal cross section averaged over (a) summer monsoon, (b) winter monsoon.

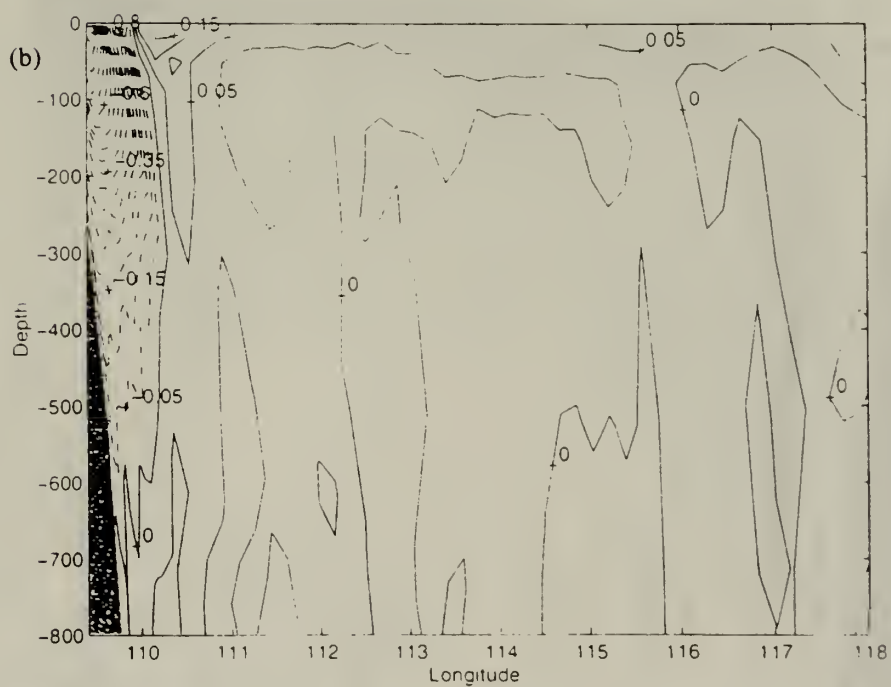
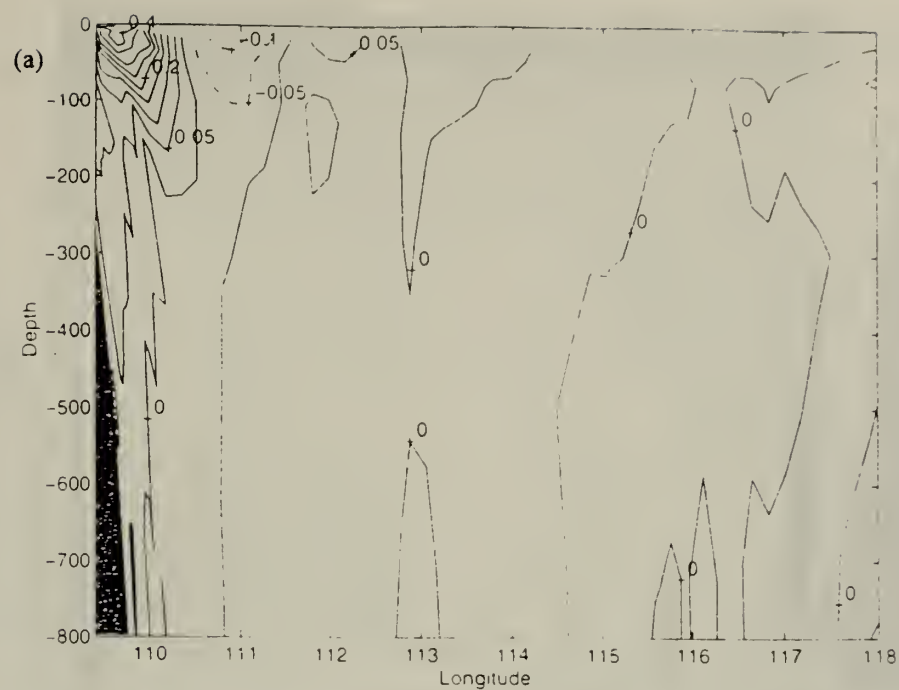


Figure 13. V component of velocity (m/s) of control run at 13° N latitudinal cross section averaged over (a) summer monsoon, (b) winter monsoon.

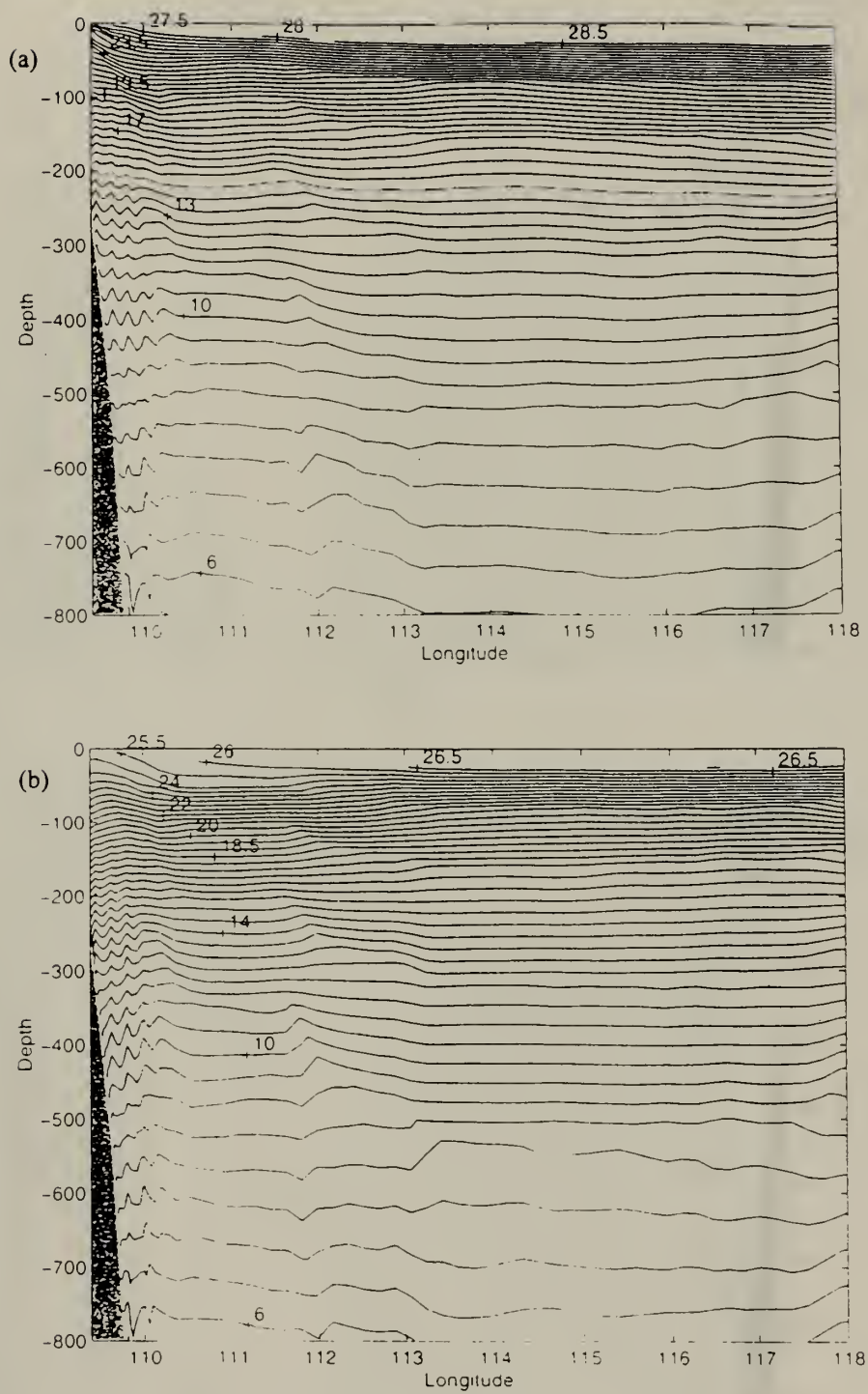


Figure 14. Temperature (°C) for control run at 13° N latitudinal cross section averaged over (a) summer monsoon, (b) winter monsoon.

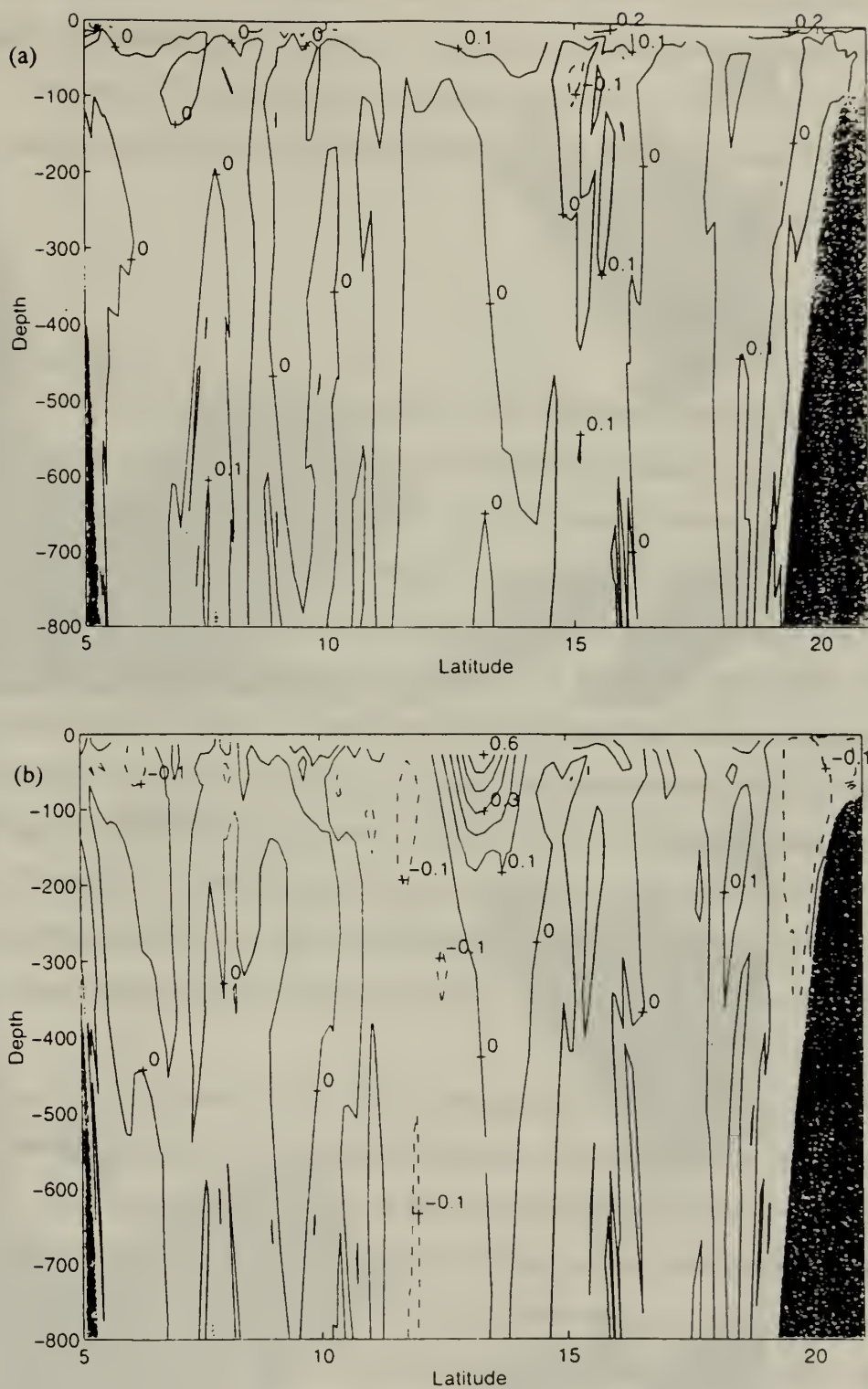


Figure 15. U component of velocity (m/s) of control run at 114° E longitudinal cross section for (a) July 15, (b) September 15.

the VCJ, flowing eastward toward the Luzon Strait (Figure 7a). As time progresses, this cross-basin current migrates south and intensifies, reaching a latitude of approximately 12° N with a core current velocity of 60 cm/s by the end of summer (Figure 14b). Examination of the total volume transport for summer shows that this current carries 13-18 Sv across the basin (Figure 16a).

2. Winter Monsoon

From November to March the winter monsoon system dominates the SCS, with the winter Asian high pressure system resulting in strong winds from the northeast. The general circulation pattern becomes cyclonic. Inflow from the Bashi Channel (the Kuroshio intrusion) and Strait of Taiwan force currents southwest along the 150 m isobath of the Asian continental shelf, then south along the coast of Vietnam and eventually out through the Gasper and Karimata Straits in the south. Sea surface heights for the winter monsoon show a depression in the northern portion of the deep basin with an increase in height as the southern boundary is approached (Figure 8b). Average temperature and salinity profiles for the winter monsoon are very similar to those for the summer: cold and saline water in the north, warm and fresh water in the south (Figure 9b), and considerable east/west variation depending on latitude. The temperature profile reflects the latitudinal variation in SST with some sloping of the horizontal isotherms in the west (Figure 10b).

Western intensification of the general cyclonic circulation pattern results in the winter monsoon version of the VCJ. From the south coast of Hainan, the current intensifies as it flows from north to south along the Vietnam coast (Figure 17b). Average current speeds are 80 cm/s in the core with little variability during winter months. Average southward volume transport for the winter monsoon is approximately 10.6 Sv (Table 2). The current is coherent from the surface down to 500 m depth along the narrow shelf break (Figure 13b). A shallow surface counter current develops late in the winter monsoon adjacent to the VCJ and persists through the transition period to the start of the summer monsoon (Figure 17c and Figure 7a). Analysis of the vertical

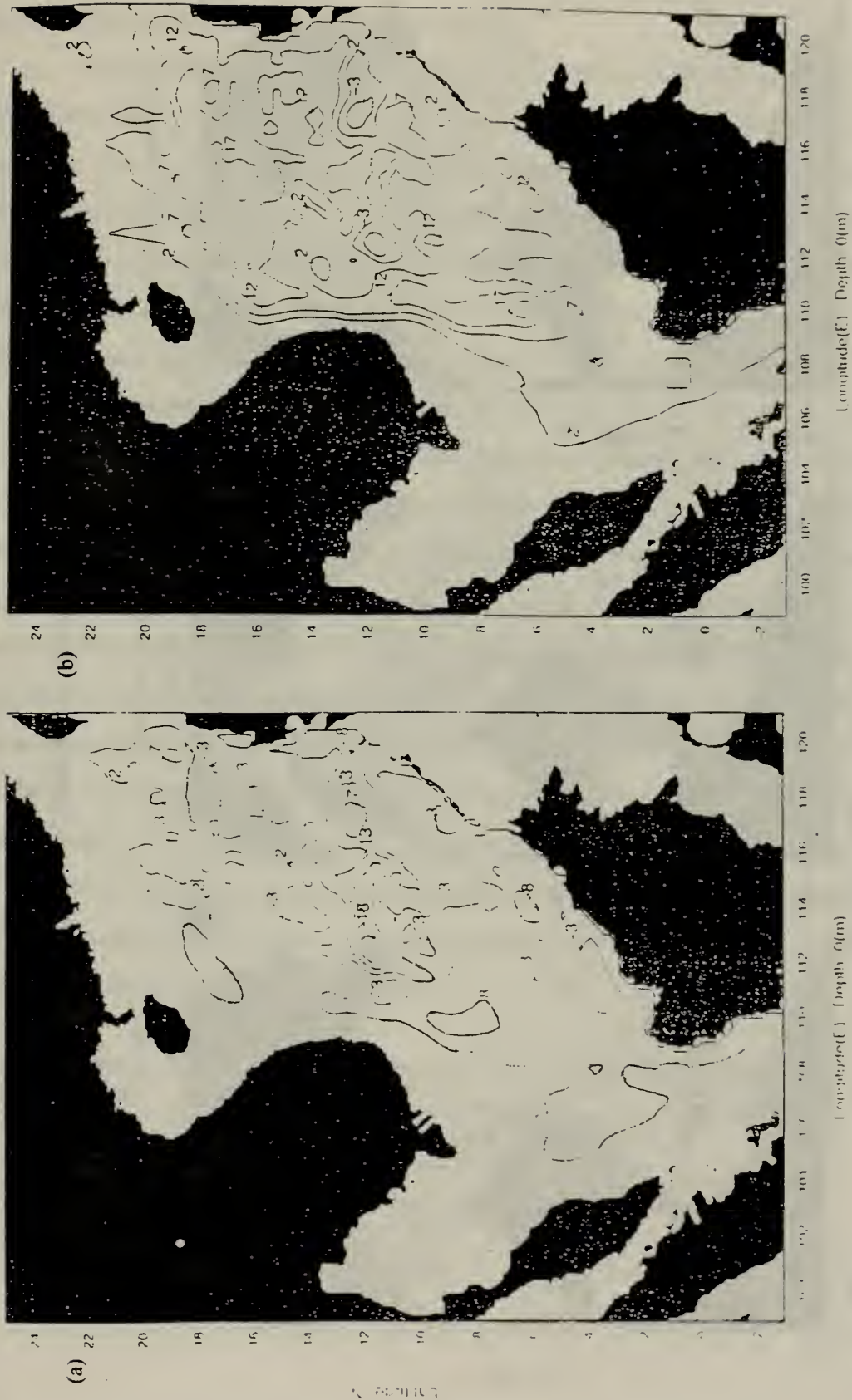


Figure 16. Volume transport (Sv) of control run averaged over (a) winter monsoon, (b) summer monsoon.

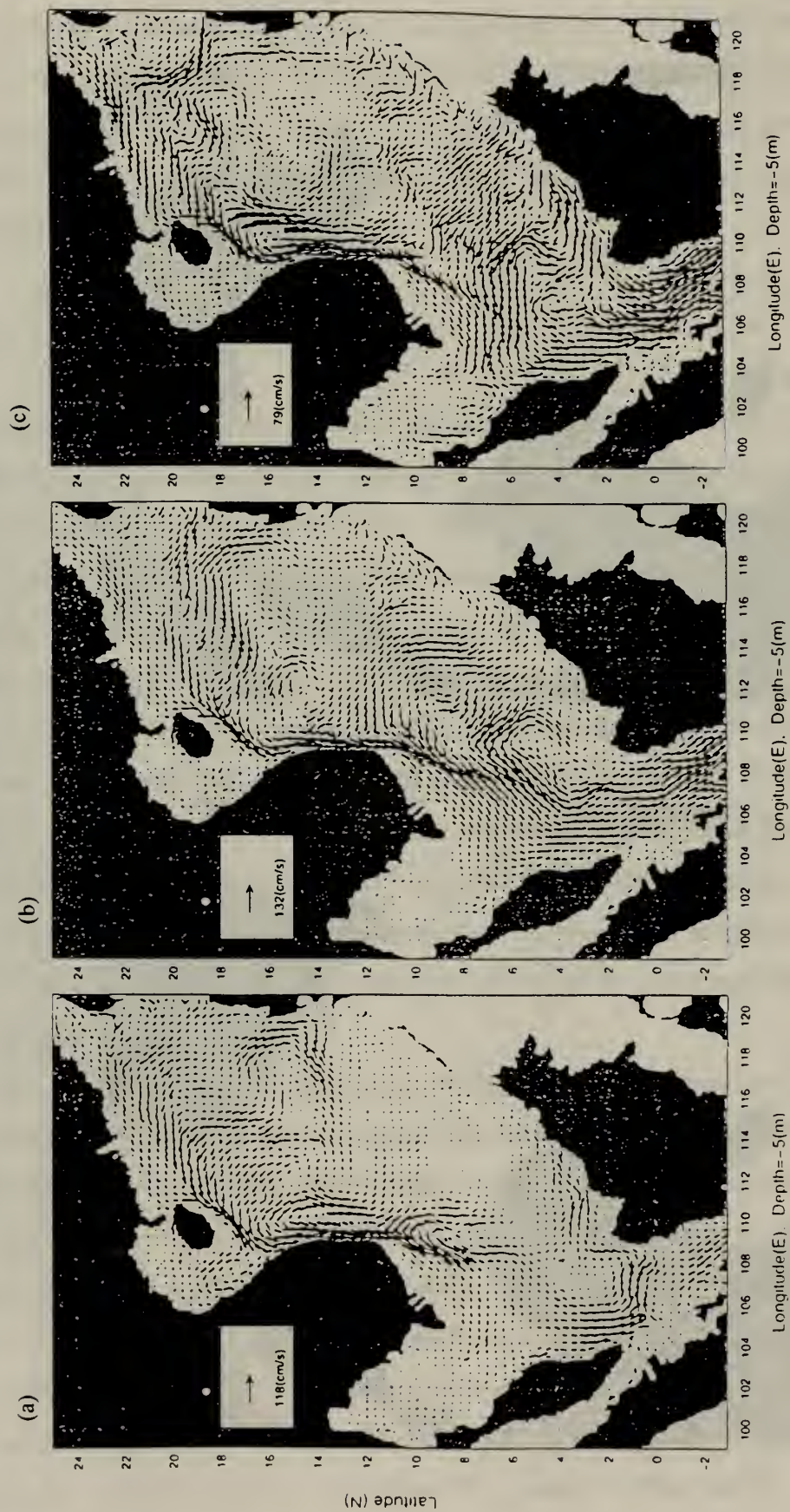


Figure 17. Near surface circulation for control run during winter (a) October 15, (b) December 15, (c) March 15.

thermal structure in this vicinity (Figure 14b) shows colder water near the surface and a general deepening of the isotherms below 50 m.

As the winter circulation pattern progresses, near surface currents along the coast of Borneo begin to turn to the northwest, eventually flowing directly away from the coastline over the Sunda Shelf and southern portions of the deep basin. Additionally, the southward VCJ begins to interact with the topography and is increasingly steered to the east (Figure 18). The combination of these effects eventually results in the formation of a mesoscale cyclonic topographic gyre, termed the Natuna Island Gyre (NIG). In the north, an anticyclonic gyre begins to form between Hainan and Vietnam (Figure 17c). These features are consistent with the observations of late winter surface circulation described earlier (Figure 4a). As shown in Figure 18, NIG has an average core velocity of 50 cm/s, which is at 5 m depth on the north side of the gyre (flowing away from the coast of Borneo) and at 50 m depth on the south side (proceeding towards Borneo). A latitudinal cross section shows that the core is similarly deeper on the west side of the gyre, and a surface phenomenon on the east side (Figure 12b). Note the vertical velocity shear on the east and north sides of the gyre, this feature also demonstrates baroclinic instability. The gyre shows little variability during the winter, with maximum swirl velocities of 60 cm/s at the peak of the monsoon but no variation in position. The velocities correspond to approximately 5 Sv volume transport. The anti-cyclonic gyre in the north forms along 110° E longitude and has a core velocity of 60 cm/s (Figure 19a). The temperature profile across this feature shows evidence of winter upwelling (Figure 19b) consistent with the observations of Chen et al. (1982).

Table 2: North/south volume transport (Sv) of individual features of SCS oceanography.

Feature	Control Run Value
Summer Vietnam Coastal Jet	5.5
Winter Vietnam Coastal Jet	10.6
Natuna Island Gyre (winter)	5.0

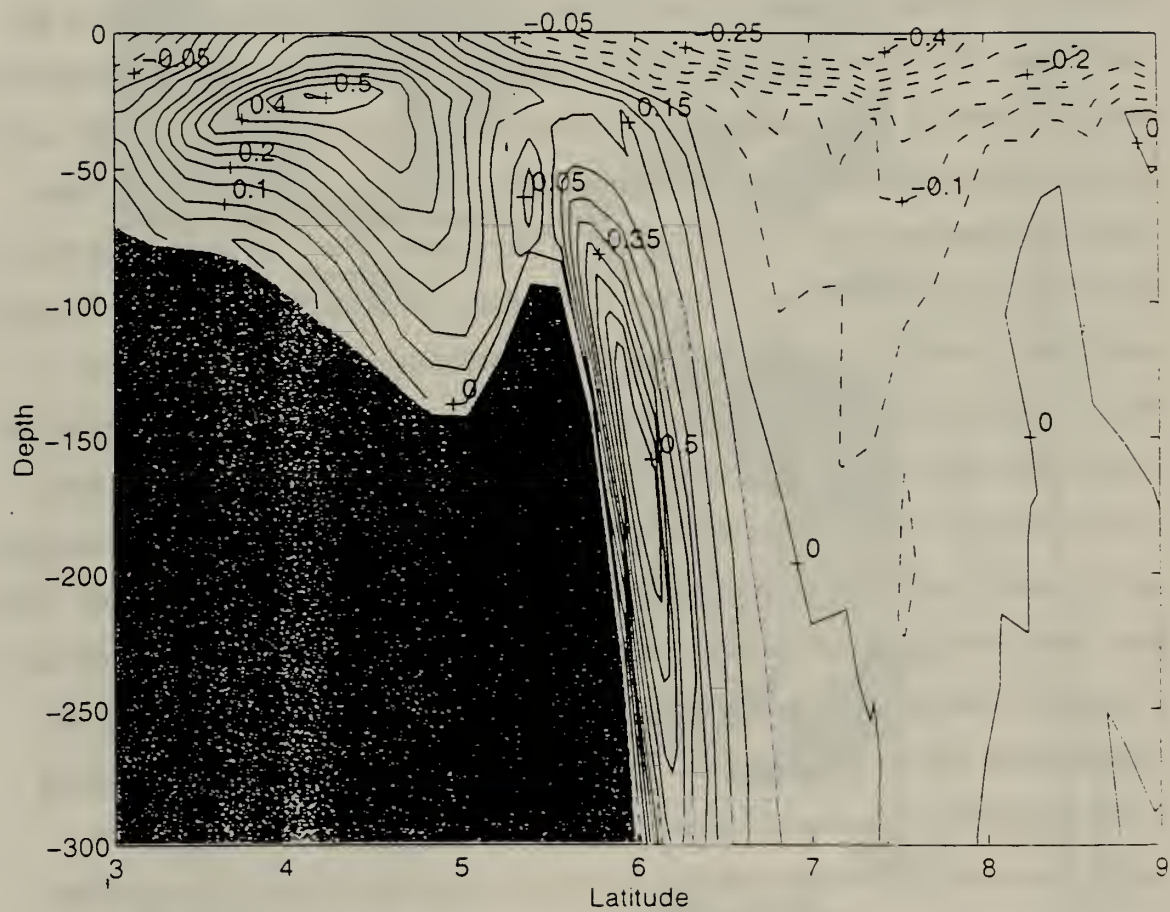


Figure 18. U component of velocity (m/s) of control run at 110° E longitudinal cross section averaged over winter monsoon.

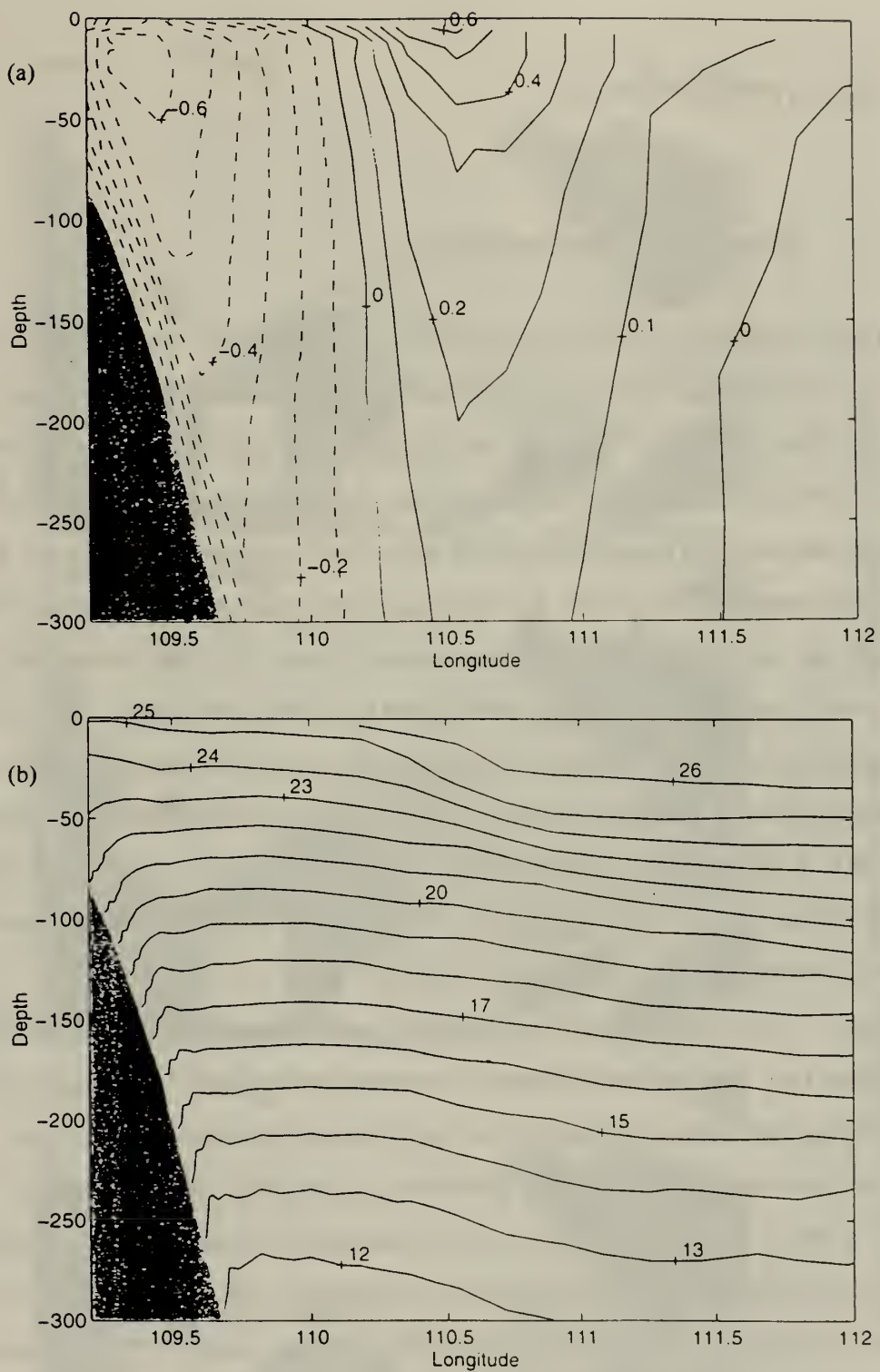


Figure 19. (a) V component of velocity (m/s) for control run and (b) temperature (°C) profile of control run for 15 March at 15° N latitudinal cross section.

B. SENSITIVITY STUDIES

1. Effects of non-linearity (Run 2)

The first sensitivity study involved modifying the dynamic equations so that there were no non-linear advective terms, but otherwise used the same parameters as the control run. The near surface velocities for mid-winter and mid-summer are shown in Figures 20 and 21 to illustrate the similarity to the control run results (Figures 7,17). Visual comparison of the linear run data with the control run shows that there are no apparent differences between them. Similar results were obtained for sea surface height data. There are specific instances when non-linearity is very important in terms of the volume transport and kinetic energy of eddies, and upwelling phenomena. When energy differences are examined for the winter monsoon, the results show that the volume kinetic energy increases when non-linear advection is removed from the momentum equations (Figure 22a). Additionally, an examination of differences in surface temperature (Figure 23) shows thin bands of effect near the eastern boundary in winter and western boundary in summer, with similar results obtained for salinity.

Figure 24 is a plot of the difference in total volume transport between the control run and linear run. The positive difference in transport located between Vietnam and Palawan during the summer circulation is in the vicinity of the coastal jet meander observed in the control run. Removing advective processes decreases the volume transport by nearly 10 Sv in this region which illustrates the importance of non-linearity to baroclinic instabilities. This is consistent with the theory that mesoscale features dependent on baroclinic instabilities can extract energy from the mean flow and increase the total transport of the system (Pond and Pickard, 1983). Conversely, the cross basin flow that peaks late in the summer at 13° N (and its associated small scale anticyclonic eddies) shows increases in total volume transport when non-linearity is removed, suggesting that

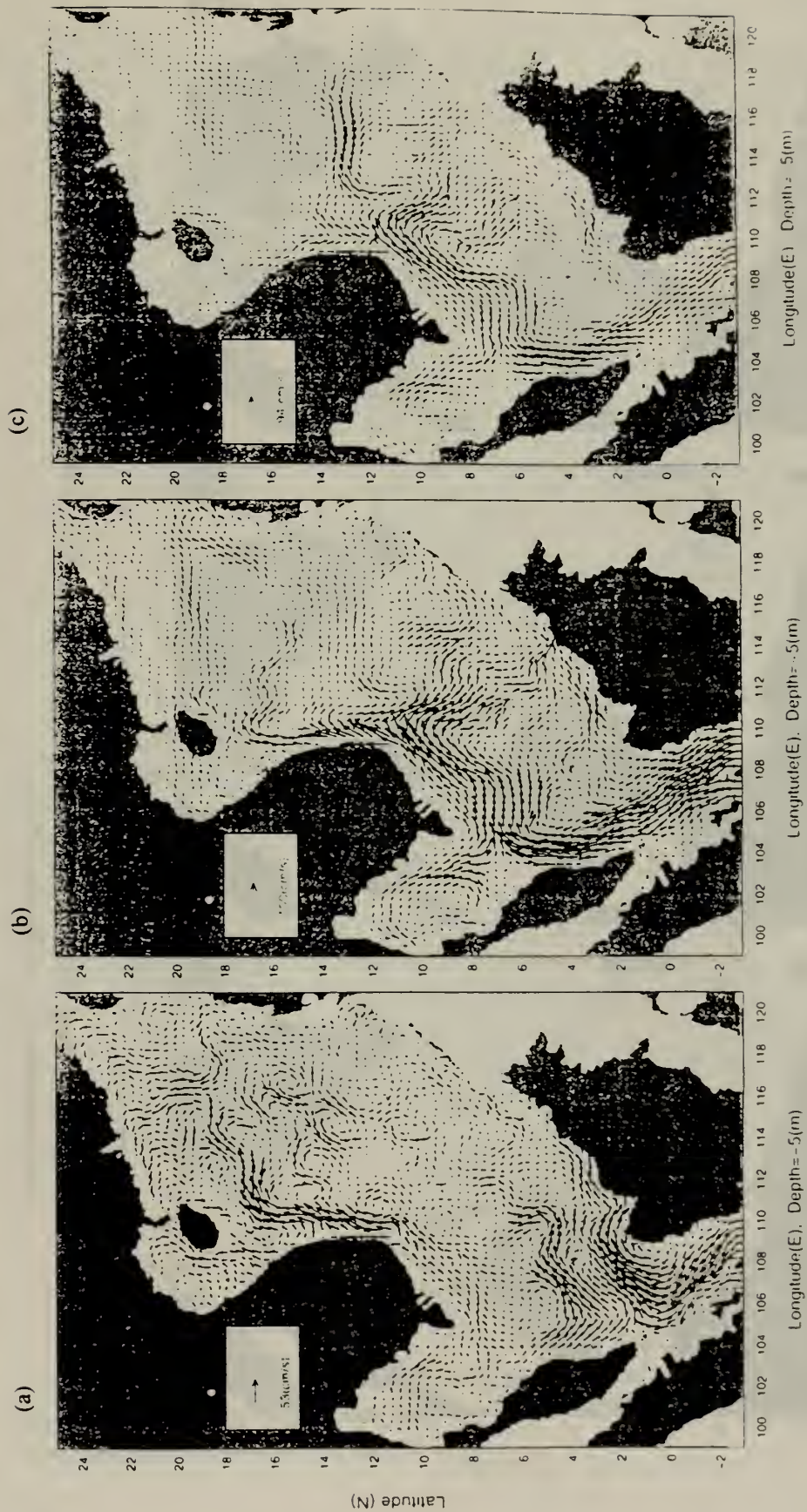


Figure 20. Near surface circulation for linear run during summer (a) May 15, (b) July 15, (c) September 15.

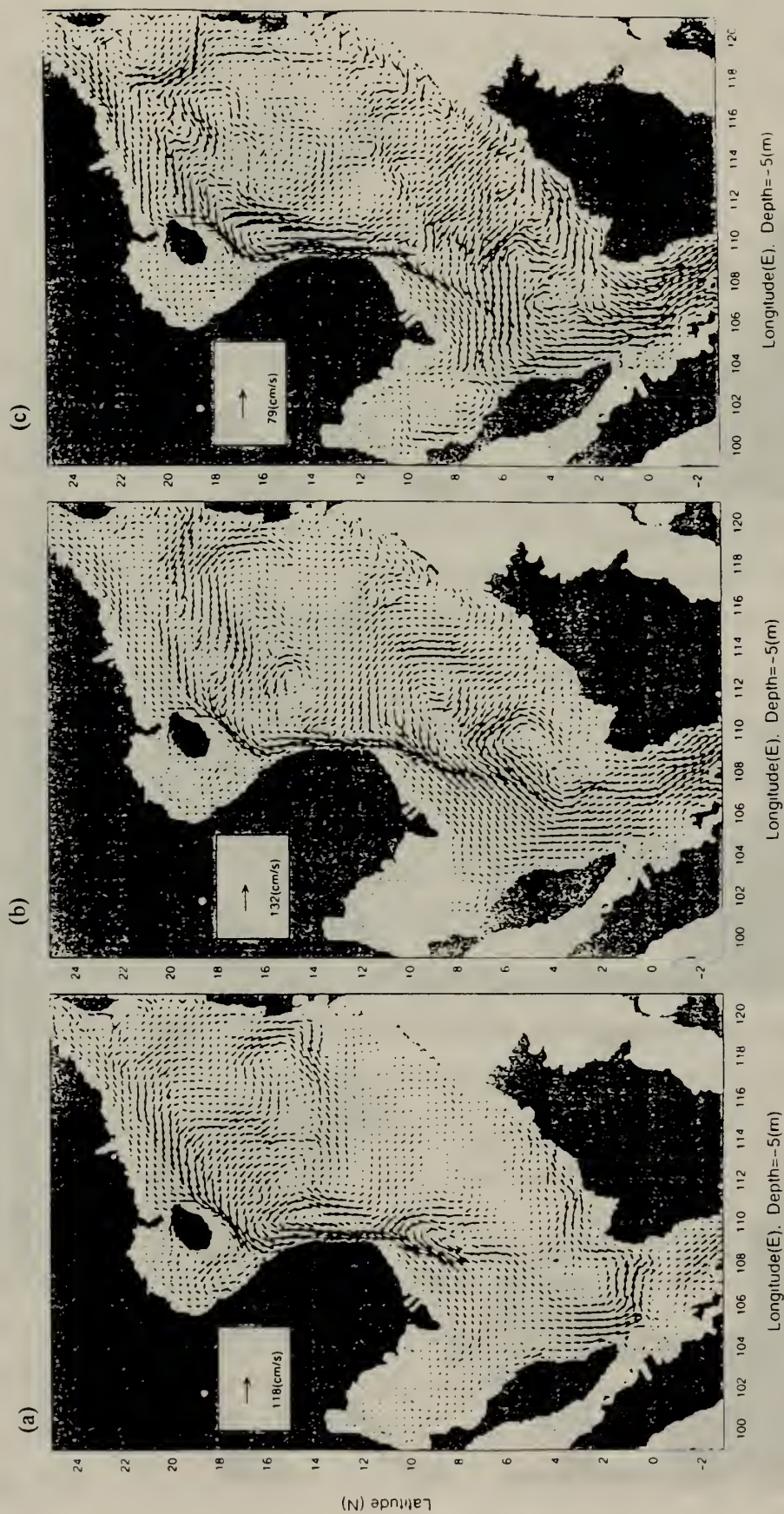


Figure 21. Near surface circulation for linear run during winter (a) October 15, (b) December 15, (c) March 15.

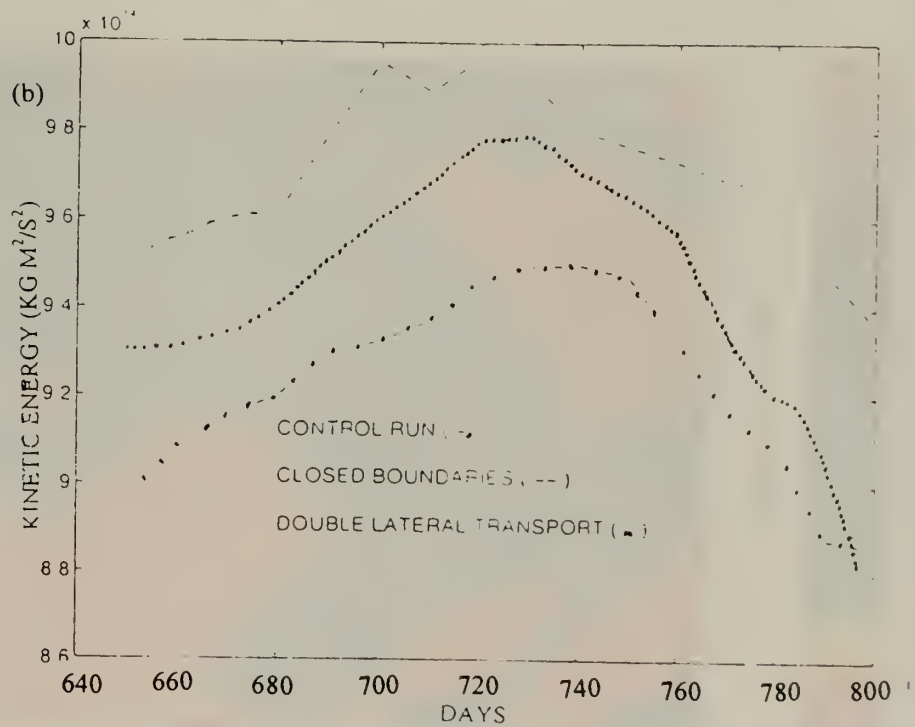
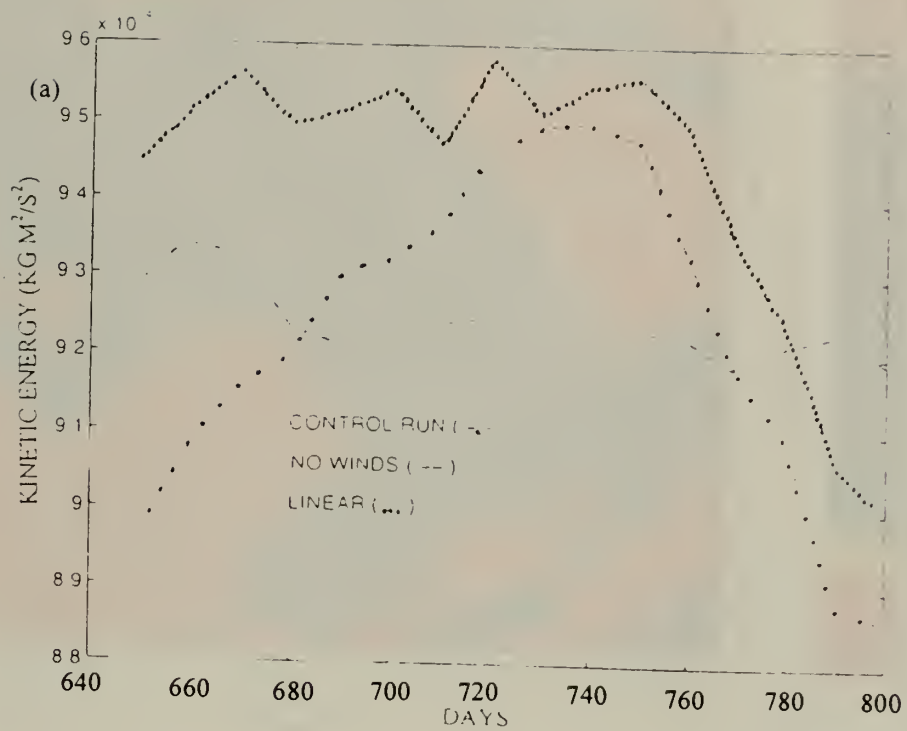
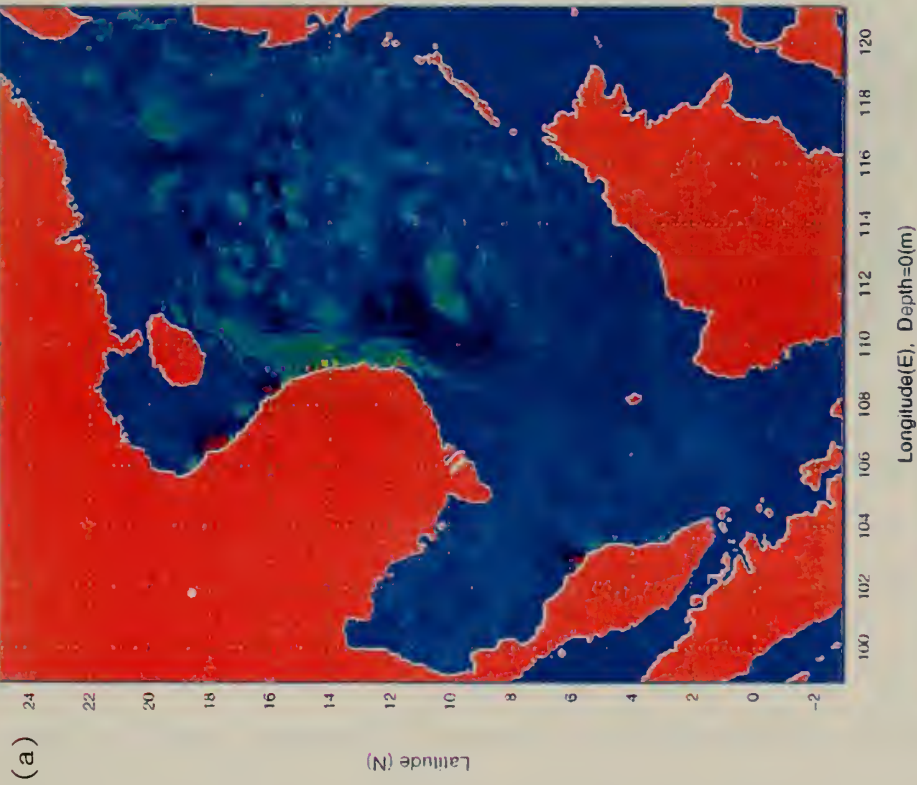


Figure 22. A comparison of kinetic energy ($\text{kg m}^2/\text{s}^2$) during the winter monsoon for (a) control run, no winds run, and linear run and (b) control run, closed boundaries run, and double lateral transport run.

SUMMER MONSOON Temperature difference ($^{\circ}\text{C}$) due to non-linearity



WINTER MONSOON Temperature difference ($^{\circ}\text{C}$) due to non-linearity

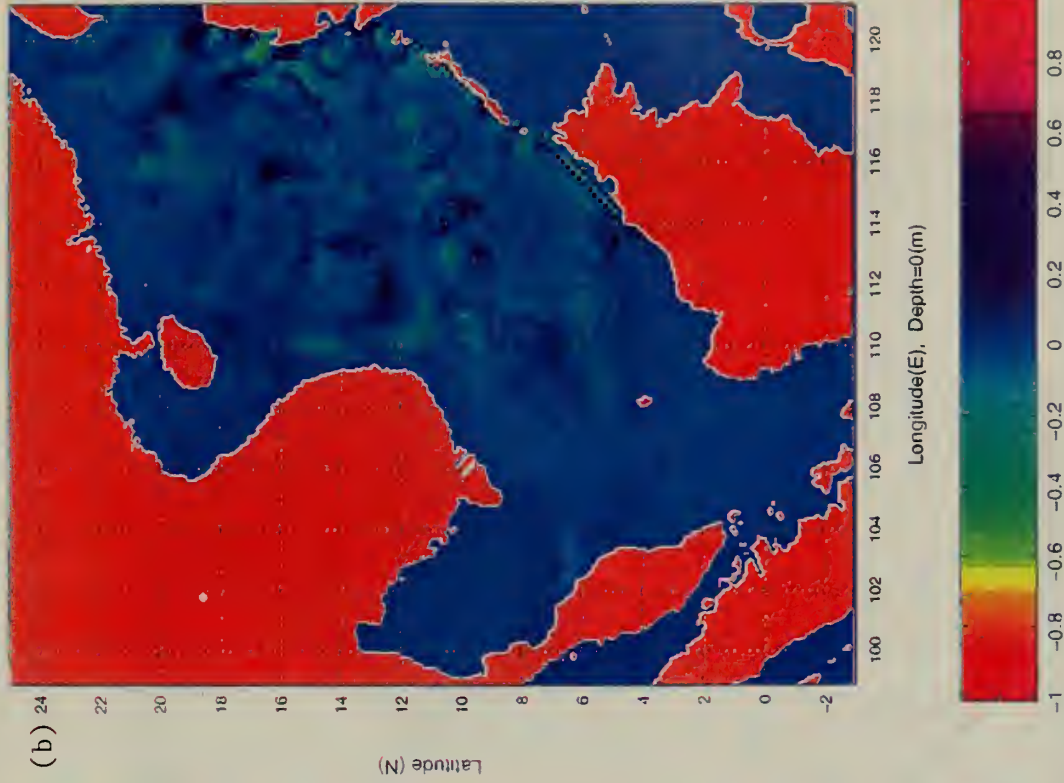


Figure 2A. Sea surface temperature differences ($^{\circ}\text{C}$) between control run and linear run over (a) summer monsoon, (b) winter monsoon.

SUMMER MONSOON Volume Transport (Sv) due to non-linearity

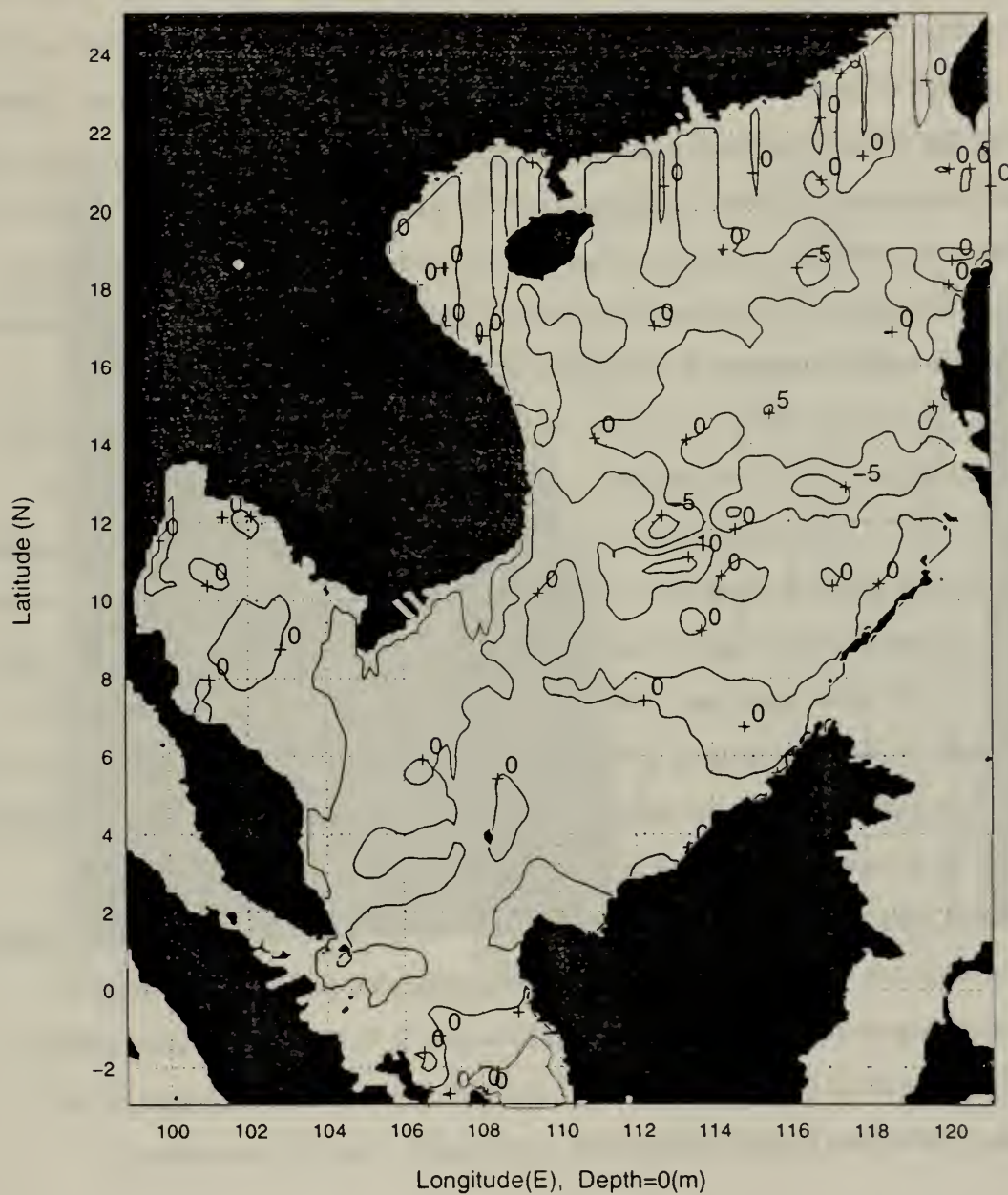


Figure 24. Volume transport difference (Sv) between control run and linear run averaged over summer monsoon.

advective processes have a dampening effect on these features. Other than these specific features the difference in volume transport is considerably smaller than the differences due to other forcing mechanisms. In other words the system is quasi-linear, as an initial calculation of the Rossby number for the latitude range indicated. A cross section plot of the average difference in velocity at 6° N between this run and the control run (Figure 25) shows that when advection is removed, the Malaysia coastal jet current decreases velocity somewhat and moves closer to shore. At 13° N, a similar phenomenon occurs--the VCJ is closer to shore and focused into a narrower jet at the surface while flow along the bottom boundary (shelf current) is increased (Figure 26). At both latitudes the amount of northward volume transport is unchanged (Table 3).

The winter VCJ also experiences narrowing and focusing when advection is removed (Figure 27). From the surface to 500 m there is an increase in southward velocity of 15-25 cm/s in the core at 13° N and a decrease of similar magnitude on either side. The net increase of velocity of 10 cm/s results in an increase in southward volume transport contribution of approximately 3.1 Sv from non-linear advection in the winter (Table 3). The most significant difference during the winter, however, occurs in the mesoscale cyclonic topographic gyre that forms northeast of Natuna Island in the control run. Figure 28 shows that the feature has a strong dependence on advection, losing about 8-10 Sv of transport when driven linearly, again consistent with theory regarding baroclinic instabilities. Figure 29 shows the effect vertically; it is apparent from this plot that advection is important to the velocity of the eddy, the differences in velocity corresponding to a volume transport contribution of 3 Sv through this cross section. Similarly, for small scale eddies there are positive differences in the region of the cyclonic eddies and negative differences in the region of anticyclonic eddies.

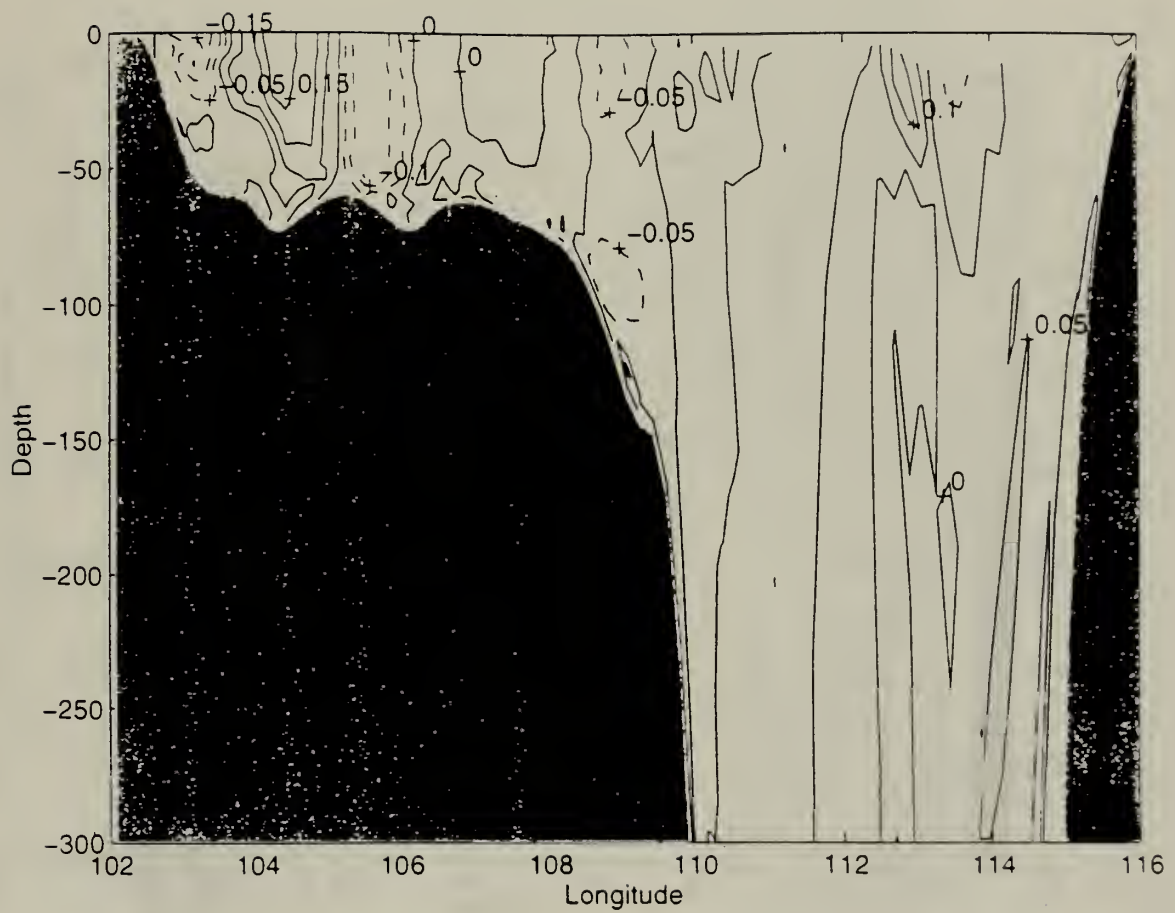


Figure 25. V component of velocity difference (m/s) between control run and linear run at 6° N latitudinal cross section averaged over summer monsoon.

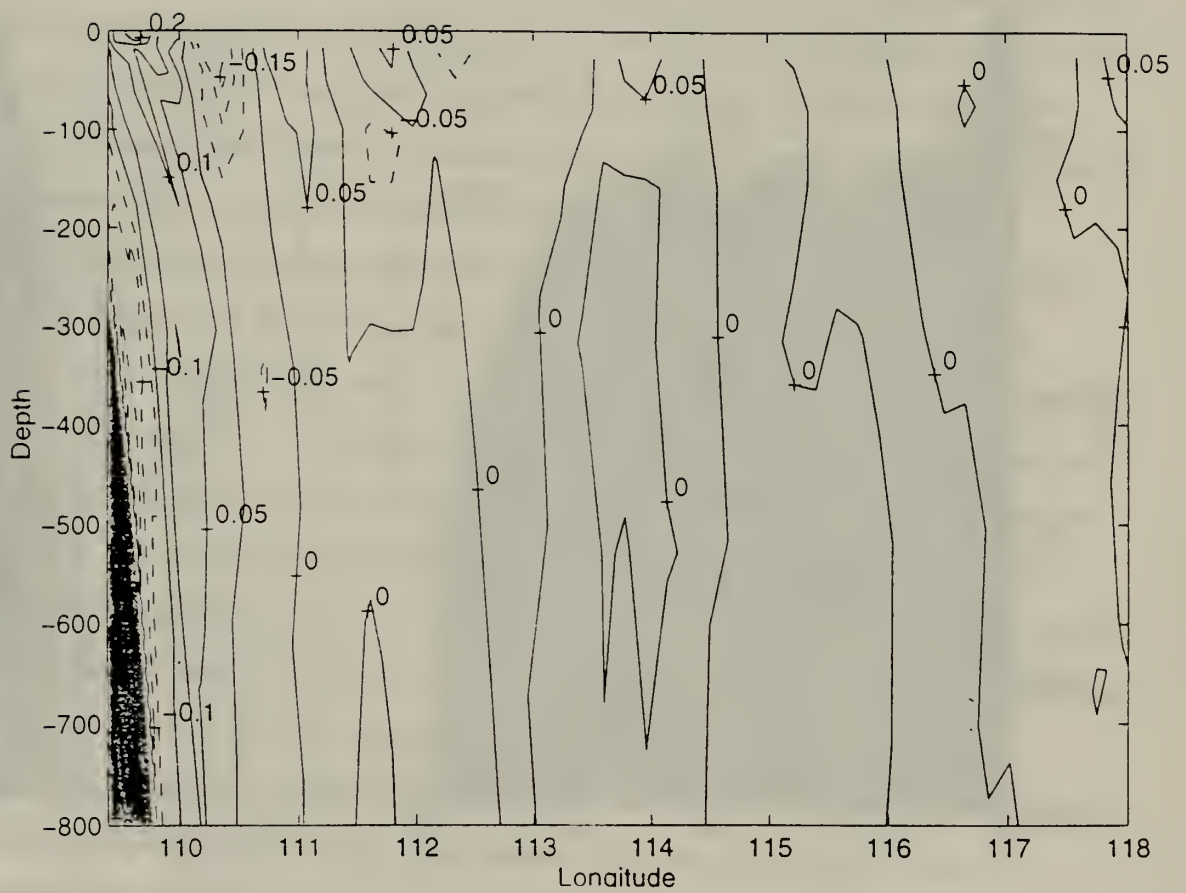


Figure 26. V component of velocity difference (m/s) between control run and linear run at 13° N latitudinal cross section averaged over summer monsoon.

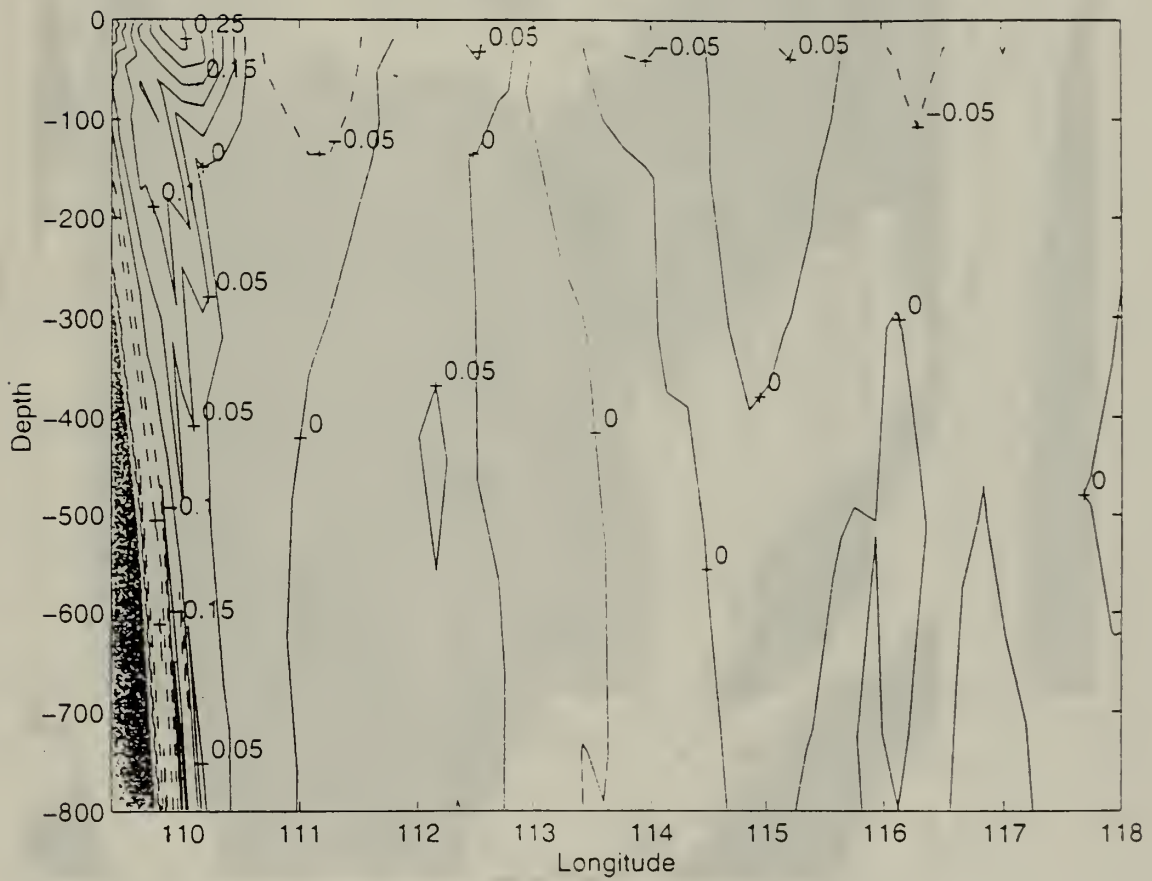


Figure 27. V component of velocity difference (m/s) between control run and linear run at 13° N latitudinal cross section averaged over winter monsoon.

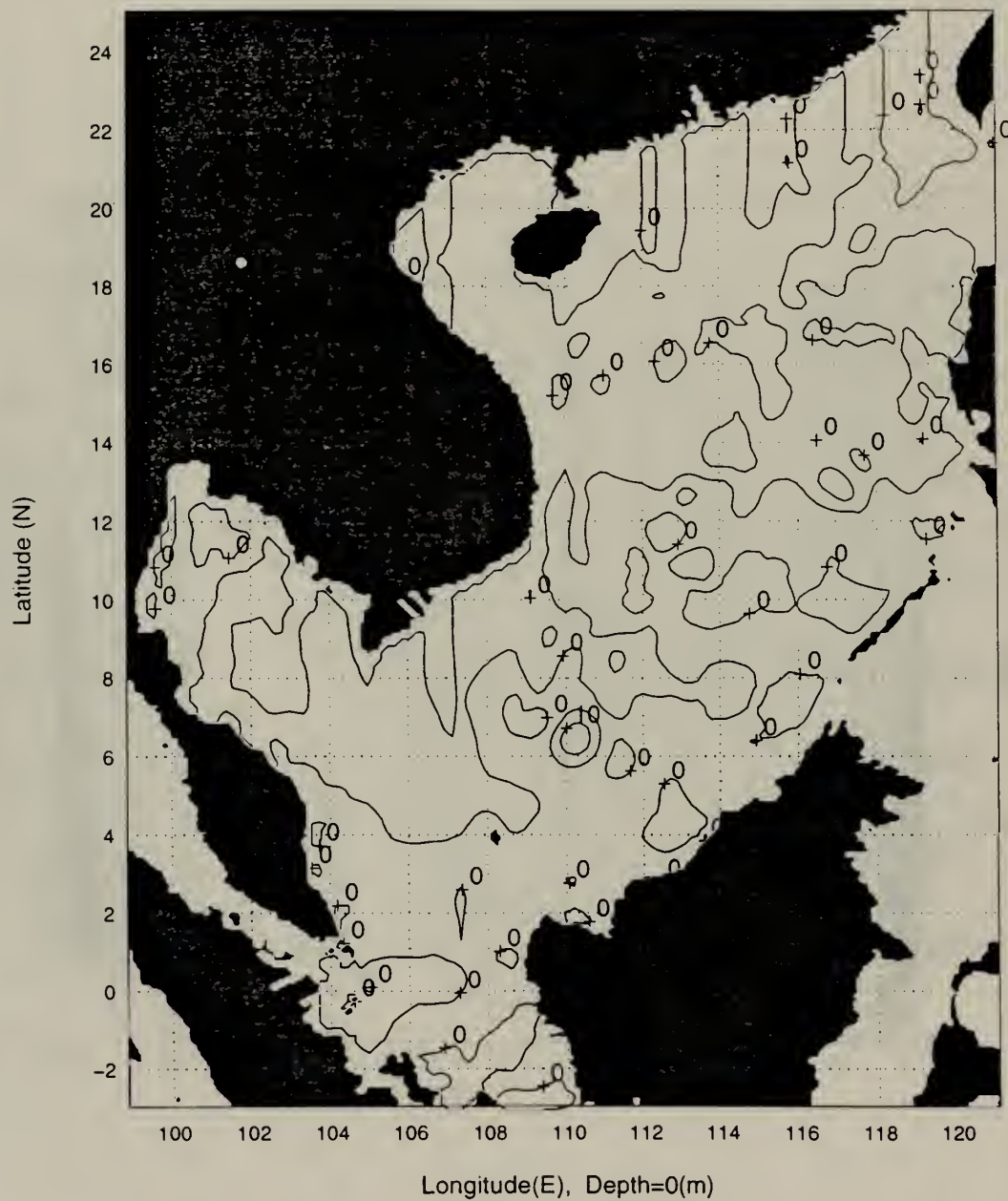


Figure 28. Volume transport difference (Sv) between control run and linear run averaged over winter monsoon.

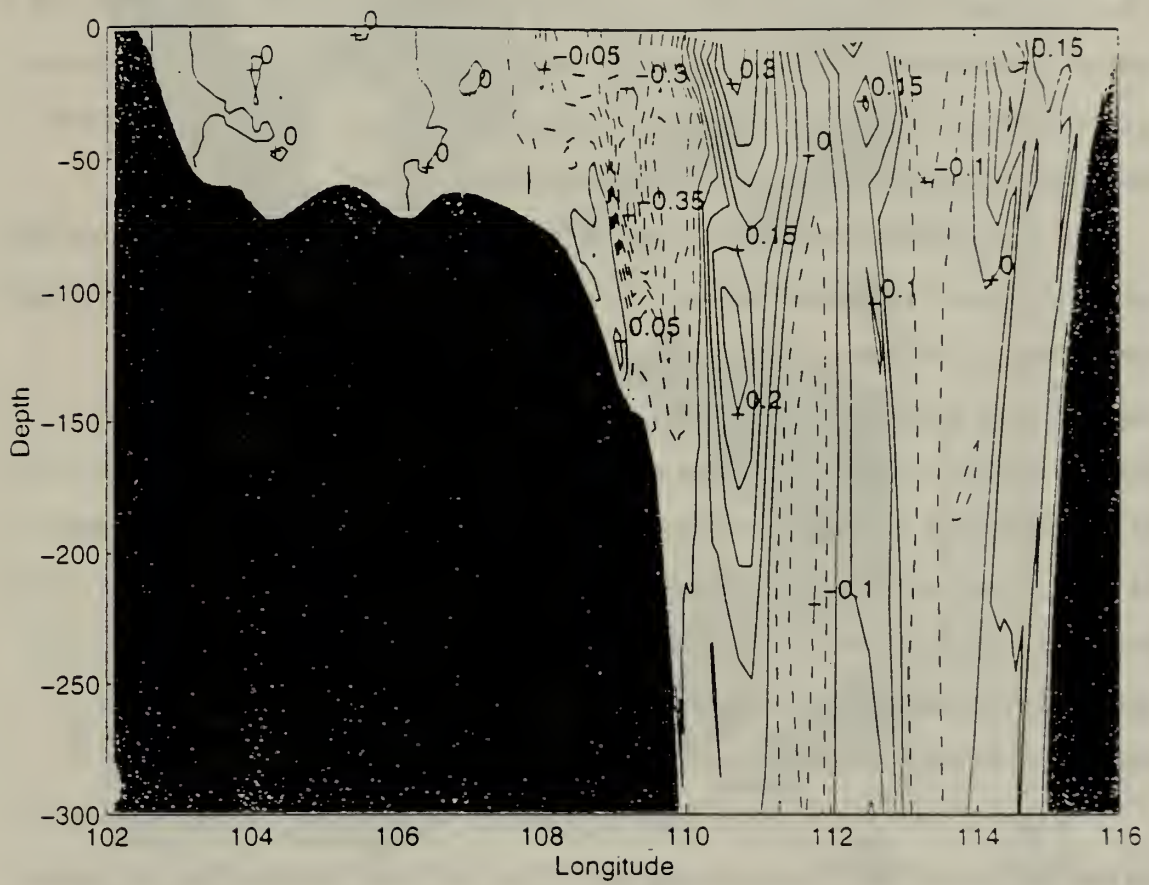


Figure 29. V component of velocity difference (m/s) between control run and linear run at 6° N latitudinal cross section averaged over winter monsoon.

2. Effects of wind (Run 3)

When winds are removed from the forcing, the model results show considerable changes in the structure of the summer circulation and a virtual disappearance of features in the winter circulation. The general circulation is still anticyclonic in the summer and cyclonic in the winter but surface velocities tend to be 20-30 cm/s smaller in the surface layers (Figures 30-31). The difference between Run 1 and Run 2 shows the monsoon wind effects on the SCS circulations and thermohaline structure.

A comparison of the kinetic energy of the no wind SCS to the control run reveals that the increase of wind contributes energy as the monsoon peaks and then acts to reduce energy through dissipation effects as the monsoon weakens (Figure 22a). The contribution of winds to the average sea surface height is seen in Figure 32: in the summer, winds act to push the surface elevation to the north increasing the elevation 5-10 cm. Elsewhere the summer wind is responsible for a decrease of the same magnitude. In the winter, the wind increases the surface elevation over the continental shelves by 15-18 cm, with a large wind induced depression over the deep basin. Since dynamic topography is a measure of potential energy, these regions show an estimate of the contribution of wind forcing to available potential energy.

Figure 33 is a plot of the differences in surface temperatures between the control run and the no wind run. During the summer, when winds are blowing from the equator, the SST off the coast of central and northern Vietnam is 1-2 degrees cooler than when winds are absent. Similar results are evident off the eastern coast of Hainan. During the winter the negative surface temperature difference is greatest on the east side of the basin along the Palawan Trough, with similar results in surface salinity differences (Figure 34).

Current patterns change substantially over the Sunda Shelf during the no wind summer. A mesoscale anticyclonic eddy is generated south of Natuna Island with a core velocity of 60-80 cm/s (Figure 35) and propagates to the northwest as the summer progresses (Figure 30). Examination of the cross section difference in velocity at 6° N

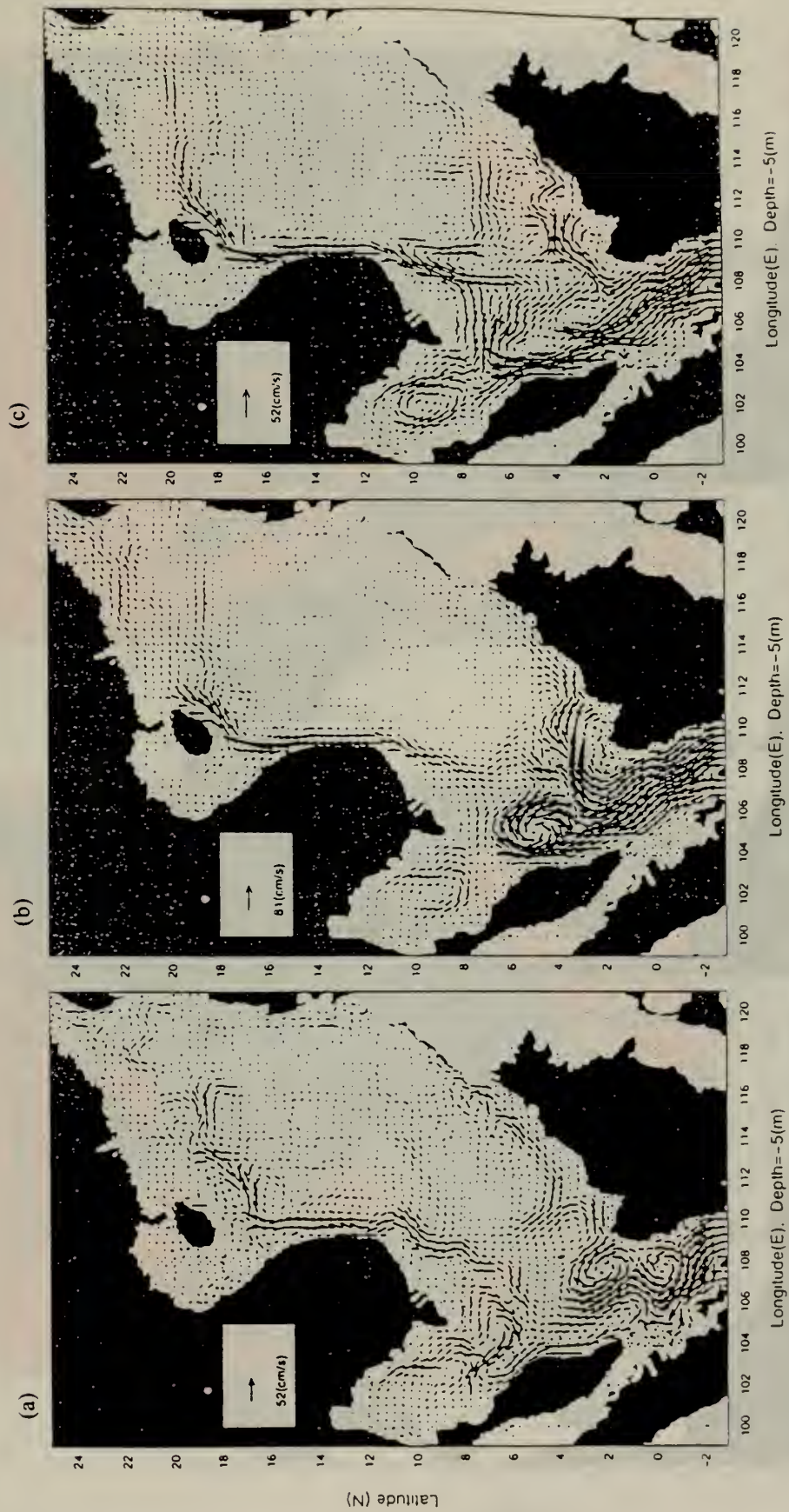


Figure 30. Near surface circulation for no winds run during summer (a) May 15, (b) July 15, (c) September 15.

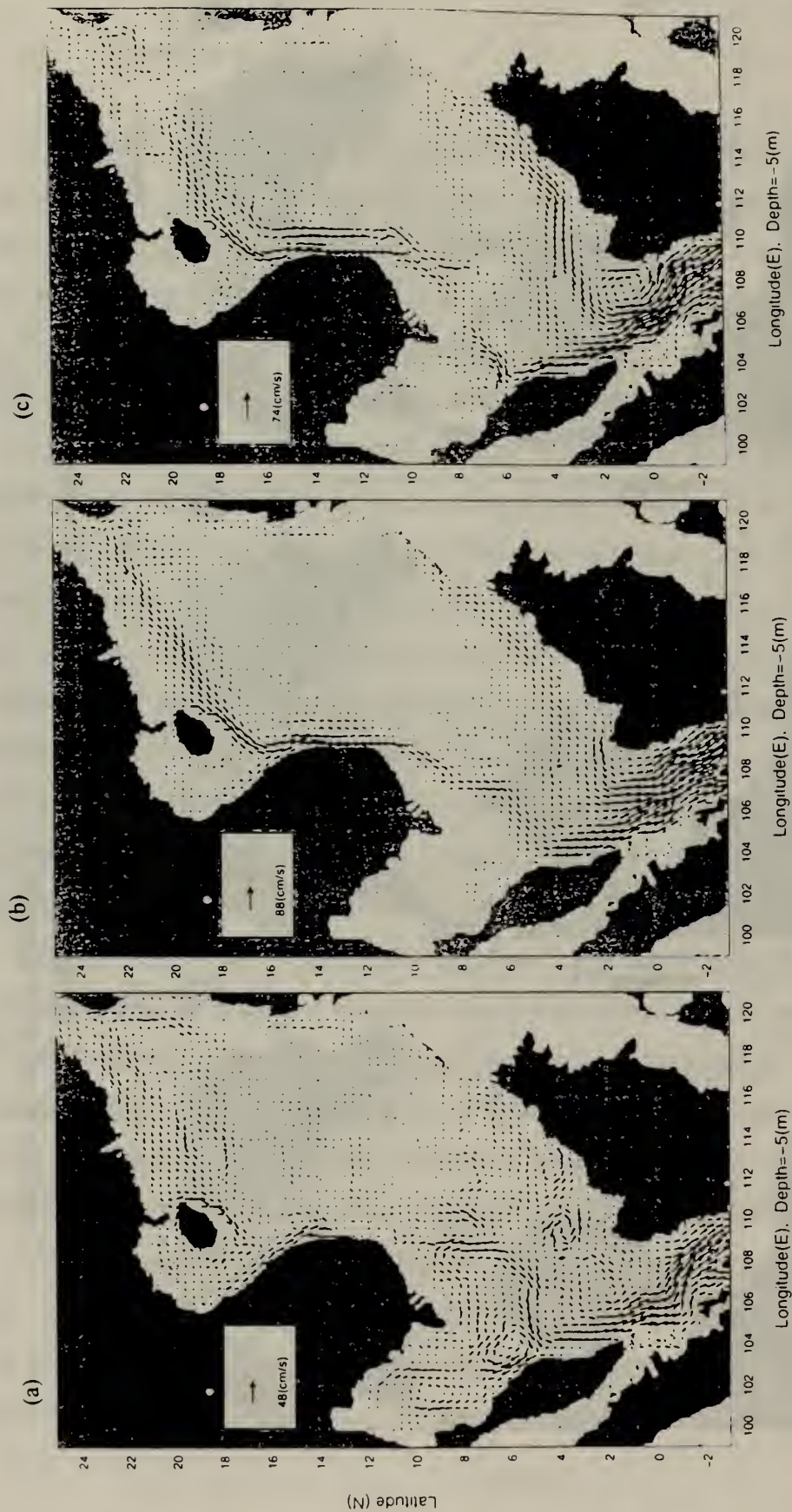


Figure 31. Near surface circulation for no winds run during winter (a) October 15, (b) December 15, (c) March 15.

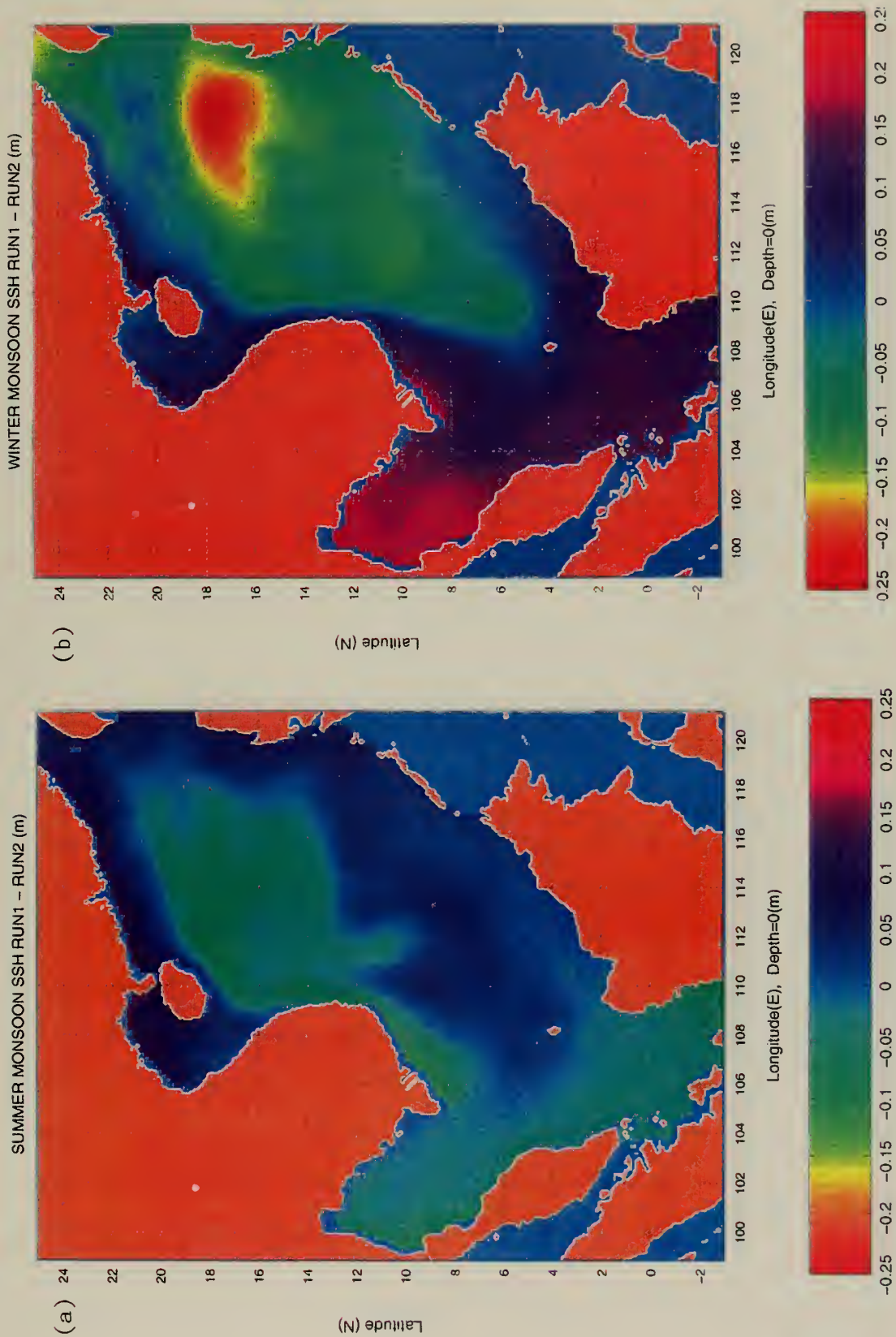


Figure 32. Sea surface height difference (m) between control run and no winds run averaged over (a) summer monsoon, (b) winter monsoon.

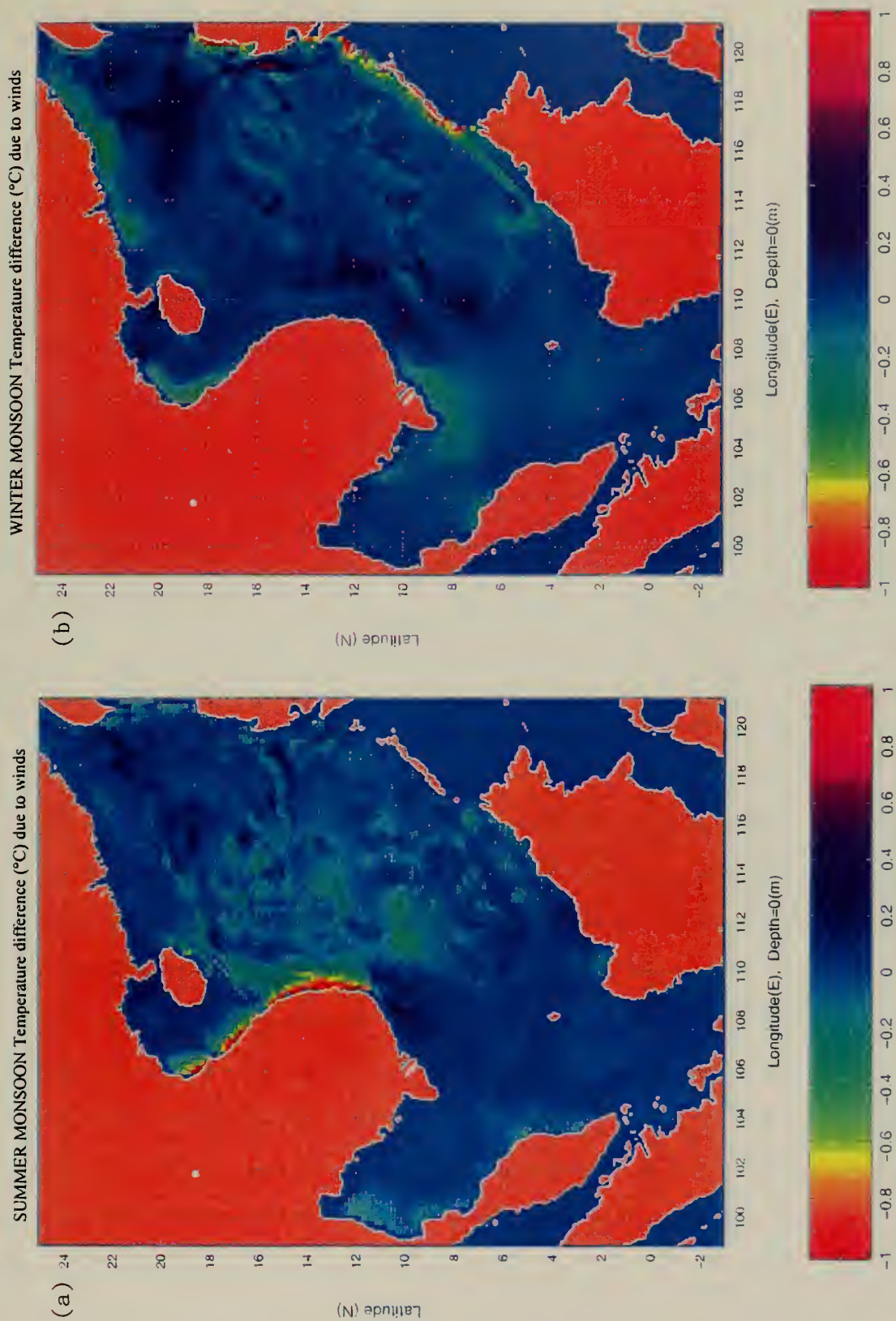


Figure 33. Sea surface temperature difference (°C) between control run and no winds run averaged over (a) summer monsoon, (b) winter monsoon.

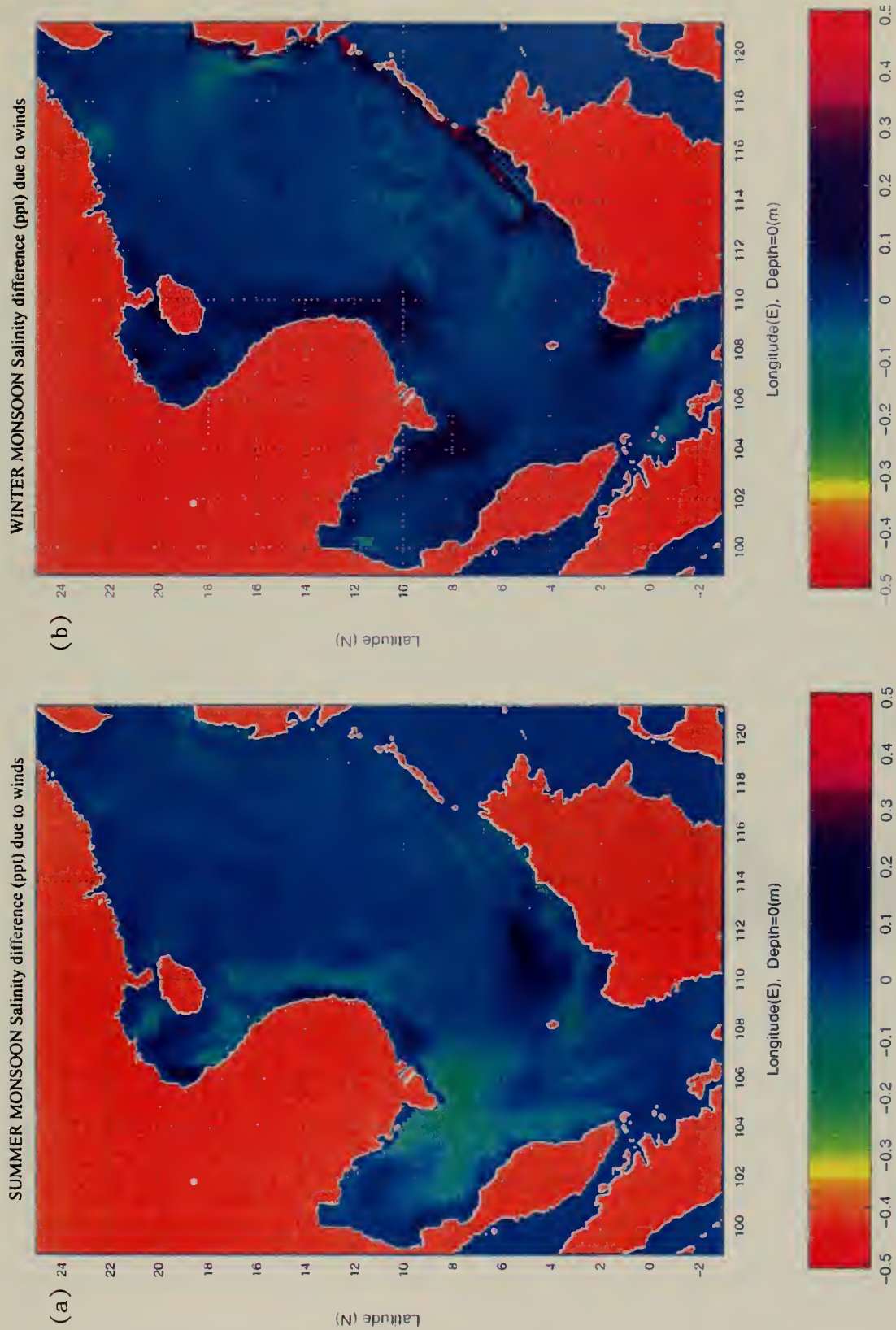


Figure 34. Sea surface salinity difference (ppt) between control run and no winds run averaged over (a) summer monsoon, (b) winter monsoon.

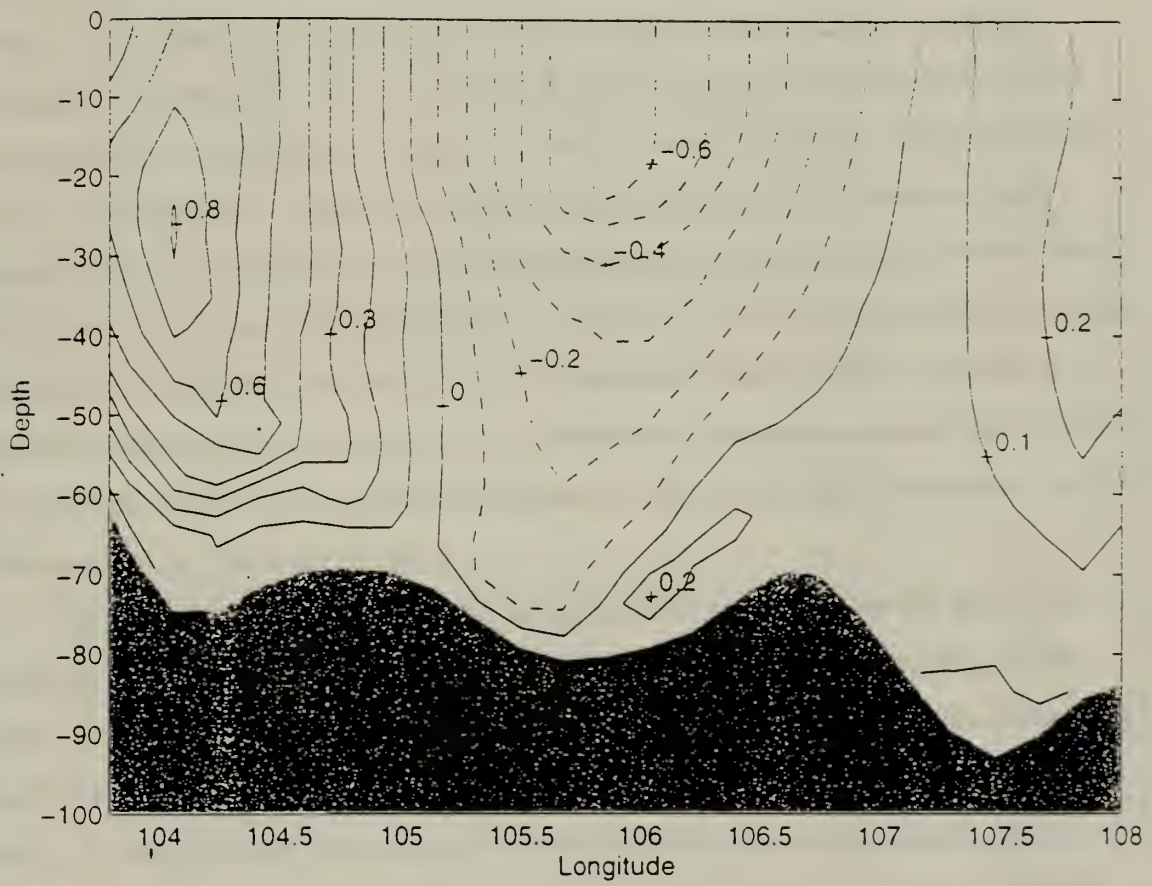


Figure 35. V component of velocity (m/s) for no winds run 15 July at 5° N latitudinal cross section.

shows that the average intensification of current offshore of Malaysia is reduced by 10-15 cm/s and has migrated closer to shore (Figure 36a). The summer VCJ still peaks in velocity by the middle of the monsoon but the core velocity is slightly higher. Since the current has moved inside the 100 m isobath (Figure 36b), and the core is smaller, the change in southward volume transport is approximately zero (Table 3). Also, rather than migrate south from the shore of Hainan as it does in the control run (increasing in strength as the summer progresses), the northern filament current actually migrates farther north following the 100 m isobath of the Asian continental shelf (Figure 30b-c). This translates into an increase in volume transport along the shelf break and a decrease in cross basin transport. Notice the difference in total volume transport due to wind forcing (Figure 37a), integrated over the summer monsoon season: positive values along the 100 m isobath south of Hainan indicate an increase of 6-8 Sv transport when the wind is removed. The negative values along 13° N indicate a decrease of 4-6 Sv transport at these grid locations in a no wind scenario. Additionally, the southwestward meander of the coastal jet near 10° N is considerably reduced in this run, losing an average of 5-6 Sv of transport when winds are removed.

The most significant differences during the winter monsoon are the absence of flow away from the western Borneo coast, the absence of topographic steering of the winter VCJ and the subsequent absence of the NIG at the southern edge of the deep basin (Figure 31). Inspection of the difference in velocity at 6° N, shows that the gyre loses an average 30-40 cm/s of its swirl velocity in this run (Figure 38a), corresponding to a volume transport reduction of 4.2 Sv. The winter VCJ is greatly reduced when winds are removed, losing 30-40 cm/s velocity (Figure 38b), corresponding to a southward volume transport loss of 4.6 Sv. The increase in shelf current flow is shown in the volume transport difference plot (Figure 37b), the only locations where total volume transport increases when winter winds are removed are along the Asian continental shelf break and at 13° N. Conversely, the volume transport difference in the rest of the central basin shows that there is considerably less volume transport when winds are removed. In general, the winter near surface circulation shows almost no horizontal structure in the

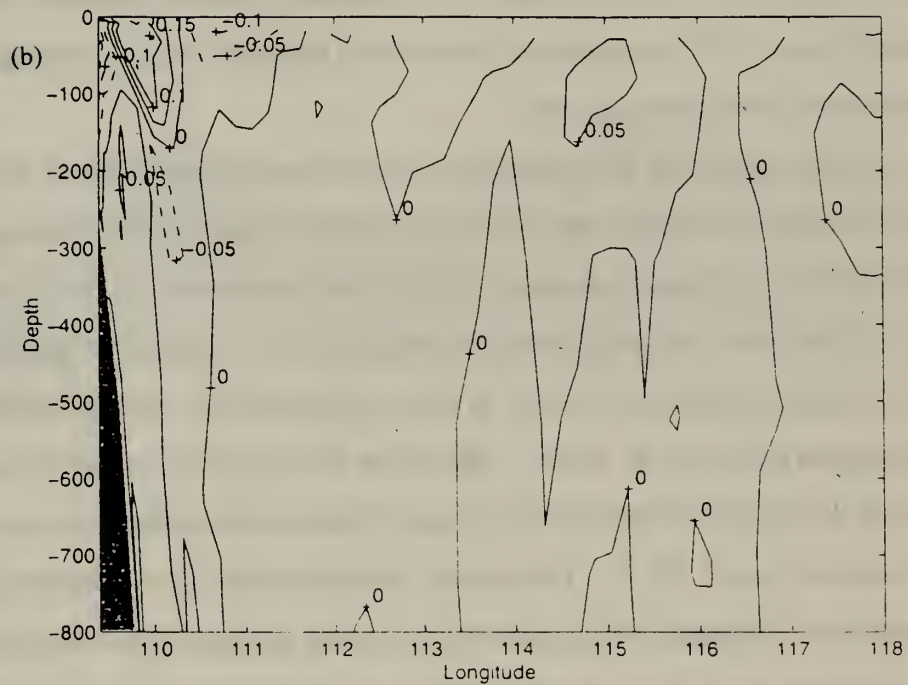
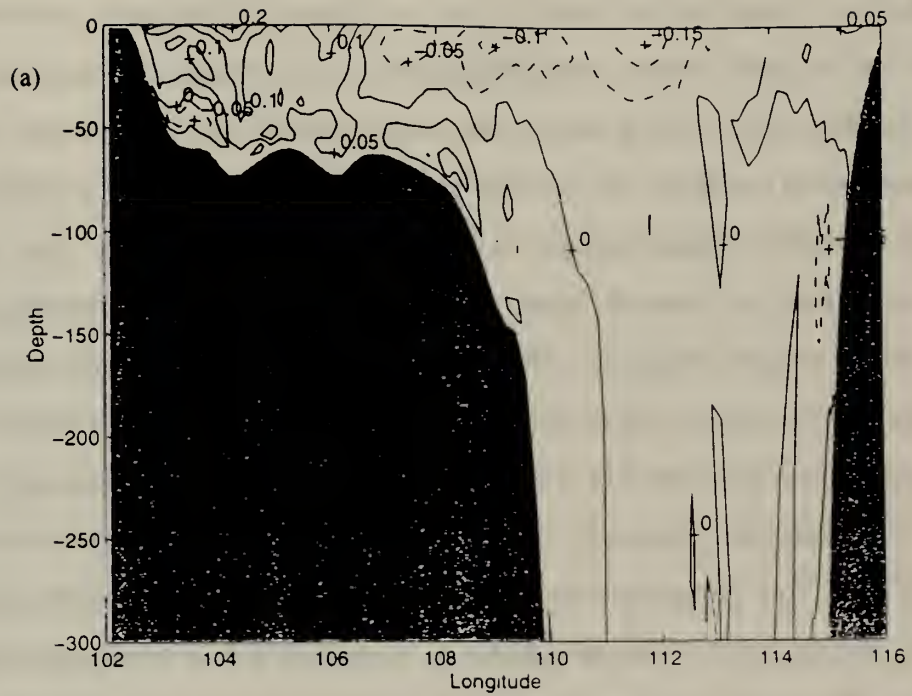
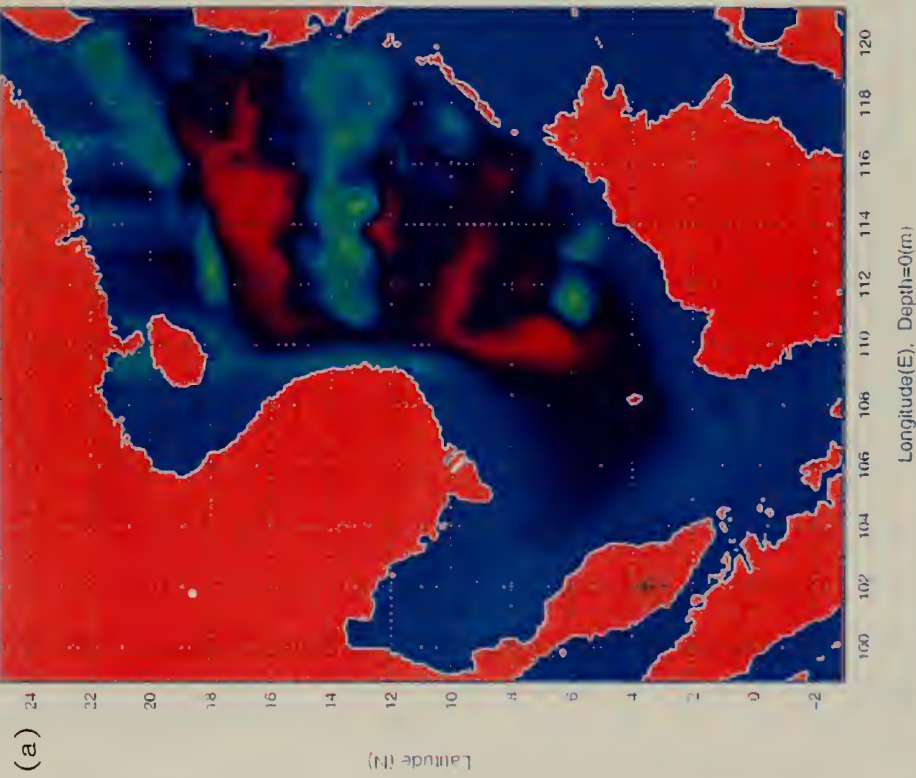


Figure 36. V component of velocity difference (m/s) between control run and no winds run averaged over summer monsoon at (a) 6° N latitudinal cross section, (b) 13° N latitudinal cross section.

SUMMER MONSOON Volume Transport difference (Sv) due to winds



WINTER MONSOON Volume Transport difference (Sv) due to winds

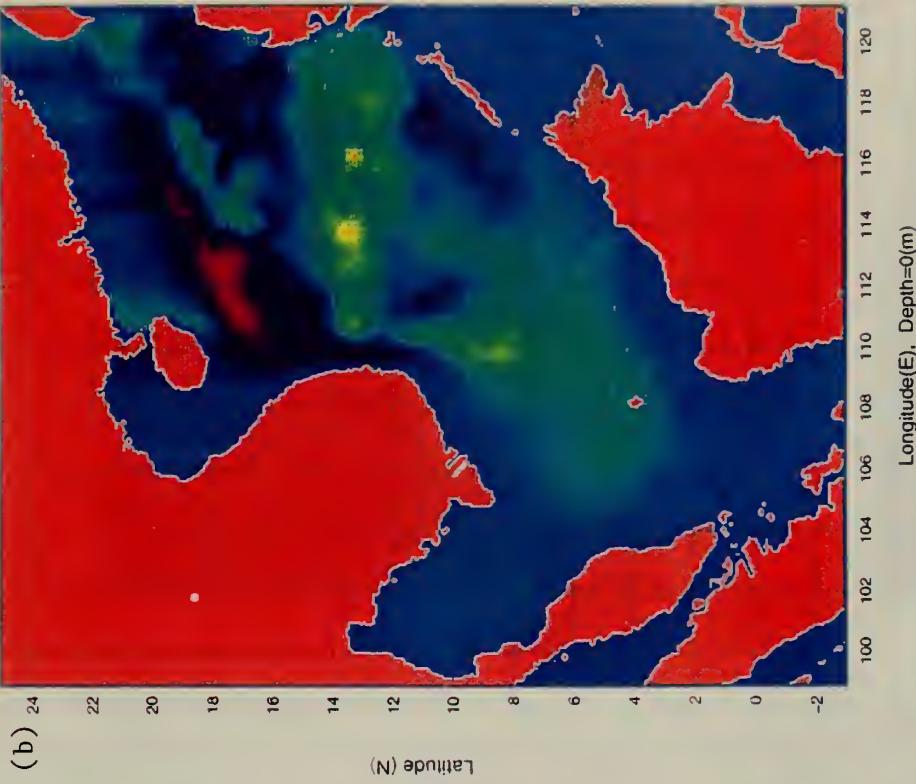


Figure 37. Volume transport difference (Sv) between control run and no winds run averaged over (a) summer monsoon, (b) winter monsoon.

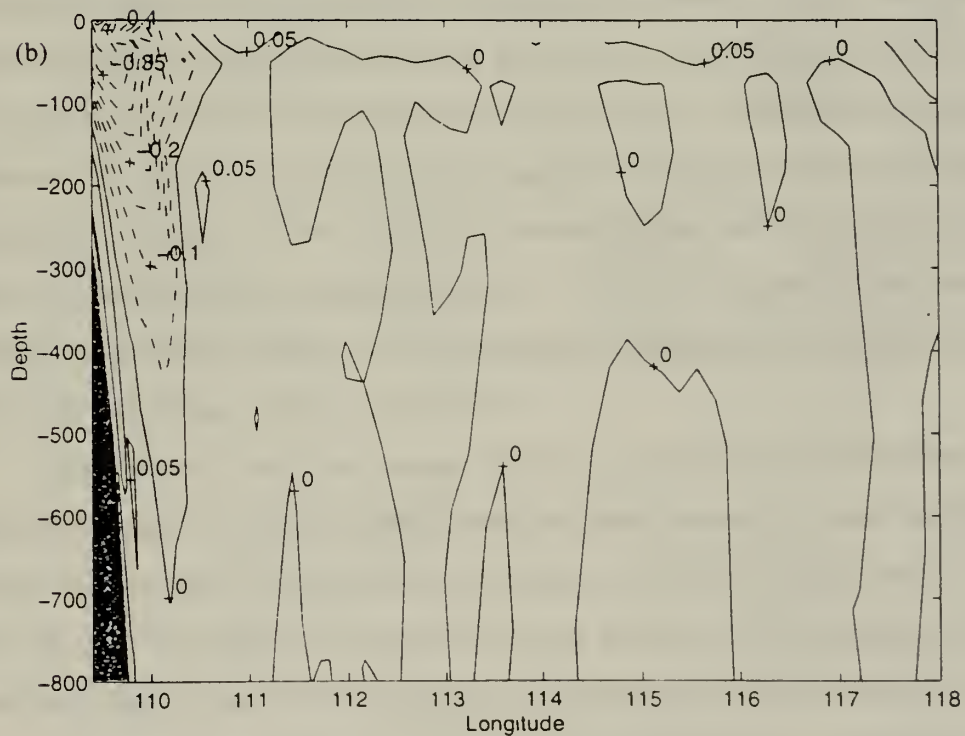
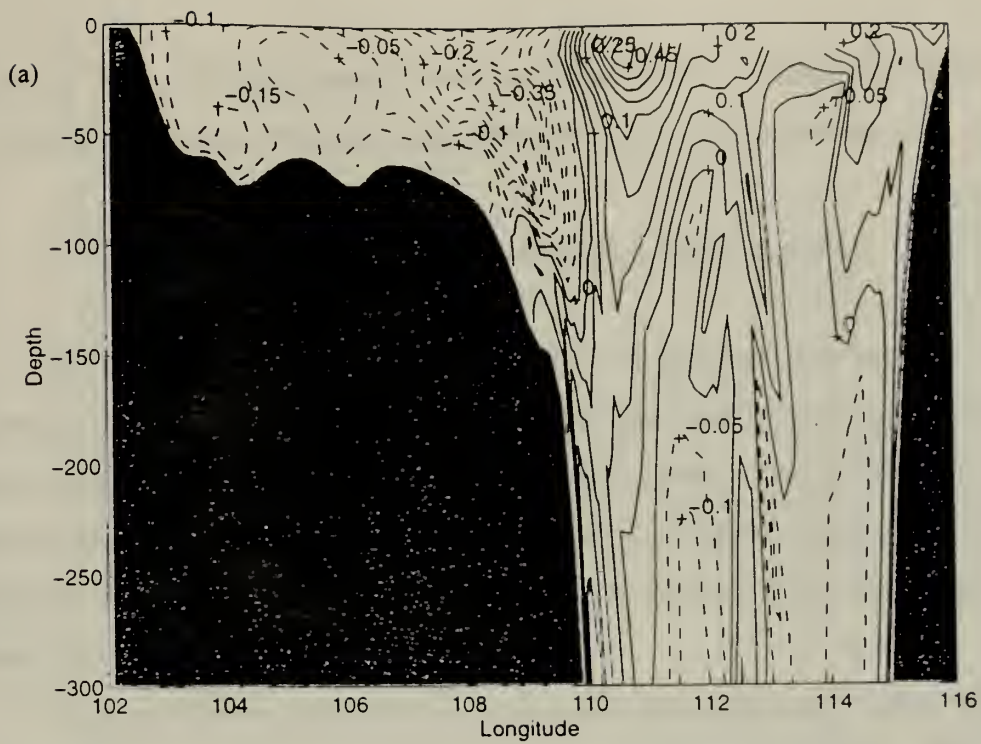


Figure 38. V component of velocity difference (m/s) between control run and no winds run averaged over winter monsoon at (a) 6° N latitudinal cross section, (b) 13° N latitudinal cross section.

absence of wind. The large range of area that shows 5-10 Sv of transport loss indicates that wind is an important factor in determining the winter volume transport.

3. Effects of lateral boundary transport (Runs 4 and 5)

The third sensitivity study used the control run equations and forcing but closed all open lateral boundaries, preventing transport of mass, heat or salinity through the Luzon Strait, Formosa Strait or Gasper and Karimata Straits. The resulting circulation is shown in Figures 39-40. The final sensitivity study doubled the inflow and outflow through these boundaries. The general circulation in this case is, of course, considerably altered (Figures 41-42).

With no inflow or outflow the summer anticyclonic gyre and winter cyclonic gyre are more pronounced. Increased recirculation generally leads to greater horizontal and vertical variability of the current structure; the result of this increased variability is that the winter kinetic energy is largest for this run (Figure 22b). The sea surface height differences are shown in Figure 43: in the summer, removing boundary transport causes an increased elevation near the northern and western shores and a decreased elevation in parts of the basin and at the southern boundary. The reverse happens in the winter, in both seasons the greatest effect is over the shallower Gasper and Karimata Straits in the south--both experience differences of 25 cm.

Figure 44 is a plot of the average difference in summer surface temperatures, winter differences were insignificant beyond the open boundaries. In the summer, two features are prominent. First, the surface temperatures in the vicinity of the southwestward boundary current that diverts flow from the VCJ are considerably warmer in this case. Second, and more significant, is the temperature difference off the coast of northern Vietnam. Current flow in the control run in this region is northward--a situation beneficial to upwelling--but in the closed boundaries run current flow is southward and upwelling does not occur.

The summer circulation patterns change dramatically when the lateral transport is removed. There is still western intensification of current along the coast of Malaysia, and

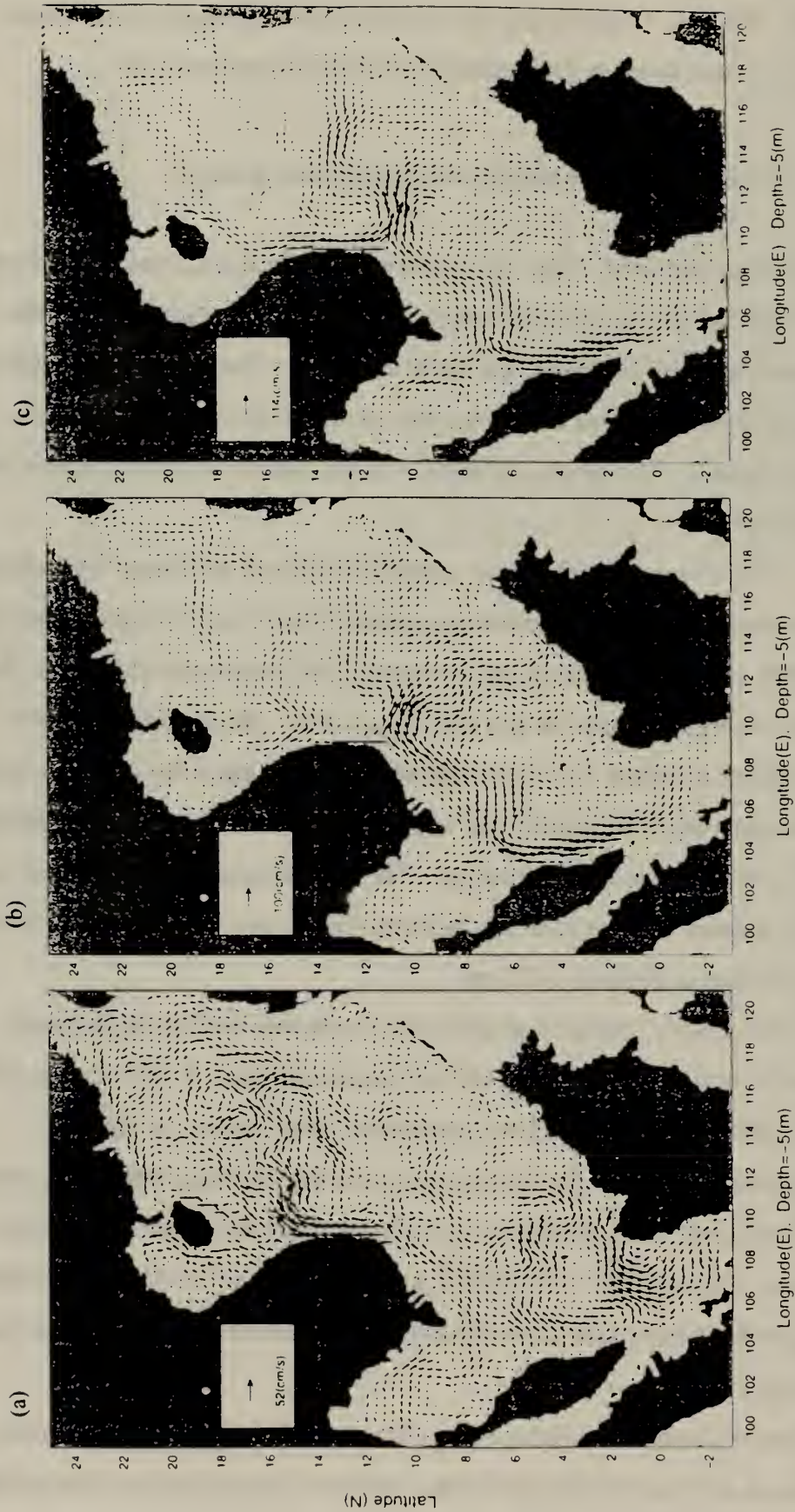
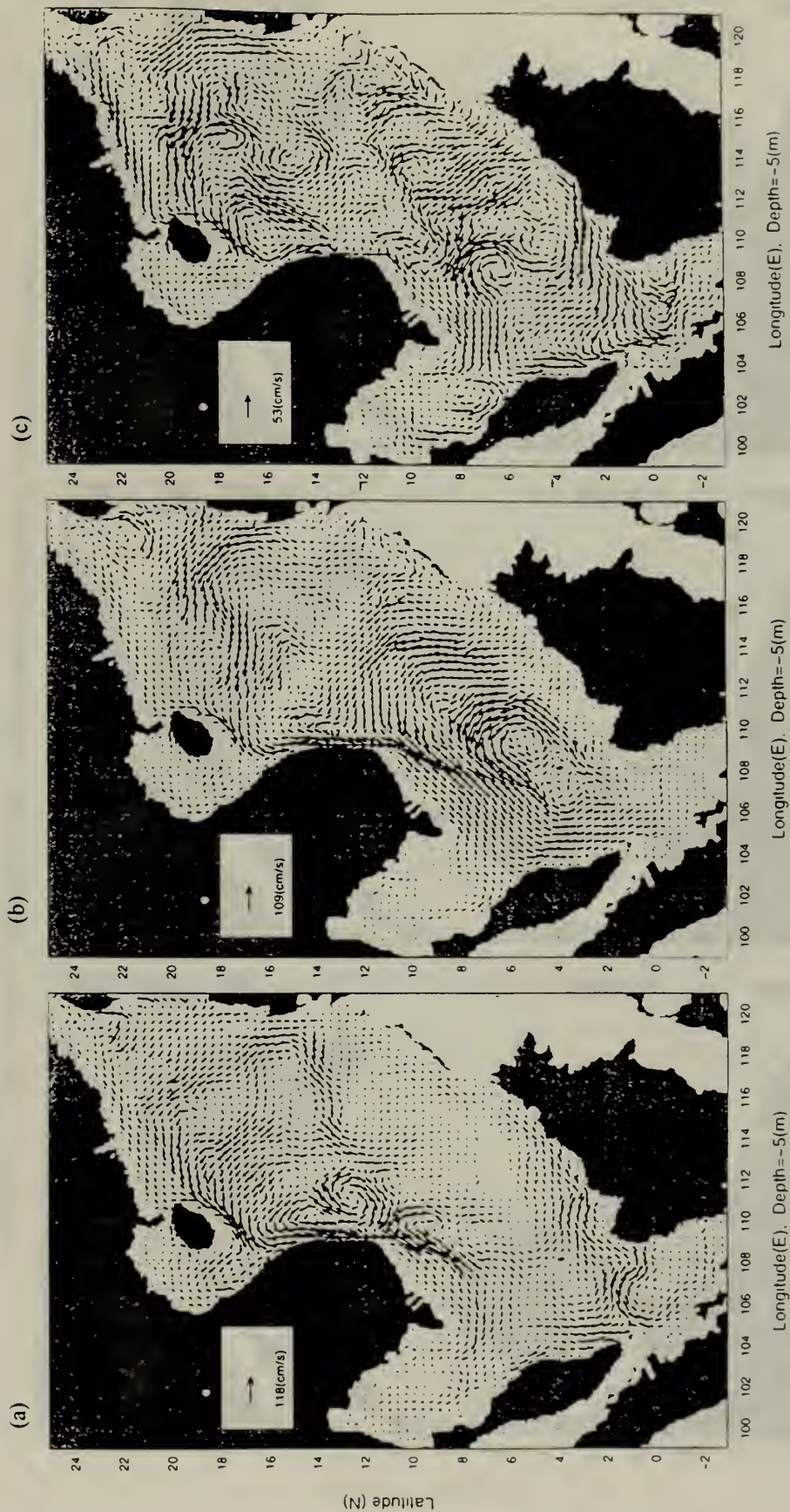


Figure 39. Near surface circulation for closed boundaries run during summer (a) May 15, (b) July 15, (c) September 15.



**Figure 40. Near surface circulation for closed boundaries run during winter
(a) October 15, (b) December 15, (c) March 15.**

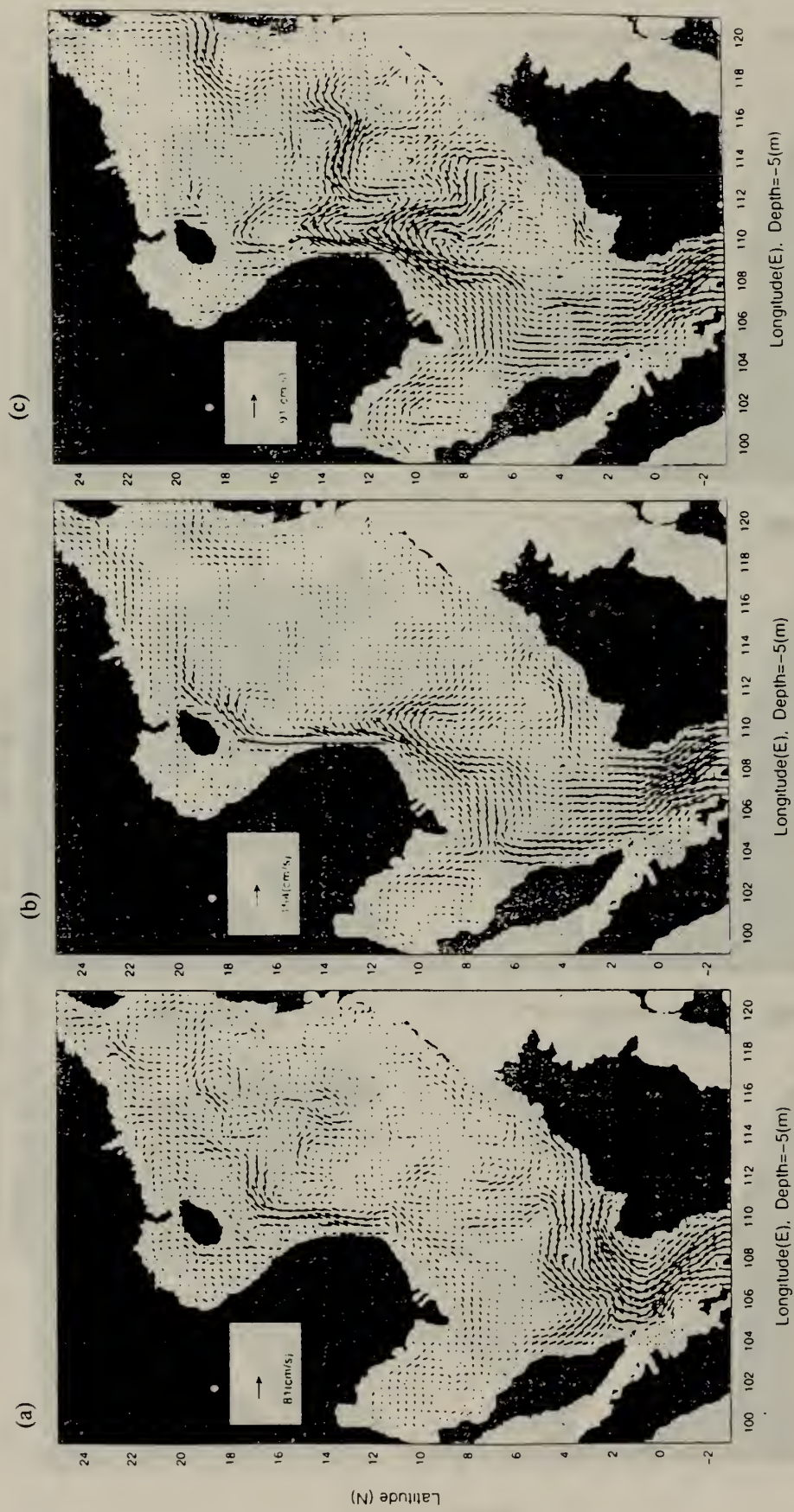


Figure 41. Near surface circulation for double lateral transport run during summer
(a) May 15, (b) July 15, (c) September 15.

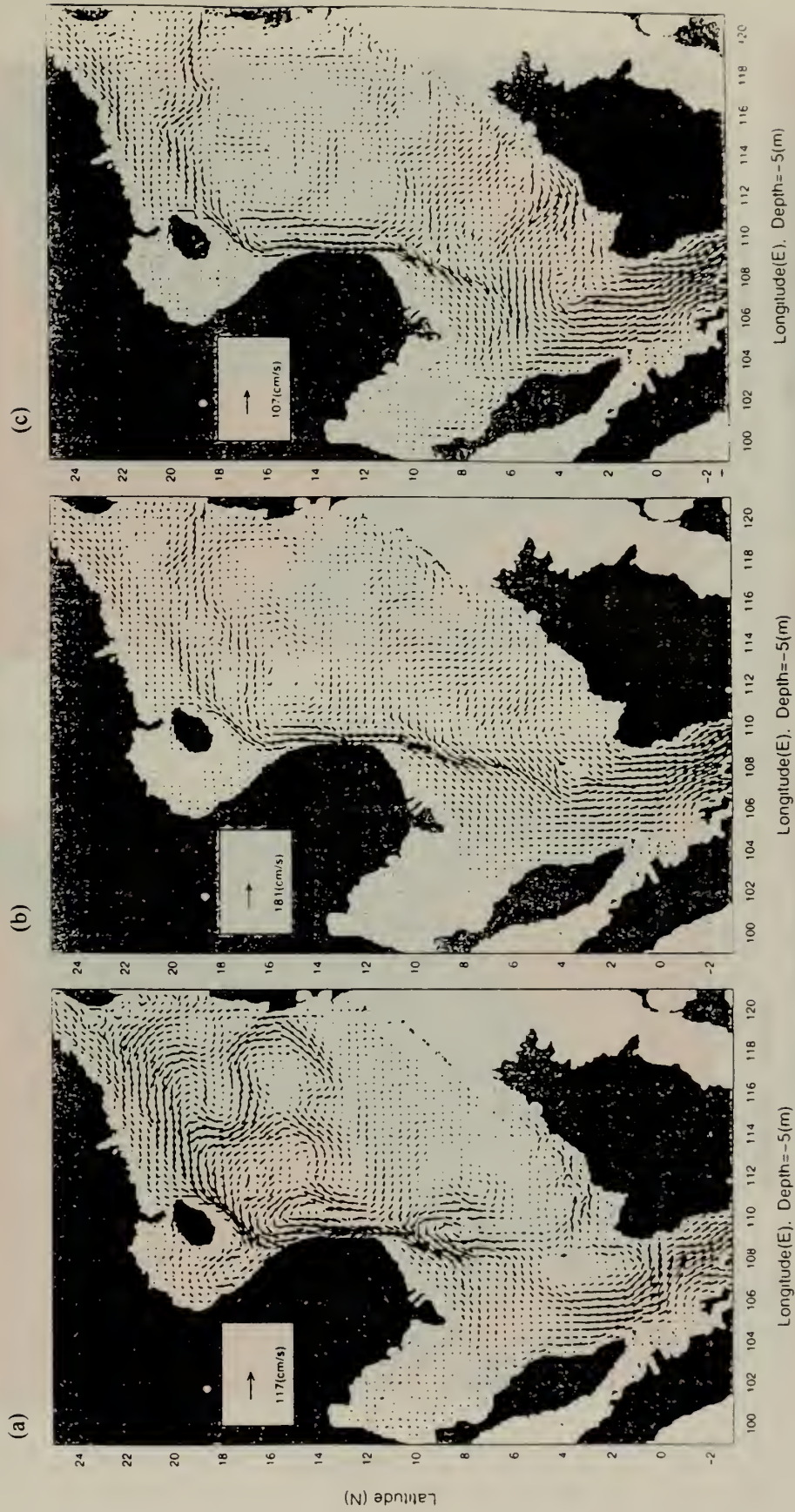


Figure 42. Near surface circulation for double lateral transport run during winter
 (a) October 15, (b) December 15, (c) March 15.

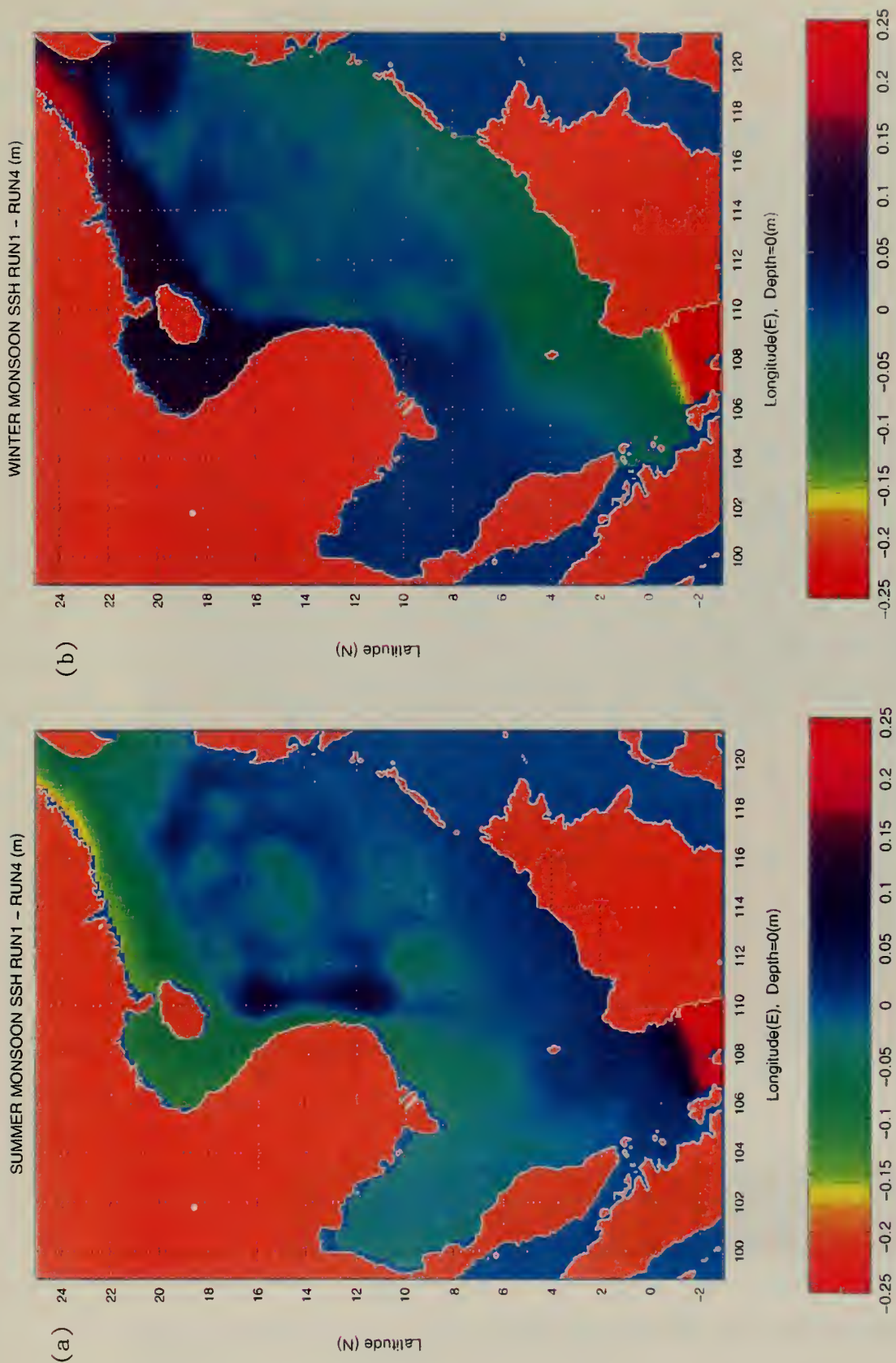


Figure 43. Sea surface height difference (m) between control run and closed boundaries run averaged over (a) summer monsoon, (b) winter monsoon.

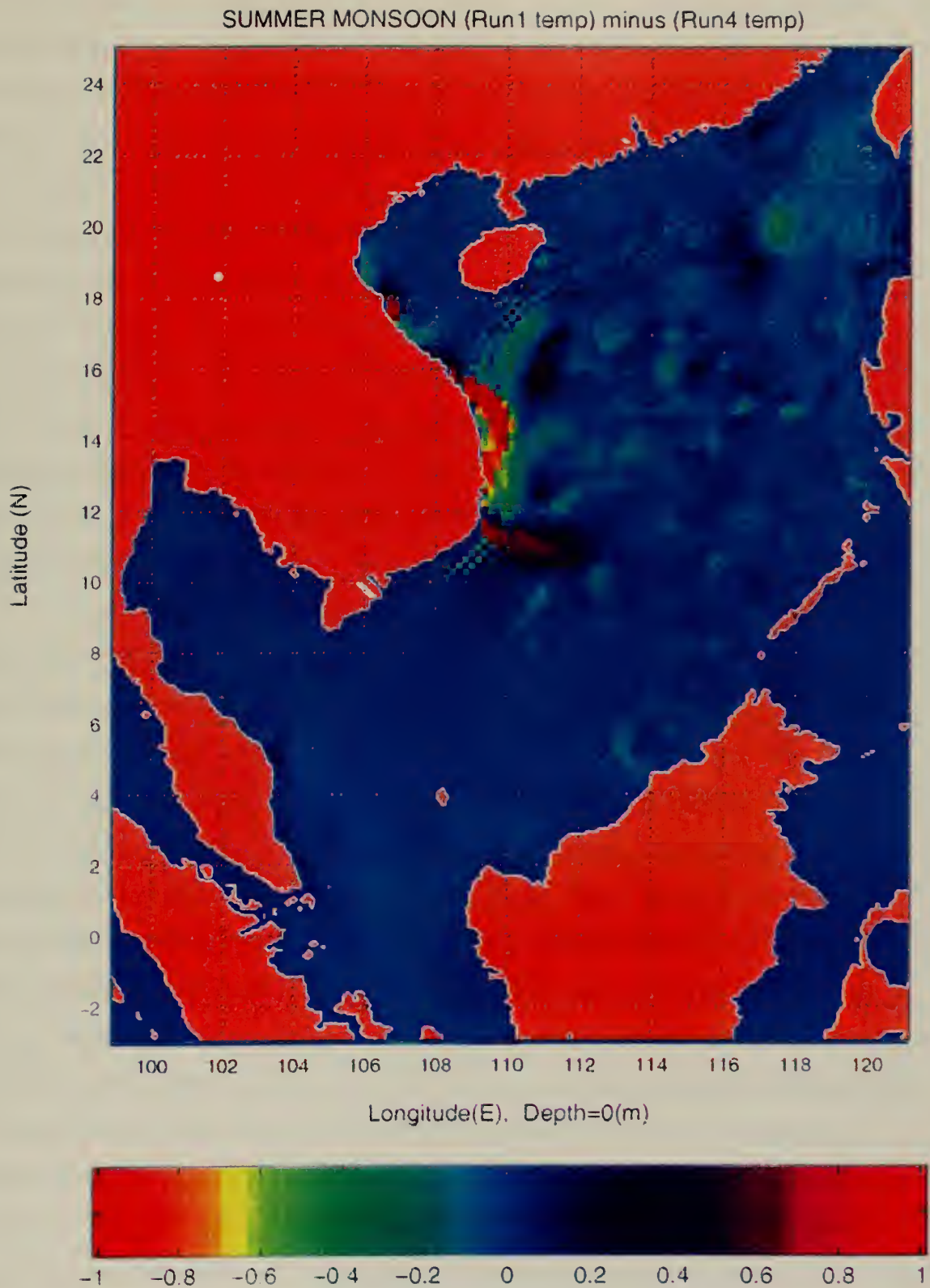


Figure 44. Sea surface temperatures difference ($^{\circ}\text{C}$) between control run and closed boundaries run averaged over summer monsoon.

it still joins the flow out of the Gulf of Thailand to contribute to an intensification of current off southern Vietnam. At 6° N, however, notice that the average northward velocity throughout most of the shallow shelf region shows no discernible pattern of change, while the shelf current along the 100 m isobath decreases by 5-10 cm/s (Figure 45). Farther north the VCJ does not continue along the 100 m isobath to Hainan as it did in the control run (Figure 41b), by 13° N the northward coastal jet has been replaced by a shallow (0-150 m) equatorward current flowing at 10 cm/s (Figure 46). Including the change in direction, the contribution to northward volume transport made by lateral transport is nearly 5.5 Sv (Table 3). The southwestward meander of the coastal jet observed in the control run takes all the current coming north, and the new southward surface current flowing from Hainan, and diverts the flow across the basin. The net effect is that by 50 m depth the circulation in this run is divided into a cyclonic gyre in the northern half of the model and an anticyclonic gyre in the south.

Winter closed boundary circulation patterns on the other hand, show less difference in structure from the control run (Figure 42) but more variability in magnitude. There is an average decrease of 10-40 cm/s in current speed of the winter VCJ (Figure 47b), which equates to approximately 4.8 Sv southward volume transport. The positive wind curl acts to strengthen the cyclonic gyre nature of overall circulation. The Kuroshio intrusion and inflow through the Formosa Strait are obviously supplemented by recirculation flow from along the coast of Luzon Island. Near Natuna Island it is noteworthy that the structure of cross basin circulation and current flow away from the Borneo coast are unchanged. Similarly, it is apparent that the spatial extent and shape of the gyre northeast of Natuna Island is unchanged by closing the boundary flow. In cross section, however, it can be seen that the NIG does lose some of its velocity--there is a 10-30 cm/s decrease in the average core velocity on the western side at 6° N in this run (Figure 47a) corresponding to a volume transport of 3 Sv, associated with the decrease in velocity of the VCJ. The difference in velocity is much smaller on the eastern side, suggesting that some other effect dominates the current structure in that region.

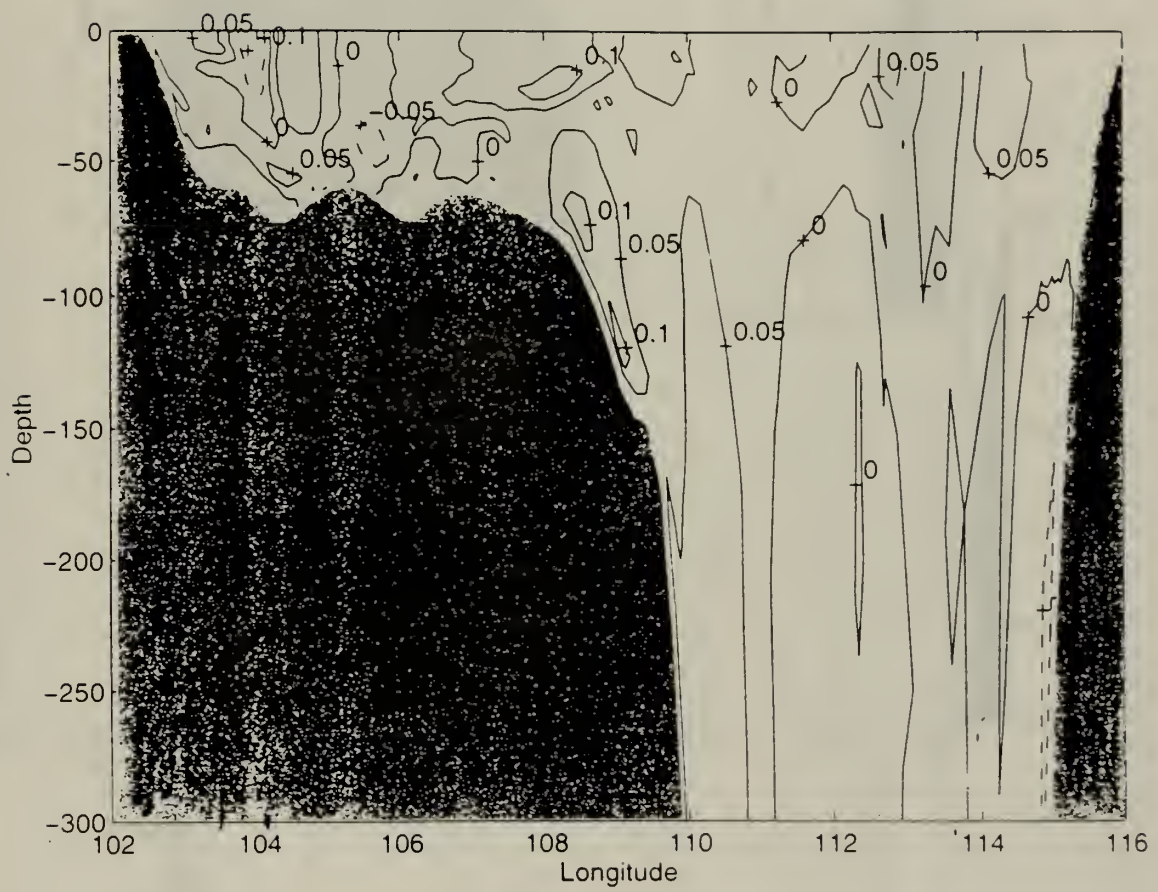


Figure 45. V component of velocity difference (m/s) between control run and closed boundaries run averaged over summer monsoon at 6° N latitudinal cross section.

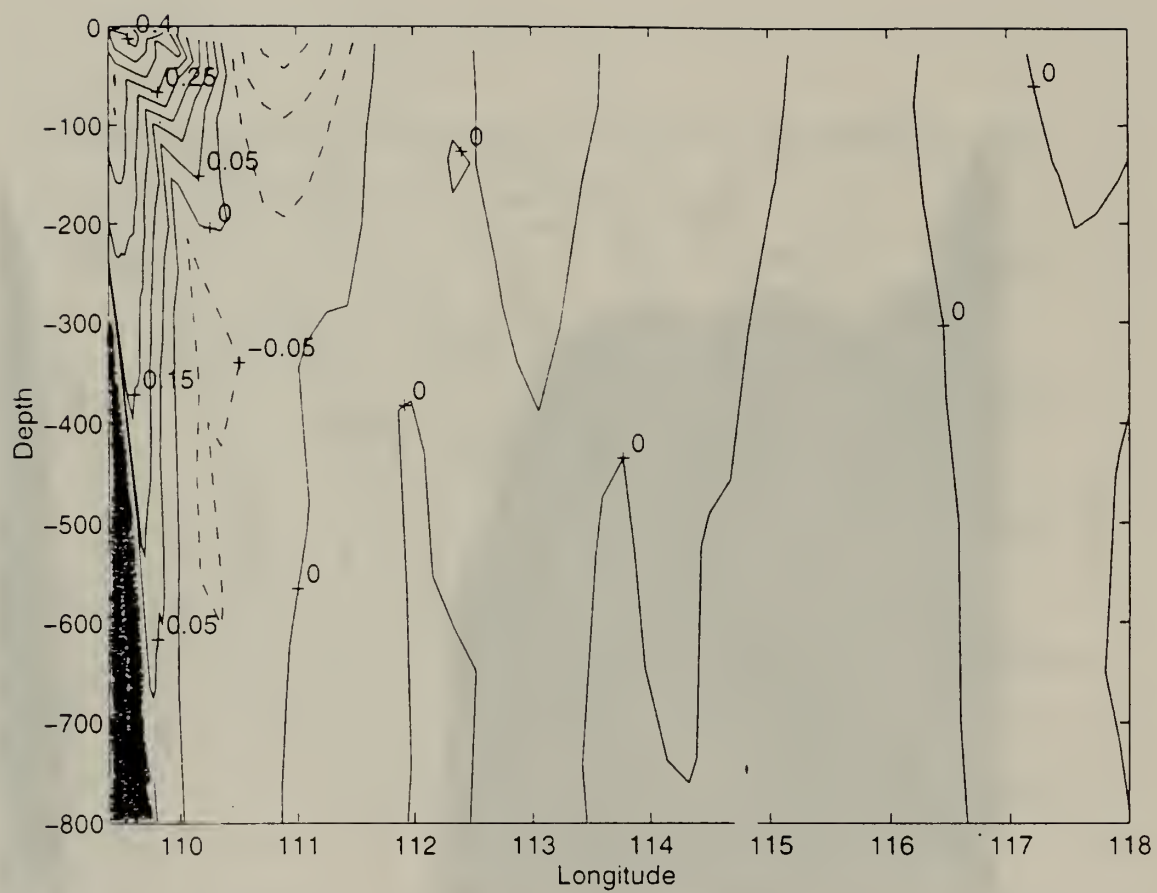


Figure 46. V component of velocity difference (m/s) between control run and closed boundaries run averaged over summer monsoon at 13° N latitudinal cross section.

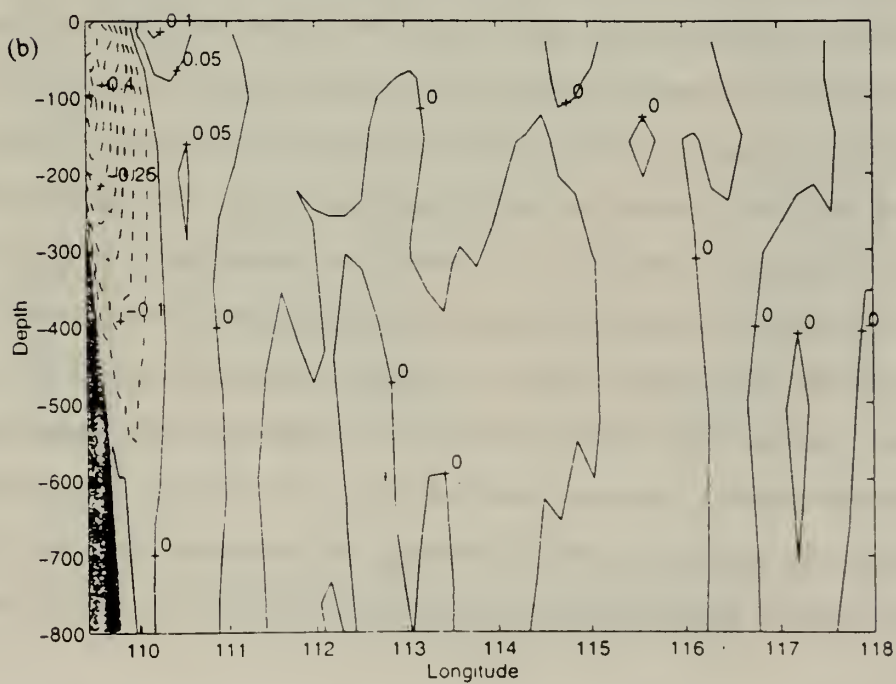
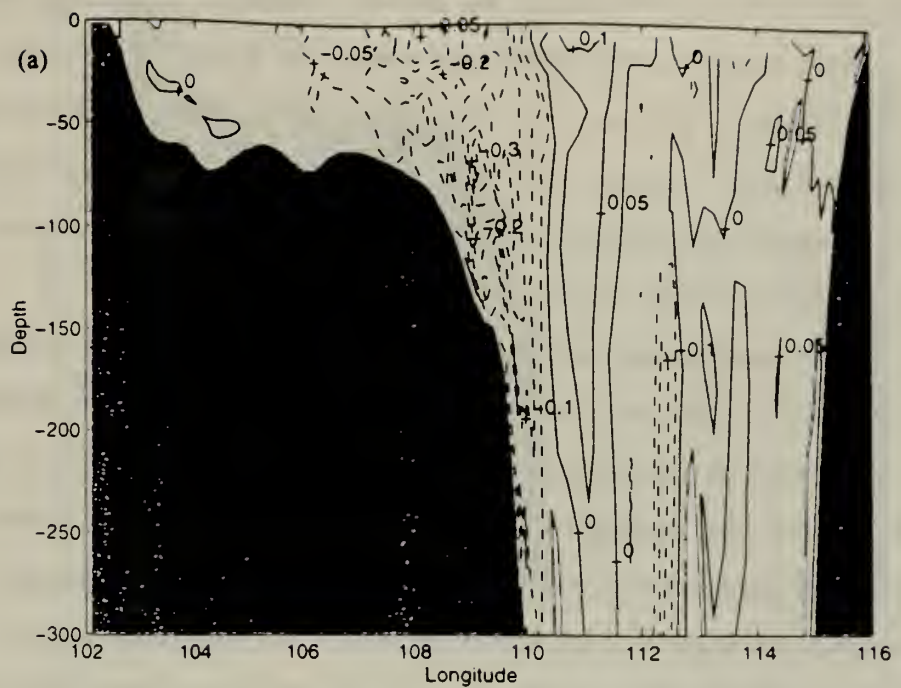


Figure 47. V component of velocity difference (m/s) between control run and closed boundaries run averaged over winter monsoon at (a) 6° N latitudinal cross section, (b) 13° N latitudinal cross section.

The final sensitivity study presented here used the standard equations and forcing but doubled the inflow transport at the lateral open boundaries. Doubling the inflow resulted in a near doubling of maximum velocities and a commensurate increase in the kinetic energy (Figure 22b). The time progression of maximum values of the vectors on the time series of near surface velocities (Figures 41-42) closely match the pattern of Wyrki's climatological values for open boundary transport.

Summer circulation patterns match the control run closely, with a few exceptions. First, there is no discernible western intensification of flow along the coast of Malaysia (Figure 41b). An increase in northward volume transport along the eastern side of the Sunda Shelf displays how the increased inflow through Gaspar and Karimata Straits becomes a broad northward current rather than intensified in the west. This broader current then becomes a stronger VCJ when it interacts with the bathymetry south of Vietnam. The cross section at 6° N shows an average of only 10 cm/s increase in velocity in northward surface current flow and shelf current flow (Figure 48a), but the effect is spread over the entire cross section resulting in an overall increased volume transport. By 13° N, however, the increase is 50 cm/s and all of it focused in the coastal jet (Figure 48b) increasing northward volume transport by more than 5.2 Sv. Additionally, the VCJ does not show the separation from the 100 m isobath near Hainan that is evident in the control run, flow into the the model at the south boundary follows the bathymetry out of the north boundaries. This is also evident in the volume transport difference, the large positive values along the 100 m isobath represent the increase in current transport when the summer lateral boundary transport is doubled (Figure 49). Second, since the current velocity is higher, the baroclinic instability is stronger and cross basin meander activity is of greater spatial extent, detracting from the anticyclonic nature of the summer circulation (Figure 42).

In the winter, the circulation is also very similar to the control run. As the flow becomes increasingly linear in and out of the model domain, there is a 20 cm/s increase in the velocity of the VCJ (Figure 50b), corresponding to an increase in southward volume

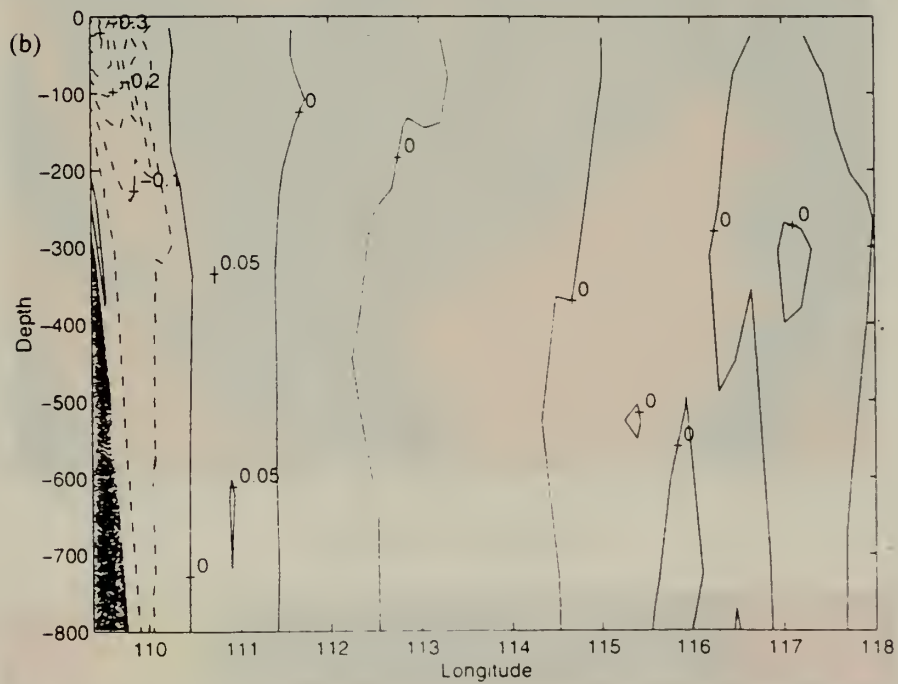
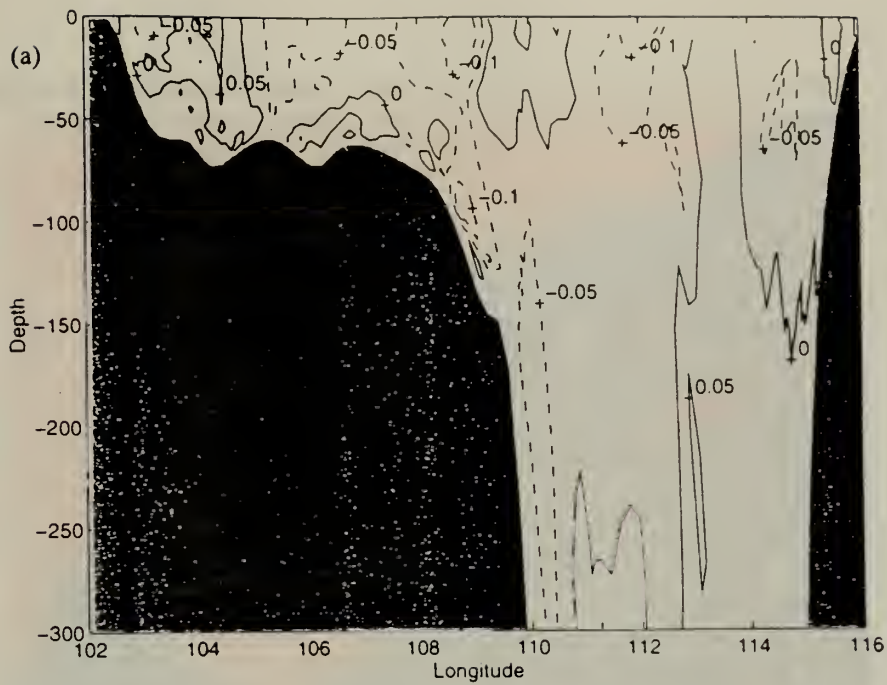


Figure 48. V component of velocity difference (m/s) between control run and double lateral transport run averaged over summer monsoon at (a) 6° N latitudinal cross section, (b) 13° N latitudinal cross section.

SUMMER MONSOON Volume Transport difference (Sv) due to 2X lateral transport

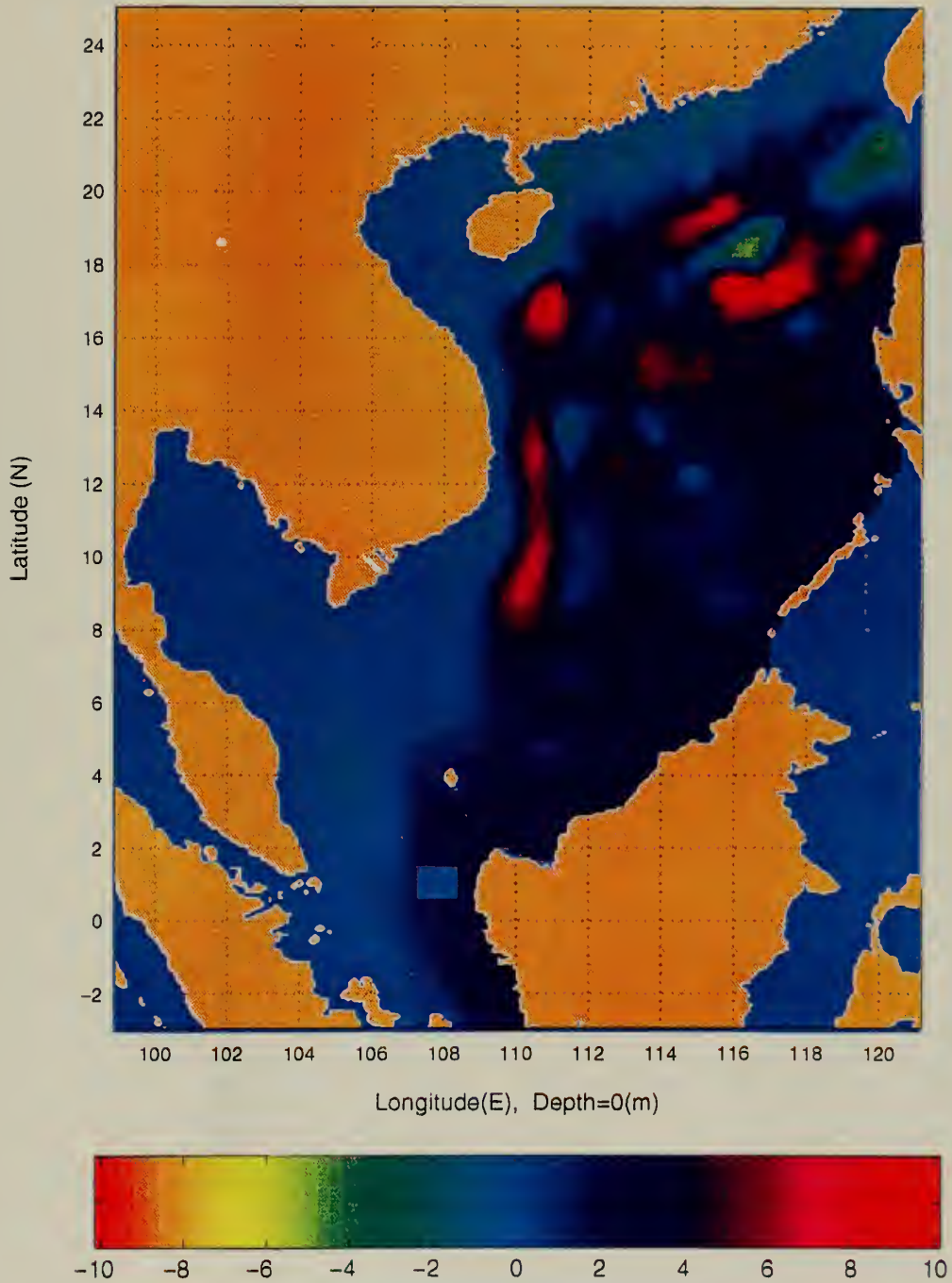


Figure 49. Volume transport difference (Sv) between control run and double lateral transport run averaged over summer monsoon.

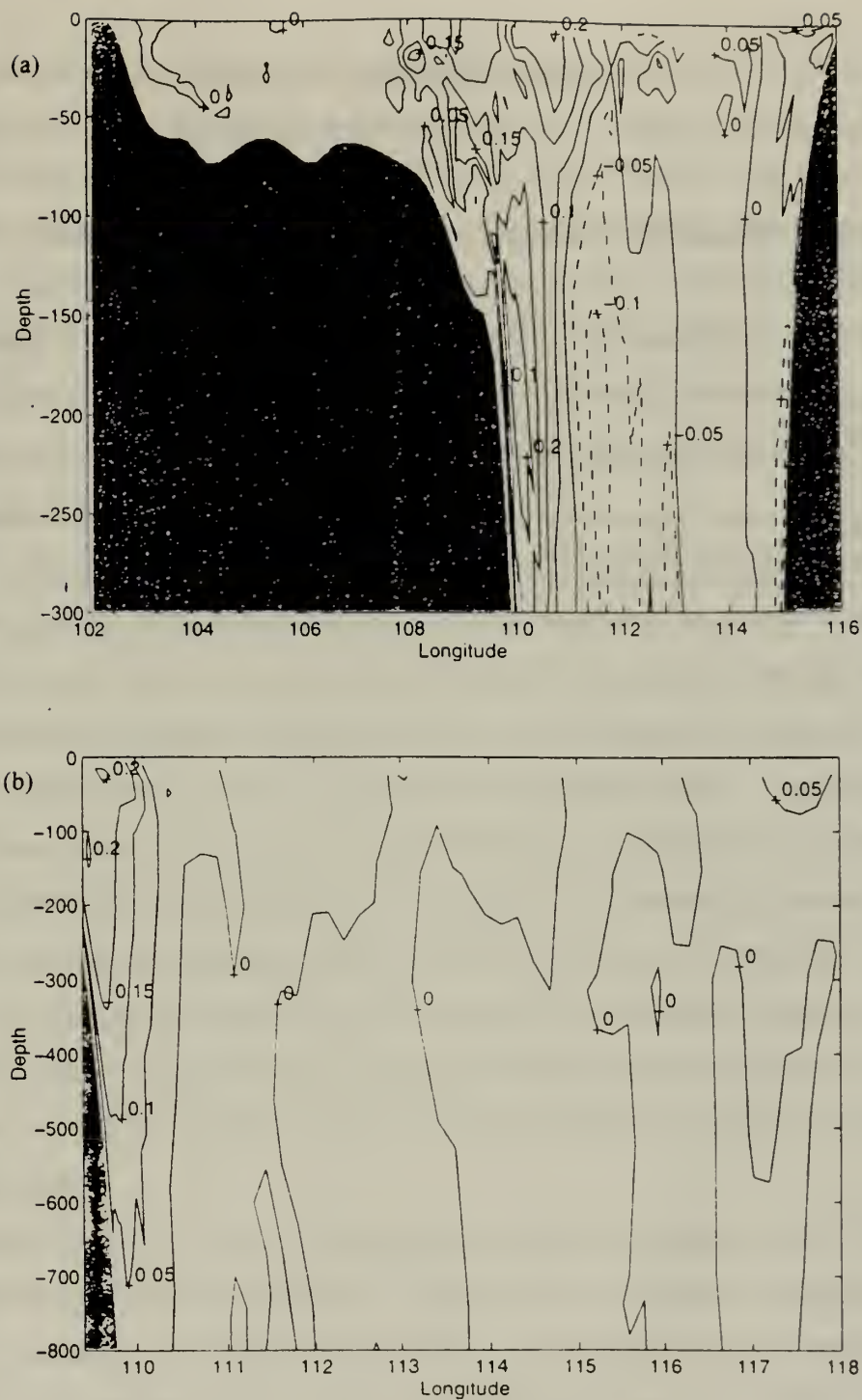


Figure 50. V component of velocity difference (m/s) between control run and double lateral transport run averaged over winter monsoon at (a) 6° N latitudinal cross section, (b) 13° N latitudinal cross section.

transport of 2.7 Sv. Farther south, the NIG shows an increase in average current velocity of 20 cm/s in the west (Figure 50a), corresponding to an increase in volume transport of 4.4 Sv.

Table 3: Summary of contributions to north/south volume transport (Sv) from isolated factors.

	Linear	No Wind	Zero Lateral Transport	Double Lateral Transport
Summer Vietnam Coastal Jet	0.0	0.0	-5.5	+5.2
Winter Vietnam Coastal Jet	-3.1	-4.6	-4.8	+2.7
Natuna Island Gyre (winter)	-3.0	-4.2	-3.0	+4.4

V. CONCLUSIONS

The South China Sea (SCS) is a dynamic and highly variable semi-enclosed sea subject to complex environmental forcing. Using the Levitus climatological dataset (1984) as an initial field, this thesis utilized the Princeton Ocean Model (POM) to simulate and analyze the SCS circulation and thermal structure. Experiments were conducted in which important forcing mechanisms (non-linearity, wind, and lateral boundary transport) were modified or eliminated to determine their effect on general circulation and specific oceanographic features.

With the exception of behavior in the region of baroclinic instabilities, advective non-linearity appears to be insignificant to the circulation during the monsoon seasons. When non-linear advection is removed from the system, the cascade of energy between levels of motion is reduced and the Reynolds stresses and fluxes that characterize turbulence no longer act as inhibitors for mean current kinetic energy. Thus the kinetic energy difference between the control run and linear run during the monsoon seasons reflects the importance of non-linearity as a mechanism for increasing velocities in eddy features. Removing non-linearity also had a small effect in areas of upwelling. Since the differences in velocity are significant only in the vicinity of the Natuna Island Gyre (NIG) and meander features, non-linearity is important to kinetic energy contained in baroclinic eddy features of the SCS but does not specifically determine any circulation or thermal structure features.

During the summer, when winds are blowing from the equator, the SST off the coast of central and northern Vietnam is 1-2 degrees cooler than when winds are absent, suggesting coastal upwelling due to Ekman drift is occurring in this area. Similar results are evident off the eastern coast of Hainan, as described in Huang et al. (1994). During the winter the surface temperature difference is greatest on the east side of the basin along the Palawan Trough, with similar results in surface salinity differences.

As seen in the no wind circulation and volume transport differences, the effect of the summer wind pattern is to increase the cross basin circulation and decrease the eddy behavior. Specifically, the northern filament of the summer Vietnam Coastal Jet (VCJ)

that migrates south during the summer is absent and the southwestward meander of the VCJ near 10° N is considerably reduced when winds are removed. Also, when winds are removed, a mesoscale anti-cyclonic eddy occurs over the Sunda Shelf that removes energy from the summer VCJ and decreases northward transport. In the winter the primary features of the hydrology essentially disappear when winds are removed--the VCJ is barely discernible and the NIG is diminished to near non-existence. Therefore, wind forcing is the primary factor in determining the strength and structure of the VCJ and NIG for the winter monsoon; if winds are light or non-existent during the winter, these features will be much less noticeable.

When the open boundary transport is removed, summer circulation features change substantially but the winter circulation remains largely unchanged. This is due to the shallowness of the southern portion of the model domain compared to the north. During the summer, the absence of lateral transport causes a two gyre system to develop with the cross basin meander at 10° N as the dividing current. When the open boundary transport inflow is doubled in the summer, the circulation pattern flows nearly linearly north to the VCJ and then out the northern boundary. The effect on the summer VCJ velocities and volume transport supports the conclusion that increased inflow linearizes the circulation through the SCS. Thus lateral boundary transport is essential to the existence of the summer VCJ between Vietnam and Hainan. During the winter, however, both the absence of lateral boundary transport and doubling the inflow have negligible effect on circulation patterns of the basin, merely decreasing and increasing the average velocities and volume transport without significantly affecting structure. Again we conclude that even though the transport through the Luzon Strait and Formosa Strait (winter) exceeds that of the Gasper and Karimata Straits (summer), the deep nature of the northern inflow boundary is responsible for the minimal effect of winter inflow/outflow on the SCS hydrology.

The contributions to north/south volume transport (Table 3) effectively summarize these conclusions for the identified features in the SCS. The summer VCJ was essentially determined by the lateral boundary transport; without open boundary

inflow there was no coastal jet. Non-linear advection and winds had no effect on volume transport, while closing the boundaries resulted in a loss of all 5.5 Sv originally present (Table 2). For the winter VCJ, lateral boundary transport and winds contributed equally to the transport. The topographic gyre was identified as a non-linear feature and therefore little can be concluded regarding effects of forcing terms from simple differencing although qualitatively the importance of wind is evident from the absence of this feature in the no wind run.

Future studies should concentrate on less simplistic scenarios. Inspection of observational surface currents from the Sulu Sea shows that these flows may be important to formation of the two gyre system that exists in the spring. Additionally, realistic surface heat and salt fluxes should be included and the use of extrapolated climatological winds needs to be upgraded to incorporate Naval Regional Ocean Atmospheric Prediction System (NORAPS) winds to improve realism. Finally, the assumption of quasi-linearity that allowed us to use simple differencing to quantify the effect of external forcing needs to be rigorously tested. It is very important to develop a thorough methodology to perform sensitivity studies under the highly non-linear conditions that may exist in the littoral environment.

LIST OF REFERENCES

- Blumberg, F., and Mellor, G., A simulation of the circulation in the Gulf of Mexico, *Israel J. Earth Science*, 34, 122-144, 1985.
- Blumberg, A., and Mellor, G., A description of a three dimensional coastal ocean circulation model, *Three-Dimensional Coastal Ocean Models*, edited by N.S. Heaps, American Geophysics Union, Washington D.C., 1-16, 1987.
- Chen, J., Fu, Z., and Li, F., A study of upwelling over Minnan-Taiwan shoal fishing ground, *Taiwan Strait*, 1, 5-13, 1982.
- Chu, P.C., C.C. Li, D.S. Ko, and C.N.K. Mooers, Response of the South China Sea to seasonal monsoon forcing, Proceedings of the Second International Conference on Air-Sea Interaction and Meteorology and Oceanography of the Coastal Zone, American Meteorological Society, Boston, 214-215, 1994.
- Chu, P.C., Huang, M. and Fu, E., Formation of the South China Sea warm core eddy in boreal spring, Proceedings of the Eighth Conference on Air-Sea Interaction, American Meteorological Society, Boston, 155-159, 1996.
- Ezer, T. and Mellor, G., A numerical study of the variability and the separation of the Gulf Stream, induced by surface atmospheric forcing and lateral boundary flows, *Journal of Geophysical Research*, 22, 660-682, 1992.
- Haney, R.L., Surface boundary conditions for ocean circulation models, *Journal of Physical Oceanography*, 1, 241-248, 1971.
- Hellerman, S. and Rosenstein, M., Normal monthly wind stress over the world ocean with error estimates, *Journal of Physical Oceanography*, 13, 1093-1104, 1983.
- Hu, J. and Liu, M., The current structure during summer in southern Taiwan Strait, in *Tropic Oceanology*, 11, 42-47, 1992.
- Huang, Q. and Wang, W., Current characteristics of the South China Sea, in *Oceanology of China Seas*, edited by Z. Di, L. Yuan-Bo, and Z. Cheng-Kui, 39-46, Kluwer, Boston, 1994.
- Levitus, S., Climatological atlas of the world ocean, *NOAA Professional Paper*, 13, U.S. Government Printing Office, Washington D.C., 173 p, 1984.
- Li, C., A numerical simulation of seasonal circulation in the South China Sea, Masters thesis, Naval Postgraduate School, Monterey, 74 p, 1994.

- Mellor, G., Users guide for a three-dimensional, primitive equation, numerical ocean model, Princeton University, 34 p, 1992.
- Mellor, G., and Ezer, T., A Gulf Stream model and an altimetry assimilation scheme, *Journal of Geophysical Research*, 96, 8779-8795, 1991.
- Mellor, G., and Yamada, T., Development of a turbulence closure model for geophysical fluid problems, *Review of Geophysical Space Physics*, 20, 851-875, 1982.
- Oey, L. and Chen, P., Frontal waves upstream of a diabathic blocking: a model study, *Journal of Geophysical Research*, 21, 1643-1663, 1991.
- Pohlmann, T., A three-dimensional circulation model of the South China Sea, In: *Three-Dimensional Models of Marine and Estuarine Dynamics*, edited by J. Nihoul and B. Jamart, 245-268, Elsevier-Science Publishing Co., Amsterdam, 1987.
- Pond, S. and Pickard, G., Introductory Dynamical Oceanography, 2nd Ed., Pergamon Press, 329 p, 1983.
- Smagorinsky, J., General circulation experiments with the primitive equations, I. The basic experiment, *Monthly Weather Review*, 91, 99-164, 1963.
- Wang, W. and Huang, Q., Three-dimensional numerical modeling of the water circulation in South China Sea, in *Oceanology of China Seas*, edited by Z. Di, L. Yuan-Bo, and Z. Cheng-Kui, Kluwer, Norwell, 91-100, 1994.
- Wang, J., Mysak, L., and Ingram, R., A three dimensional numerical simulation of Hudson Bay summer ocean circulation: topographic gyres, separations, and coastal jets, *Journal of Physical Oceanography*, 24, 2496-2513, 1994.
- Wyrski, K., Scientific results of marine investigations of the South China Sea and the Gulf of Thailand 1959-1961, *Naga Report, Vol 2&3*, the University of California Scripps Institution of Oceanography, 1960.

INITIAL DISTRIBUTION LIST

No. of copies

1. Defense Technical Information Center2
8725 John J. Kingman Rd., STE 0944
Ft. Belvoir, VA 22060-6218

2. Dudley Knox Library2
Naval Postgraduate School
411 Dyer Rd.
Monterey, CA 93943-5101

3. Superintendent1
Attn: Chairman, Department of Meteorology (Code MR/WX)
Naval Postgraduate School
Monterey, CA 93943-5000

4. Superintendent1
Attn: Chairman, Department of Oceanography (Code OC/BF)
Naval Postgraduate School
Monterey, CA 93943-5000

5. Superintendent3
Attn: Professor Peter C. Chu
Naval Postgraduate School
Monterey, CA 93943-5000

6. Lt. Nathan Edmons2
9490 Stargaze Rd.
San Diego, CA 92129

7. Superintendent1
Naval Research Laboratory
7 Grace Hopper Avenue Stop 2
Monterey, CA 93943-5502

8. Chairman1
Oceanography Department
U.S. Naval Academy
Annapolis, MD 21402

9. Office of Naval Research (Code 420)1
800 N. Quincy Street
Arlington, VA 22217

10. Library1
Scripps Institution of Oceanography
P.O. Box 2367
La Jolla, CA 92037
11. Dr. Ted Bennett1
Naval Oceanographic Office (Code N531)
Stennis Space Center, MS 39522
12. Dr. Martha Head1
Naval Oceanographic Office (Code N53)
Stennis Space Center, MS 39522
13. Dr. Charles Horton1
Naval Oceanographic Office (Code N531)
Stennis Space Center, MS 39522
14. Andy Johnson1
Naval Oceanographic Office (Code N531)
Stennis Space Center, MS 39522
15. Dr. Mike Carron1
Naval Oceanographic Office (Code N3T)
Stennis Space Center, MS 39522
16. Steven D. Haeger2
Naval Oceanographic Office (Code N3T)
Stennis Space Center, MS 39522
17. NOAA Library1
7600 Sand Point Way NE
Building 3
Seattle, WA 98115

7.1. 9/21/98

~~LIBRARY~~
~~MONTEREY STATE SCHOOL~~
~~MONTEREY, CA 93940-5101~~

DUE TO MONTEREY STATE SCHOOL
MONTEREY, CA 93940-5101

DUDLEY KNOX LIBRARY



3 2768 00349809 8

7

8

9

0

1



DUDLEY KNOX LIBRARY



3 2768 00349809 8